Studying strongly correlated hybrid quantum systems through quantum simulations and efficient numerical approaches

UNIWERSYTET
WARSZAWSKI

Doctoral Thesis

Author: João Pedro Vieira de Mendonça Santos

Advisor: Krzysztof Jachymski

2025

Abstract

Strongly correlated quantum systems, characterized by competing interactions, play a central role in emergent phenomena across quantum materials. Motivated by the need for robust models and reliable simulation techniques, this thesis develops a rigorous theoretical framework alongside novel efficient methods to study hybrid quantum systems that combine light–matter and electron–phonon interactions.

We begin by deriving the fundamental Hamiltonians governing these interactions. For light–matter systems, the second quantization of the electromagnetic field leads to the Dicke model, which is then extended by incorporating direct spin–spin interactions. In parallel, the Holstein model for electron–phonon systems is derived and further generalized to include electron–electron interactions, thereby capturing the essential physics of competing processes in complex materials.

Building on these theoretical developments, efficient numerical techniques are introduced by representing bosonic degrees of freedom through Gaussian and non-Gaussian states and applying variational methods that culminate in a hybrid numerical approach. This method integrates a variational ansatz for the bosonic sector with many-body numerical techniques for fermionic and spin components, enabling precise simulations of strongly correlated systems.

The developed framework is then applied to both sectors. For electron–phonon systems, a quantum simulation platform is proposed and the hybrid numerical method is validated on the Hubbard–Holstein model, serving as a precursor to its extension to more complex scenarios. For light–matter systems, the extended Dicke–Heisenberg model is systematically investigated under the hybrid numerical method to elucidate the interplay between spin–photon and spin–spin interactions and to clarify the conditions underlying superradiance and magnetic ordering.

Overall, this study provides a clear and versatile framework for exploring the interplay of competing interactions in hybrid quantum systems, with direct implications for both theoretical analysis and experimental design in quantum materials.

Abstrakt

Układy kwantowe o silnych sprzężeniach, charakteryzujące się konkurującymi oddziaływaniami, odgrywają kluczową rolę w emergentnych zjawiskach w materiałach kwantowych. Motywowana potrzebą niezawodnych technik symulacyjnych, niniejsza rozprawa rozwija ramy teoretyczne wraz z efektywnymi metodami badania hybrydowych układów kwantowych, takich jak silnie skorelowane układy światło-materia oraz elektron-fonon.

Rozpoczynamy od wyprowadzenia fundamentalnych hamiltonianów opisujących te oddziaływania. Dla układów światło–materia, druga kwantyzacja pola elektromagnetycznego prowadzi do modelu Dickego, który następnie zostaje rozszerzony poprzez włączenie bezpośrednich oddziaływań spin–spin, tworząc model Dicke–Heisenberga. Równolegle wyprowadzony zostaje model Holsteina dla układów elektron–fonon, który jest dalej uogólniany o oddziaływania elektron–elektron, co pozwala uchwycić istotną fizykę konkurujących ze sobą procesów w złożonych materiałach. Bazując na tym modelu teoretycznym, wprowadzamy efektywne techniki numeryczne, polegające na reprezentowaniu bozonowych stopni swobody za pomocą stanów gaussowskich, a następnie niegaussowskich, oraz zastosowaniu metod wariacyjnych, które odgrywają kluczową rolę w hybrydowym podejściu numerycznym. Metoda ta łączy wariacyjny ansatz dla sektora bozonowego z technikami numerycznymi dla układów wielociałowych zastosowanych do komponentów fermionowych i spinowych, umożliwiając precyzyjne symulacje układów o silnych sprzężeniach.

Opracowana metoda jest następnie stosowana w obu obszarach. Dla układów elektron–fonon zaproponowana jest również platforma symulacji kwantowych, a hybrydowa metoda numeryczna jest weryfikowana na modelu Hubbard–Holsteina, stanowiąc punkt wyjścia do rozszerzenia jej na bardziej złożone scenariusze. Dla układów światło–materia systematycznie badany jest rozszerzony model Dicke–Heisenberga, aby wyjaśnić współdziałanie oddziaływań spin–foton i spin–spin oraz doprecyzować warunki leżące u podstaw nadpromienności i uporządkowania magnetycznego. Podsumowując, niniejsza rozprawa dostarcza jasnych i wszechstronnych ram do badania współdziałania konkurencyjnych oddziaływań w hybrydowych układach kwantowych, mając bezpośrednie zastosowanie zarówno dla analizy teoretycznej, jak i projektowania eksperymentalnego materiałów kwantowych.

List of Publications

The content of this dissertation is primarily based on the results published in the following works, co-authored by the author, his supervisor, and colleagues. These articles were disseminated to present the research outcomes achieved during the author's PhD studies:

1. J. P. Mendonça, K. Jachymski, *Quantum simulation of extended electron–phonon-coupling models in a hybrid Rydberg atom setup*, Phys. Rev. A **107**, 032808 (2023).
2. J. P. Mendonça, K. Jachymski, Y. Wang, *The role of exchange interactions in the superradiant phenomena*, arXiv:2503.04961 (2024).
3. J. P. Mendonça, Y. Wang, K. Jachymski, *A variational non-Gaussian approach to cavity QED with strongly interacting emitters*, In preparation.

Other research papers

1. J. P. Mendonça, I. Gleria, M. L. Lyra, *Delay-induced bifurcations and chaos in a two-dimensional model for the immune response*, Physica A: Statistical Mechanics and its Applications **517**, 484–490 (2019).
2. J. P. Mendonça, I. Gleria, M. L. Lyra, *Prey refuge and morphological defense mechanisms as nonlinear triggers in an intraguild predation food web*, Commun. Nonlinear Sci. Numer. Simul. **90**, 105373 (2020).
3. J. P. Mendonça, FABF de Moura, M. L. Lyra, G. M. A. Almeida, *Emergent nonlinear phenomena in discrete-time quantum walks*, Phys. Rev. A **101**, 062335 (2020).
4. J. P. Mendonça, FABF de Moura, M. L. Lyra, G. M. A. Almeida, *Generation and distribution of atomic entanglement in coupled-cavity arrays*, Phys. Rev. A **102**, 062416 (2020).
5. P. A. Brandão, J. P. Mendonça, S. B. Cavalcanti, *Low coherence-induced resonance in double-layer structures having parity–time symmetry*, Opt. Lett. **46**, 717–720 (2021).

6. P. R. N. Falcão, J. P. Mendonça, A. R. C. Buarque, W. S. Dias, G. M. A. Almeida, and M. L. Lyra, *Nonlinear three-state quantum walks*, Phys. Rev. A **106**, 042202 (2022).
7. J. P. Mendonça, Arthur A. Brum, M. L. Lyra, Sérgio A. Lira, *Evolutionary game dynamics and the phase portrait diversity in a pandemic scenario*, Appl. Math. Comput. **475**, 128749 (2024).
8. J. P. Mendonça, S. Biswass, M. Lewenstein, K. Jachymski, T. Grass, *Effect of band flattening in ladder systems with non-Fermi liquid behavior*, In preparation.

Author Contributions: In all the listed articles, I had a leading contribution by performing all the derivations and calculations while playing an extensive role in the writing process. Exceptions are: for publication **7**, I developed only the theoretical framework (including model development and analysis), while Arthur Brum (the second author) handled the data analysis; for publication **6**, Pedro Falcão was the main author, so my role was primarily supportive and mentoring; and for publication **5**, Paulo Brandão and I contributed equally in terms of derivations and calculations.

Acknowledgements

I thank my advisor and friend, Krzysztof, who early saw my potential and has accepted my application to become his PhD student. Coming from a distant country, from another continent, was not easy, and I am deeply grateful by his immensurable support during this stage of my life. For that support I also thank his family for all the help they offered me and my wife specially during our first year in Poland. We have never actually learned how to pronounce each other's names correctly, but we overcome language and cultural barriers easily. I have learned a lot during his supervision and I can say that I have matured as a scientist.

Eu agradeço a minha amada esposa Lucielly por todo o suporte emocional durante esse longo processo que, apesar de ter sido divertido e valido a pena, teve seus momentos difíceis. Eu reconheço todo o esforço que foi mudar para um outro país com língua e cultura totalmente diferentes. Seu sorriso e suporte constantes me ajudaram a chegar até o fim dessa jornada. Obrigado por ter sido companheira e ter sempre apoiado minha carreira.

Agradeço a minha familia por estar sempre comigo, principalmente meus pais, Fernando e Ana, e meus sogros Lucélia, Sebastião, João e Luciana. Agradeço a minha irmãzinha que sempre me traz orgulho e me faz querer sempre ser o irmão modelo.

I thank the friends that I have acquired during this process, Sakthi, Sangami, Piotr, Felipe, Fernanda. A special thanks to Sakthi and Sangami for all the fun that we have together. Without you guys, I would likely get insane before graduation. Agradeço aos meus amigos da UFAL que me apoiaram a seguir em frente e correr atrás dos meus sonhos e mantiveram a amizade e, sempre que puderam, contato mesmo havendo toda essa distância: Pedro do bigode, Mari, Waltinho, Nico, e a antiga galera do GFTC. Um agradecimento especial ao Pedro que está bem perto e sempre conversa comigo sobre trabalho, aleatoriedades, e a famigerada mágica em MBL.

I thank all professors that helped me grow. My former advisors Guilherme and Marcelo, who have been always supportive and hopeful about my carrier. They taught me basically everything that I am proud of knowing before the PhD studies. In particular, I thank my close collaborators Tobias Grass and Yao Wang. Collaborating with them was an amazing learning experience that made me a better scientist.

Contents

1

Introduction

Highly correlated systems lay the foundation for exploring novel phases of matter due to *emergent phenomena*. In fact, one of the goals of modern condensed-matter physics is to design states of matter with desirable emergent properties. Two important examples of emergent phenomena are superfluidity and fractional quantum Hall effect: low-energy collective effects of many particles that cannot be deduced from the microscopic equations of motion in a rigorous way and that disappears completely when the system is taken apart. Emergent phenomena are associated with the formation of quasi-particles–effective excitations arising from collective interactions in many-body systems–that behave in ways nearly identical to those of genuine particles. For example, in a crystal, lattice vibrations turn into phonons–the quanta of sound which, at low-energy scales, behave as a particle. Phonons propagate carrying energy and momentum without decaying, and are only destroyed if the crystal falls apart. Phonon-mediated interactions can lead to emergent phenomena such as conventional superconductivity.

When studying systems with unpredictable emergent phenomena, it helps to clearly define when two states of matter are the same. This is related to the study of phase transitions, which occur only in the thermodynamic limit. In smaller systems, finite-size effects smooth out the transition. One common way to investigate this is by testing whether one state can continuously transform into another–a process known as an adiabatic transformation. In small systems, this continuous transformation is readily observed, whereas in thermodynamically large systems, even minor perturbations can induce abrupt, dramatic shifts, making such smooth transitions impossible. When this happens, we say the states belong to different phases. For example, the microscopic details of the electron-electron interactions are not so important if the emergent phenomena observed are qualitatively the same: two metals with slightly different interactions are considered the same phase since the macroscopic behavior is metallic. On the other hand, a metal and an insulator belong to two distinct quantum phases. This idea simplifies our understanding by circumventing the need to predict complex behaviors solely from first principles–a task that remains extremely challenging even with current methods [56]. In short, the essential feature that defines strongly correlated systems, also known as quantum materials, is that the behavior of its components cannot be described solely in terms of non-interacting entities.

A broad class of quantum materials involves combining two systems with distinct nature, such as bosons and fermions. Strong competing interactions between the distinct components lead to novel quasi-particles, which then lead to complex emergent phenomena. For example, strong interaction between electrons and phonons form polarons at low-temperature. Polarons are quasiparticles defined as an electron plus an attached phonon cloud. Effectively, the electrons screen the atoms in the lattice while the lattice screens the electrons. The effective attractive interaction between electrons competes with strong electron-electron interactions which can lead to the conventional superconductivity, as aforementioned. Analogously, we have the quasi-particle called polariton, where photons, the quanta of light, strongly interact with a dipole-carrier excitation, such as excitons. In the quest for designing states of matter for implementing quantum technologies, which exploit nonclassical correlations for computing, simulation, communication, and sensing purposes [36], composite systems offer a higher degree of control, as the interaction between distinct components offers indirect strong competing interactions among one of the constituents. As we will dig deeper in the next sections of this chapter and during the whole thesis, atom-photon and electron-phonon systems show to be great platforms to observe complex phenomena that are useful not only for future technological advancements but also for deepening the fundamental understanding of the microscopic nature of many collective macroscopic phenomena.

1.1 Collective atomic interactions with light

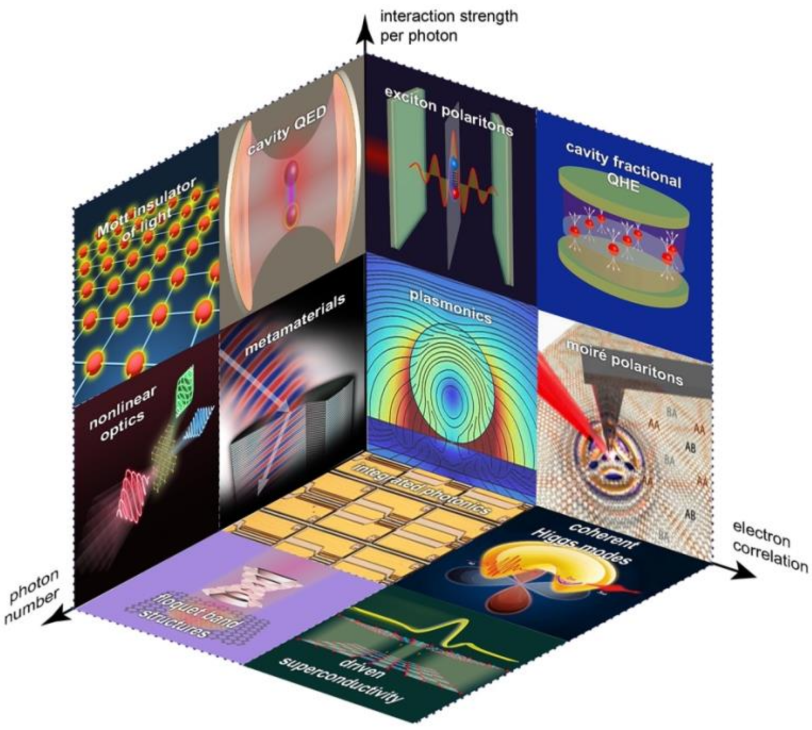

Figure 1.1: Conceptual 3D representation of the regimes in quantum optics. Adapted from [19] (arXiv, CC BY-NC-ND 4.0).

Optical methods are natural candidates for realizing state preparation and quantum control schemes in various systems, owing to the availability of tunable laser light, single-photon sources, and pulse modulation techniques that allow for excellent time resolution. It is also worthwhile to consider the backaction of the system in the light field, an essential aspect for applications such as energy storage and extraction in a quantum battery [69] or state readout from quantum memories [70]. These recent advancements enable the optical control of quasi-particles in solid-state systems, their many-body collective modes and excitations. This interplay between the distinct constituents is pushing the boundaries of important areas such as quantum materials, quantum optics, and nonlinear laser physics. The term *strongly correlated electron–photon science* was coined in Ref. [18] to refer to the research area that lies in the intersection of those then separated areas.

The majority of the aforementioned advancements on the optical control of solid-state quasi-particles relies on materials where electron correlations are weak. On the other hand, at weak interaction regimes, where a strong optical field can be treated semi-classically, light has been used to drive cooperative responses in strongly interacting materials. For instance by inducing transient high-temperature superconductivity [98], mediating long-range interactions leading to self-organization [119], photo-induced magnetism [34, 128], ferroelectricity [105, 85], and non-equilibrium topological phases [140, 93]. A conceptual map of research fields in quantum optics, classified according to emergent phenomena as functions of photon number, electron correlations, and electron-photon interaction strength (adapted from Ref. [19]), is shown in Fig. 1.1. Starting from a baseline with low photon numbers, weak electron-photon interactions, and negligible electron correlations, familiar regimes such as metamaterials, integrated photonics, and plasmonics are observed. The figure organizes phenomena based on which of these parameters is weak or absent. For example, in the absence of significant electron correlations, when electron-photon interactions are weak, increasing the photon number drives a transition from the linear optical responses of metamaterials to nonlinear optical phenomena, whereas with strong electron-photon interactions, low photon numbers lead to cavity quantum electrodynamics (cQED) phenomena and further increases in photon number result in exotic states like Mott insulators of light. In contrast, in the weak-field limit with strong electron correlations, weak electron-photon interactions can give rise to Moiré polaritons, while increasing the interaction strength in this regime leads to emergent phenomena such as exciton-polaritons and the cavity fractional quantum Hall effect as electron correlations become more pronounced. It is also important to note that when the photon number is large and electron-photon interactions are negligible, the strong light field behaves classically. Finally, by varying both the photon number and electron correlations in the absence of significant electron-photon interactions, a variety of phenomena emerge, including photo-induced driven superconductivity in systems with strongly correlated electrons under a strong field. Our main interest is in the interplay between strong electron correlations and interactions for small photon numbers, which we treat as an extension of cQED adding direct electron interactions that cause strong correlations. Starting from the paradigmatic Dicke model, we extend the model to include competing exchange interactions.

The Dicke model is a cornerstone for understanding collective interactions between a single-mode light field and matter. It has been experimentally realized in diverse platforms, including solid-state cavity QED [29], trapped ions [122], organic molecules [43], and cold gases [10, 119, 28, 110]. Central to its appeal is the superradiant phase transition, where macroscopic photon occupancy emerges as a distinctive characteristic of collective quantum behavior. Variations of this model have proven vital in understanding phenomena such as quantum batteries [42, 114, 35], polaritonic chemistry [117], and quantum spin glasses [131, 73]. In particular, photon-mediated long-range spin-spin interactions achieved via coupling to light enabled applications in quantum state engineering and spin squeezing [90, 103, 111]. The Dicke model is obtained via second quantization of the Hamiltonian of a collection of atoms in an external field under dipole approximation. The rigorous calculations for obtaining this model are shown as the ultimate goal of Chapter 2. Specifically, the conventional Dicke model is represented by the Hamiltonian:

$$\mathcal{H}_{\text{Dicke}} = \omega\left(a^\dagger a + \frac{1}{2}\right) + \frac{\varepsilon}{2}\sum_{i=1}^{N}\sigma_i^z + \frac{g}{\sqrt{N}}\sum_{i=1}^{N}\sigma_i^x(a + a^\dagger), \tag{1.1}$$

where the state of each two-level qubit is encoded by a local spin operator $s_n^\alpha = \sigma_n^\alpha/2$, and the photonic operators $x = (a^\dagger + a)/\sqrt{2}$, $p = i(a^\dagger - a)/\sqrt{2}$, with $a(a^\dagger)$ being the photon annihilation(creation) operator. Here, ω is the cavity frequency, ε the atomic transition frequency, g is the collective coupling strength, and N is the number of atoms. The Dicke model can be mapped to an SU(N) spin model and solved exactly [75], and exhibits a phase transition between superradiant and normal phases.

However, spin-spin interactions, arising from electronic Coulomb interactions or atomic interactions, are often unavoidable in realistic material and atomic systems. These interactions are expected to significantly affect the properties of the system, deviating from the conventional Dicke model, but are usually not included into theoretical studies due to the extremely increasing complexity. These interactions compete with light-induced order, offering a complex but potentially tunable platform to study quantum many-body phenomena both in and out of equilibrium. This generalization can be described by introducing a Heisenberg interaction term, written as

$$-\sum_{\langle i,j\rangle}\sum_{\alpha=x,y,z} J_\alpha s_i^{(\alpha)} \cdot s_j^{(\alpha)}. \tag{1.2}$$

The isotropic Heisenberg model ($J_\alpha = J$) features ferromagnetic and antiferromagnetic interactions, depending on the sign on the exchange interaction J. Indeed, these two types of interactions have distinct physical origins: in systems governed by Hund's coupling where intra-atomic exchange favors parallel spin alignment the effective interaction is ferromagnetic, while in systems where the interaction arises from superexchange processes (as in Hubbard models), the coupling is inherently antiferromagnetic [91]. The latter is obtained in Chapter 3 from the Hubbard model in the limit of strong on-site repulsion at half-filling. As we will see in Chapter 7, the interplay between strong spin-photon and spin-spin interactions leads to novel phenomena including a transient coexistence between spin order and photon superradiance.

1.2 Lattice vibrations coupled to electronic motion

Phonons are collective excitations of the vibrational modes in elastic materials. The crystal lattice formed by periodic arrangement of atoms is allowed to deform and distort without destroying the crystal structure. The vibrational modes are quantized and the formed quasiparticle representing the collective excitation is called *phonon*, as first coined by Frenkel [46]. Analogous to energy and momentum, phonon dispersion relation is given by $\omega(\mathbf{k})$ frequency and wavevector. Since $\mathbf{k}$ is well defined, phonons are not localized particles, but for a small $\mathbf{k}$ we obtain a fairly localized wavepacket with group velocity $v_{\mathrm{g}} = \mathrm{d}\omega(\mathbf{k})/\mathrm{d}\mathbf{k}$. As photons are the quanta of light, phonons are interpreted as the quanta of sound, and the group velocity is the velocity of sound in the material. However, phonons have a broad spectrum, which strongly depends on the source as they reveal themselves in all electrical, thermal, and optical phenomena in materials, are usually labeled in different frequency ranges as sound waves (10–10^4 Hz), ultrasound (10^4–10^8 Hz), hypersound (10^8–10^{11} Hz), and heat (over 10^{11} Hz) [104]. The phonon propagation can be engineered with low-dimensional systems (nano-structures) and metamaterials like phononic crystals. Phononics, or phonon engeneering, opens a wide range of possibilities for controlling transport such as acoustic and sound wave propagation, heat transfer, and mediated interactions.

The motion of ions arranged in a periodic lattice, quantized as phonons, couples with itinerant electrons and thus electron-phonon interactions become important. Electron-phonon interaction is one of the cornerstones of condensed-matter and materials physics, and its notion is as old as the quantum theory of solids. Despite being extensively studied, its emergent phenomena and the lack of a clear fundamental understanding makes it still very attractive. Coupling electrons with the lattice's vibrational degrees of freedom fundamentally alters the material's properties, leading to phenomena such as electrical resistance, superconductivity, and carrier relaxation in semiconductor structures [118].

Placing a charge in a polarizable media causes a screening effect that alters the properties of the carrier. In solids, the ions that constitute the lattice are polarized by the presence of electrons. In fact, electron motion induces ions to displace from their equilibrium positions followed by a relaxation which induces lattice vibrations. The electron carries the polarization around itself, effectively screening its charge, a phenomenon known as phonon cloud. The electron bound to the phonon cloud work as a single entity, a quasi-particle known as *polaron*, as coined by Pekar [109]. Properties of polarons such as response to external fields and effective mass differ from that of band electrons. The details of polaron formation are crucial for carrier transport since polaron formation leads to a larger effective mass of a carrier. In systems with strong electron-phonon interactions, like when coupling with longitudinal optical phonons, the polaron picture becomes dominant and governs the transport properties. The Frölich model [50, 48, 49] is the most paradigmatic model for polaron description. It considers the so described system of electrons in an ionic medium with electrons in the free electron approximation interacting with a single longitudinal optical phonon in the Einstein approximation. It reads

$$\mathcal{H}_{\text{Frölich}} = \frac{\mathbf{p}^2}{2m} + \hbar\omega \sum_{\mathbf{q}} b^{\dagger}_{\mathbf{q}} b_{\mathbf{q}} + \sum_{\mathbf{q}} (V_{\mathbf{q}} b_{\mathbf{q}} e^{i\mathbf{q}\mathbf{r}} + h.c.), \tag{1.3}$$

where $b_{\mathbf{q}}$ account for phonon the annihilation, $\mathbf{r}$, $\mathbf{p}$, and m are the position, momentum and mass of the band electron, and $V_{\mathbf{q}}$ is the effective potential experienced by the electrons given by

$$V_{\mathbf{q}} = -i\frac{\hbar\omega}{q}\sqrt{\frac{4\pi\alpha}{V}\sqrt{\frac{\hbar}{2m\omega}}} \quad \text{with} \quad \alpha = \frac{e^2}{\hbar}\sqrt{\frac{m}{2\hbar\omega}}\left(\frac{1}{\epsilon_\infty} - \frac{1}{\epsilon_0}\right), \tag{1.4}$$

where α is the dimensionless coupling constant, V is the volume, ϵ_∞ and ϵ_0 are the high-frequency and static dielectric constants. Since the model treats the phonon field in a continuum approximation, the resulting lattice distortion extends over many unit cells. Thus the quasiparticle emerging from the model is called a large polaron, its size is much larger than the lattice spacing. In short, the Fröhlich Hamiltonian is interesting because it captures how an electron in a polar crystal interacts with a long-range polarization field created by longitudinal optical phonons. This interaction leads to the formation of a large polaron—an electron dressed by a spread-out cloud of phonons. Its analytical tractability and relevance for understanding effective mass renormalization, carrier mobility, and various transport phenomena in polar materials make it a fundamental and insightful model in condensed matter physics. However, when dealing with materials where the electron-phonon interaction is essentially local, the Holstein model is more appropriate [64, 65]. We show in figure 1.2 a cartoon representation of the two types of polarons. In addition to its focus on local phonon modes, the Holstein model is compelling because it provides a minimal framework that captures the essential physics of small polaron formation. The understanding of polaron formation and its consequences is important to understand the underlying mechanisms of electron-phonon systems, however, in the work presented here, polarons are not the main goal of the study. A thorough analysis of polarons in general is found at Emin's book [38] and specifically for Frölich polarons in the progress review by Devreese and Alexandrov [4]. A compendium of theoretical and experimental realizations for both cases in found at [44].

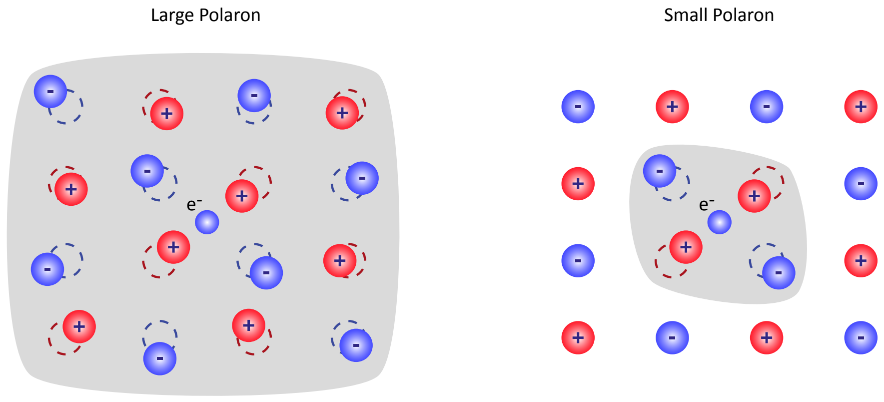

Figure 1.2: Fröhlich (large) and Holstein (small) polarons.

While the Fröhlich Hamiltonian is well-suited for describing extended, long-range interactions in polar materials, the Holstein model is particularly useful when the electron couples strongly to a local lattice distortion. This local interaction can lead to phenomena such as self-trapping of the electron, an increase in effective mass, and distinctive transport properties that are key in systems like molecular crystals or narrow-band semiconductors. Moreover, its relative simplicity allows us to apply some analytical approximations and numerical simulations, allowing for a deeper exploration of the interplay between electronic motion and lattice dynamics. In this work, we focus on extended Hubbard-Holstein models of the form

$$\mathcal{H}_{\mathrm{EHH}} = -t \sum_{\langle i,j\rangle\sigma} (c^{\dagger}_{i\sigma} c_{j\sigma} + \mathrm{H.c.}) + U \sum_{i} n_{i\uparrow} n_{i\downarrow} + \sum_{\mathbf{q}} \omega_{\mathbf{q}} b^{\dagger}_{\mathbf{q}} b_{\mathbf{q}} + \sum_{\mathbf{q}} g_{\mathbf{q}} (b^{\dagger}_{\mathbf{q}} + b_{-\mathbf{q}}) \rho_{\mathbf{q}} \,,$$

where local electron-phonon interactions are replaced by long-range interactions, the phonon dispersion is taken into account, and electron-electron Coulomb interactions play a crucial role in the emergent phenomena. Here, $\rho_{\mathbf{q}} = \sum_{\mathbf{k},\sigma} c^{\dagger}_{\mathbf{k}+\mathbf{q},\sigma} c_{\mathbf{k},\sigma}$. In chapter 3 we rigorously obtain the Hubbard-Holstein (HH) model and its extended family from second quantization of a general classical model that takes into account all electronic and ionic motion and the interactions between each of its constituents under a series of approximations. The study of extended HH models via quantum simulation protocols and innovative numerical techniques is given by chapter 6.

1.3 Efficient techniques

The quest for theoretical understanding of strongly correlated many-body systems is known to be extremely challenging. Classical simulation methods can become inefficient as the Hilbert space becomes too large to effectively sample. The number of parameters needed to describe and store a quantum state grows exponentially with the system size. The situation becomes even more involved when dealing with composite (hybrid) systems. Hybrid systems, such as electrons and phonons or atoms and light, combine distinct components, Fermions and Bosons, each with unique nature and demands, posing significant challenges to numerical methods. Fermionic degrees of freedom exhibit strong correlations that require many-body techniques [143, 144, 146, 83] or quantum computational approaches [39, 27, 21]. Bosonic systems, on the other hand, belong to an infinite-dimensional Hilbert space with possibly large occupation numbers, where variational methods can be effective [58, 24]. While these methods have proven effective in isolated systems, they are limited when applied to hybrid systems. Such kind of strongly correlated materials can feature a competition between different processes, which drives the system towards to complex phases that cannot be captured by perturbative methods because of the lack of a small parameter. Computational methods such as exact diagonalization (ED), quantum Monte Carlo (QMC), and density matrix renormalization group (DMRG), greatly advanced the understanding of many-body systems. However, as the phonon Hilbert space has to be truncated, numerical studies typically allow only a small phonon number and system size. For instance, competition between electron-electron and electron-phonon interactions, in the Hubbard-Holstein model, can lead to rich phase diagrams and strongly correlated ground states. Phonon-mediated attraction between electrons can enhance fermion pairing even when the Coulomb repulsion is strong [3, 82]. In light-matter photon induces effective long-ranged (all-to-all) interactions between the atoms that compete with short-range couplings. Theoretical treatment of such multicomponent models turns out to be a nontrivial task. For separable energy scales, one can rely on perturbative expansions or approximate decoupling approaches such as the Holstein-Primakoff transformation [112, 134]. However, for competing processes, numerical techniques are typically required. For example, as the ground state of the Dicke model in the strong coupling regime is well represented by the coherent state for the photonic part, approaches working in Fock space suffer from its infinite Hilbert space dimension that requires truncation, making exact diagonalization (ED) or tensor network methods ineffective. Simulations based on phase-space representations such as truncated Wigner method can be more reliable in describing large QED setups [67, 107]. On the other hand, due to the presence of competing orders in hybrid systems, simple variational ansätze based on *a priori* intuitions could introduce bias to the conclusion. For instance, separable state assumptions followed by tracing out the infinity bosonic Hilbert space cannot capture the intricate correlations of the system.

Quantum computers hold the promise to overcome this difficulty, but near-term devices cannot be expected to provide the needed number of logical qubits and sufficient circuit depth. For these reasons, analog quantum simulators are among the most promising tools to study ground state properties as well as dynamics of interacting quantum systems [25, 55, 45]. As the approach of analog simulation is to construct a controllable system that can reproduce the physics of a different one, it is nonuniversal and thus the details of experimental implementation matter. The platforms for quantum simulation must feature some versatility in tuning the system parameters, scalability in the number of qubits, and reliable measurement schemes. Over the past two decades, a wide range of promising quantum devices that may have some of the desired properties has emerged [6]. Among the various platforms available, ultracold neutral atoms [17] and Rydberg atom arrays [13] received a lot of attention in this respect. A hybrid approach involving a combination of setups can be promising as well, allowing for easier implementation of more complex systems with potentially independently tunable properties [15]. A number of theoretical proposals for quantum simulation of electron-phonon models using molecules as well as ions exists [113, 108, 59, 68]. However, they have stringent requirements and can lack versatility. For example, in order to crystallize the molecules one needs extremely low temperatures, while in ion-atom systems the relevant energy scales are quite separated. Here we focus on a different type of mixture involving an array of Rydberg atoms and a ground state gas. In most experimental realizations, the Rydberg states are repelled by optical traps and the laser field must be turned off during experiments. However, recent developments allow for keeping the tweezer array on as well as to achieve state-insensitive traps [148, 95], leading to long lifetimes and opening the door towards a new simulation platform. In chapter 6 we propose a hybrid setup involving two species: Rydberg atoms, that are pinned by optical tweezers by are allowed to perform small displacements from equilibrium, and neutral atoms that are free to move but feel the presence of the Rydberg atomic array as a background lattice potential. We show that this platform is efficient for simulating a class of extended Hubbard-Holstein models.

Another way to circumvent these challenges is to develop novel efficient numerical techniques that are specifically designed to tackle the problem. By utilizing a hybrid variational approach [127, 138] designed to work for general electron-phonon systems regardless of the Hamiltonian details, we study the Hubbard-Holstein model in chapter 6. In this approach, the bosonic part of the wavefunction is approximated by a Gaussian state, and optimized variationally. The fermionic part of the system is on the other hand treated numerically exactly via exact diagonalization or density matrix renormalization group (DMRG) methods. The key component is a suitable entangling operation added in order to include possible correlations between the subsystems. The goal of this numerical study was to probe the method for the simplest case of electron-phonon and electron-electron interaction model, to finally move to the study of extended Hubbard-Holstein models with intricate properties, such as the model that we obtained in 6.1. Related works show that the approach works well for extended Hubbard-Holstein models [138, 137, 139, 31], where it very accurately reproduced state-of-the-art numerical results. Even though this hybrid approach was initially designed for electron-phonon systems, extensions for distinct types of multicomponent systems seem viable. In order to study the Dicke-Heisenberg model, the model that includes both strong spin-spin and spin-photon interactions, we adapted the hybrid numerical method to work for a general class of spin-photon systems where the photonic part of the wavefunction that optimized variationally is treated as a Gaussian state, reflecting the Dicke model solution at strong coupling. The spin part of the system is on the other hand treated numerically exactly via DMRG. The entangling transformation for the electron-phonon systems is a parametrized Lang-Firsov transformation. Thus, we designed a dressing transformation where the transverse spin operator works as the electronic density. This adapted hybrid numerical approach shows to be very efficient, where it reproduces the Dicke model in the thermodynamic limit and its finite-size effects depending on the choice of the variational ansatz. We show in chapter 7 a thorough analysis of spin-photon systems with both isotropic and anisotropic spin-spin interactions. The spin exchange fundamentally alters the phase landscape of the Dicke model, where we observe enhanced superradiance, distinct phase transitions, and coexistence between superradiance and spin order.

This thesis is primarily based on the following articles: *Quantum simulation of extended electron–phonon-coupling models in a hybrid Rydberg atom setup*, Phys. Rev. A **107**, 032808 (2023); *The role of exchange interactions in the superradiant phenomena*, arXiv:2503.04961 (2024); *A variational non-Gaussian approach to cavity QED with strongly interacting emitters*, In preparation. In these works, the author had the leading contribution and performed all the derivations and calculations. The results presented in this thesis represent the original research carried out by the author during his PhD studies, developed under the guidance of his supervisor and in close collaboration with his colleagues.

2

Light-matter Systems

Cavity quantum electrodynamics (cQED) systems are among the most prominent platforms for quantum computing, quantum simulation, and quantum devices. Atoms provide robust carriers of information due to their well-defined energy levels, while photons, with their high degree of coherence, are ideal for transmitting information over long distances. This synergy makes hybrid light-matter systems promising candidates for large-scale quantum computing and the realization of the quantum internet [74]. However, achieving strong atom-light interactions requires extremely small cavity volumes, which complicates experimental control [2], making it challenging in terms of scalability and controllability. Despite their applicability potential, cQED systems are intrinsically difficult to understand at a fundamental level, due to the distinct and competing nature of its components. As recognized by the 2012 Nobel Prize in Physics awarded to Serge Haroche and David J. Wineland [60, 149], the study of such systems is of vital importance, not only due to future application advancements, but also to fundamental understanding of light-matter interacting systems. In this chapter, we focus on the second quantization of the electromagnetic light field in a microcavity, and of the light-matter interaction under certain approximations, ultimately obtaining the quantum Hamiltonian of interest. In the next chapters, we will study a class of light-matter systems derived from this Hamiltonian, developing a novel numerical method to address the aforementioned challenges.

2.1 Quantization of the electromagnetic field

Before studying the quantum theory of light-matter interaction, we need to quantize the electromagnetic field in a cavity. This is a special application of second quantization [5]. Let us begin by recalling Maxwell's equations with sources

$$\begin{aligned} \boldsymbol{\nabla} \cdot \mathbf{E} &= \frac{\rho}{\varepsilon_0}, & \boldsymbol{\nabla} \cdot \mathbf{B} &= 0, \\ \boldsymbol{\nabla} \times \mathbf{E} &= -\frac{\partial \mathbf{B}}{\partial t}, & \boldsymbol{\nabla} \times \mathbf{B} &= \mu_0 \epsilon_0 \frac{\partial \mathbf{E}}{\partial t} + \mu_0 \mathbf{J}. \end{aligned} \tag{2.1}$$

The fields can be expressed in terms of potentials. Since the divergence of the magnetic induction field is zero, it can be written in terms of a vector potential $\mathbf{A}$ via

$$\mathbf{B} = \boldsymbol{\nabla} \times \mathbf{A}. \tag{2.2}$$

The electric field can also be written in terms of both scalar and vector potentials as

$$\mathbf{E} = -\boldsymbol{\nabla}\phi - \frac{\partial \mathbf{A}}{\partial t}. \tag{2.3}$$

That way, one can describe the system solely in terms of ϕ and $\mathbf{A}$, leading to

$$\left(\nabla^2 \mathbf{A} - \mu_0 \varepsilon_0 \frac{\partial^2 \mathbf{A}}{\partial t^2}\right) - \boldsymbol{\nabla}\left(\boldsymbol{\nabla} \cdot \mathbf{A} + \mu_0 \varepsilon_0 \frac{\partial \phi}{\partial t}\right) = -\mu_0 \mathbf{J} \tag{2.4a}$$

$$\nabla^2 \phi + \frac{\partial}{\partial t}\left(\boldsymbol{\nabla} \cdot \mathbf{A}\right) = -\frac{\rho}{\varepsilon_0}. \tag{2.4b}$$

These two equations encapsulate all the information in Maxwell's equations, showing that we can work solely with potentials.

2.1.1 Non-Uniqueness of Potentials and Gauge Transformations

The potentials obtained are not unique. Observe that we can perform the following transformations without altering the fields $\mathbf{E}$ and $\mathbf{B}$:

$$\phi \to \phi + \beta, \tag{2.5a}$$

$$\mathbf{A} \to \mathbf{A} + \boldsymbol{\nabla}\chi, \tag{2.5b}$$

where β is constant in space. The fields remain invariant under these transformations because $\boldsymbol{\nabla}\beta = 0$ and $\boldsymbol{\nabla} \times (\boldsymbol{\nabla}\chi) = 0$. The gauge transformation relates β and $\boldsymbol{\nabla}\chi$ by considering that the transformations yield the same electric field,

$$\boldsymbol{\nabla}\beta + \frac{\partial}{\partial t}\left(\boldsymbol{\nabla}\chi\right) = 0 \Rightarrow \boldsymbol{\nabla}\left(\beta + \frac{\partial \chi}{\partial t}\right) = 0,$$

we conclude that $\beta = -\, \partial\chi/\partial t$. Hence,

$$\phi' = \phi - \frac{\partial \chi}{\partial t}, \tag{2.6a}$$

$$\mathbf{A}' = \mathbf{A} + \boldsymbol{\nabla}\chi, \tag{2.6b}$$

the potentials $(\phi', \mathbf{A}')$ and $(\phi, \mathbf{A})$ produce the same fields $\mathbf{E}$ and $\mathbf{B}$. This is the gauge transformation, which is invariant. In classical electromagnetism, the choice of χ is often used to simplify calculations. In this work, we focus on the Coulomb gauge, where χ is chosen such that $\boldsymbol{\nabla} \cdot \mathbf{A} = 0$. This implies that ϕ will reflect all variations in ρ, since

$$\nabla^2 \phi = -\frac{\rho}{\varepsilon_0}, \tag{2.7}$$

i.e., the scalar potential ϕ can be written in terms of the source

$$\phi(\mathbf{x},t) = \frac{1}{4\pi\varepsilon_0}\int \frac{\rho(\mathbf{x}',t)}{|\mathbf{x}-\mathbf{x}'|}\,\mathrm{d}^3x'\,. \tag{2.8}$$

When there is no source, the scalar potential is zero. Another implication of the Coulomb gauge comes from the fact that any vector field that vanishes sufficiently quickly at infinity can be decomposed into its rotational and irrotational components as[1]

$$\mathbf{A} = \mathbf{A}_\perp + \mathbf{A}_\parallel, \tag{2.9}$$

where $\boldsymbol{\nabla}\cdot\mathbf{A}_\perp = 0$ and $\boldsymbol{\nabla}\times\mathbf{A}_\parallel = 0$. In this case, this is equivalent to separating the transverse and longitudinal parts. Thus we note that the Coulomb gauge considers a transverse vector potential, $\mathbf{A} \equiv \mathbf{A}_\perp$ (rotational field).

2.1.2 Quantization of the Radiation Field Hamiltonian

Let us start by performing a Fourier decomposition of the vector potential in a cubic volume $V = L^3$ with periodic boundary conditions. At $t = 0$,

$$\mathbf{A}(\mathbf{x},t=0) = \frac{1}{\sqrt{V}}\sum_{\mathbf{k}}\sum_{\alpha=1}^{2}\left(\boldsymbol{\epsilon}^{(\alpha)}c_{\mathbf{k},\alpha}(t=0)e^{i\mathbf{k}\cdot\mathbf{x}} + \boldsymbol{\epsilon}^{*(\alpha)}c^*_{\mathbf{k},\alpha}(t=0)e^{-i\mathbf{k}\cdot\mathbf{x}}\right), \tag{2.10}$$

where $c_{\mathbf{k},\alpha}$ are the expansion coefficients, $\mathbf{k}$ is the wave vector with $k_i = 2\pi n_i/L$ $(i = x, y, z)$, $1/\sqrt{V}$ arises from the normalization of the plane waves, and $\boldsymbol{\epsilon}^{(\alpha)}$ are two polarization vectors that satisfy orthonormality relations. Polarization vectors can have Cartesian directions x and y (making them real), where $\boldsymbol{\epsilon}^{x,y}\cdot\mathbf{k} = 0$. They can also represent circular polarizations (making them complex), expressed in terms of $\boldsymbol{\epsilon}^x$ and $\boldsymbol{\epsilon}^y$.

Maxwell's equations in the Coulomb gauge, assuming no source, becomes simple: $\Box A^\mu = 0$. Thus, the temporal dependence is given by

$$c_{\mathbf{k},\alpha}(t) = c_{\mathbf{k},\alpha}(0)e^{-i\omega t}, \quad \text{where } \omega = c|\mathbf{k}|.$$

The vector potential can then be written as

$$\mathbf{A}(\mathbf{x},t) = \frac{1}{\sqrt{V}}\sum_{\mathbf{k}}\sum_{\alpha=1}^{2}\left(\boldsymbol{\epsilon}^{(\alpha)}c_{\mathbf{k},\alpha}(t)e^{i\mathbf{k}\cdot\mathbf{x}} + \boldsymbol{\epsilon}^{*(\alpha)}c^*_{\mathbf{k},\alpha}(t)e^{-i\mathbf{k}\cdot\mathbf{x}}\right). \tag{2.11}$$

Explicitly including the temporal dependence of $\mathbf{A}$ and keeping time-independent coefficients $c_{\mathbf{k},\alpha}(0) \equiv c_{\mathbf{k},\alpha}$, we can write in the covariant form, which makes the calculations much easier,

$$A^\mu = \frac{1}{\sqrt{V}}\sum_{\mathbf{k}}\sum_{\alpha=1}^{2}\epsilon^{(\alpha)}_\mu c_{\mathbf{k},\alpha}e^{ik_\rho x^\rho} + \text{c.c.}, \tag{2.12}$$

where the inner product is $k_\mu x^\mu = \mathbf{k}\cdot\mathbf{x} - \omega t$.

---

[1] This was proven by Helmholtz in 1858 [61], in the context of hydrodynamics.

The local Hamiltonian can be expressed in terms of the tensorial field $F^{\mu\nu}$ and A^{μ} as

$$\mu_0 \mathcal{H} = F_{\mu 0}\partial^0 A^{\mu} + \frac{1}{4} F_{\mu\nu}F^{\mu\nu}, \tag{2.13}$$

with the total Hamiltonian given by $H = \int \mathrm{d}^3x\, \mathcal{H}$. After some algebra, $\mathcal{H}$ can be simplified to

$$\mu_0 \mathcal{H} = -\partial^0 A^{\mu} \partial^0 A^{\mu}. \tag{2.14}$$

Thus, the total Hamiltonian, in terms of $c_{\mathbf{k},\alpha}$, reads

$$H = \varepsilon_0 \sum_{\mathbf{k},\alpha} \omega^2 \left[c_{\mathbf{k},\alpha} c^*_{\mathbf{k},\alpha} + c^*_{\mathbf{k},\alpha} c_{\mathbf{k},\alpha} \right]. \tag{2.15}$$

This Hamiltonian resembles a collection of uncoupled oscillators, one for each $\mathbf{k}$ and α, by defining the coordinates

$$Q_{\mathbf{k},\alpha} = \sqrt{\varepsilon_0}(c_{\mathbf{k},\alpha} + c^*_{\mathbf{k},\alpha}), \tag{2.16}$$

and the corresponding conjugate momenta

$$P_{\mathbf{k},\alpha} = -i\omega\sqrt{\varepsilon_0}(c_{\mathbf{k},\alpha} - c^*_{\mathbf{k},\alpha}). \tag{2.17}$$

This change of variables gives rise to the usual form of the harmonic oscillator Hamiltonian

$$H = \frac{1}{2} \sum_{\mathbf{k},\alpha} \left[P^2_{\mathbf{k},\alpha} + \omega^2 Q^2_{\mathbf{k},\alpha} \right], \tag{2.18}$$

where $Q_{\mathbf{k},\alpha}$ and $P_{\mathbf{k},\alpha}$ satisfy the Hamilton equations.

Second quantization involves replacing $Q_{\mathbf{k},\alpha}$ and $P_{\mathbf{k},\alpha}$ with quantum operators $\hat{Q}_{\mathbf{k},\alpha}$ and $\hat{P}_{\mathbf{k},\alpha}$ satisfying the commutation relations

$$[\hat{Q}_{\mathbf{k},\alpha}, \hat{P}_{\mathbf{k}',\alpha'}] = i\hbar \delta_{\mathbf{k},\mathbf{k}'} \delta_{\alpha,\alpha'}, \tag{2.19a}$$

$$[\hat{Q}_{\mathbf{k},\alpha}, \hat{Q}_{\mathbf{k}',\alpha'}] = 0, \tag{2.19b}$$

$$[\hat{P}_{\mathbf{k},\alpha}, \hat{P}_{\mathbf{k}',\alpha'}] = 0. \tag{2.19c}$$

Following the equations above, we can express the Fourier coefficients $c_{\mathbf{k},\alpha}$ and $c^*_{\mathbf{k},\alpha}$ in terms of the creation and annihilation operators that satisfy $[\hat{a}_{\mathbf{k},\alpha}, \hat{a}^{\dagger}_{\mathbf{k}',\alpha'}] = \delta_{\mathbf{k},\mathbf{k}'}\delta_{\alpha,\alpha'}$,

$$c_{\mathbf{k},\alpha} = \sqrt{\frac{\hbar}{2\varepsilon_0 \omega}} \hat{a}_{\mathbf{k},\alpha}, \tag{2.20a}$$

$$c^*_{\mathbf{k},\alpha} = \sqrt{\frac{\hbar}{2\varepsilon_0 \omega}} \hat{a}^{\dagger}_{\mathbf{k},\alpha}. \tag{2.20b}$$

The quantum Hamiltonian for each oscillator reads

$$\hat{H}_{\mathbf{k},\alpha} = \hbar\omega \left(\hat{a}^{\dagger}_{\mathbf{k},\alpha} \hat{a}_{\mathbf{k},\alpha} + \frac{1}{2} \right). \tag{2.21}$$

Finally, the second quantized fields of interest, written in relativistic notation, become

$$\hat{A}^\mu = \frac{1}{\omega} \sum_{\mathbf{k},\alpha} \varepsilon_{\mathbf{k}} \epsilon_\mu^{(\alpha)} \hat{a}_{\mathbf{k},\alpha} e^{ik_\rho x^\rho} + \text{H.c.}, \tag{2.22a}$$

$$\hat{E}^\mu = i \sum_{\mathbf{k},\alpha} \varepsilon_{\mathbf{k}} \epsilon_\mu^{(\alpha)} \hat{a}_{\mathbf{k},\alpha} e^{ik_\rho x^\rho} - \text{H.c.}, \tag{2.22b}$$

where $\varepsilon_{\mathbf{k}}$ is a scalar with dimensions of electric field,

$$\varepsilon_{\mathbf{k}} = \sqrt{\frac{\hbar\omega_{\mathbf{k}}}{2V\varepsilon_0}}, \tag{2.23}$$

with $\omega \equiv \omega_{\mathbf{k}} = c|\mathbf{k}|$.

This completes the quantization of the electromagnetic field in a cavity, providing the foundational expressions for further study of light-matter interactions. We drop the hat notation from now on.

2.1.3 Photon Statistics

In this section, we will examine some properties of the operators a and $a^\dagger$, define the Fock states and a coherent state. With knowledge of photon statistics, we can investigate the quantum behavior of the electromagnetic field. Since the Hamiltonian has been reduced to a set of uncoupled harmonic oscillators, we will, from now on, omit the $(\mathbf{k}, \alpha)$ indices and study the properties of a single harmonic oscillator in the context of photon statistics.

The Fock states are the eigenstates of the cavity field Hamiltonian H_c, defined via

$$H_\text{c} |n\rangle = \hbar\omega \left(a^\dagger a + \frac{1}{2} \right) |n\rangle = E_n |n\rangle . \tag{2.24}$$

We note that the states $a|n\rangle$ and $a^\dagger|n\rangle$ are also eigenstates of H_c, since $H_\text{c} a|n\rangle = (E_n - \hbar\omega) a|n\rangle$. That is, the state $a|n\rangle$ is an eigenstate of the Hamiltonian with energy $-\hbar\omega$ relative to the state $|n\rangle$. The operator a is called the annihilation operator because it removes one quantum of energy when applied. For the ground state, $a|0\rangle = 0$, because E_0 is the lowest energy level. Thus,

$$H_\text{c} |0\rangle = \hbar\omega \left(a^\dagger a + \frac{1}{2} \right) |0\rangle = \frac{\hbar\omega}{2} |0\rangle , \tag{2.25}$$

giving $E_0 = \hbar\omega/2$. The discrete energy levels can then be written recursively as $E_{n-1} = E_n - \hbar\omega$ or $E_n = E_{n-1} + \hbar\omega$. Observing this, one defines the bosonic number operator $a^\dagger a = n$, which gives the average number of photons in the cavity $\langle n\rangle = \langle n| a^\dagger a |n\rangle = n$, and the energy can be written as $E_n = \hbar\omega(n + 1/2)$. Following this reasoning, the operator a satisfies

$$|n-1\rangle = \frac{a}{\alpha_n} |n\rangle .$$

where $\alpha_n = \sqrt{n}$ is obtained from orthonormality of the Fock states. Applying the same procedure to $a^\dagger$, we find

$$a^\dagger |n\rangle = \sqrt{n+1}\, |n+1\rangle , \tag{2.26}$$

By applying the above equation n times starting from $|0\rangle$, we obtain

$$|n\rangle = \frac{(a^\dagger)^n}{\sqrt{n!}} |0\rangle . \tag{2.27}$$

This is an important equation that reflects how to go from a vacuum state to any Fock state $|n\rangle$ in terms of the ladder operators.

In summary, the main important characteristics of Fock states are: Fock states form a complete orthonormal set, so $\langle n|m\rangle = \delta_{n,m}$ and $\sum_{n=0}^{\infty} |n\rangle\langle n| = \mathbb{1}$. An arbitrary state vector $|\psi\rangle$ can be expressed as a superposition of eigenstates of the Hamiltonian $|\psi\rangle = \sum_n C_n |n\rangle$. The operators a and $a^\dagger$ are not Hermitian, but certain combinations are, such as $x = \sqrt{\frac{\hbar}{2\omega}}(a+a^\dagger)$, $p = i\sqrt{\frac{\hbar\omega}{2}}(a-a^\dagger)$, and H_{c}. The only nonzero matrix elements of these operators are $\langle n-1| a |n\rangle = \sqrt{n}$ and $\langle n+1| a^\dagger |n\rangle = \sqrt{n+1}$. Classically, the energy distribution of the electromagnetic field is continuous, but quantum mechanically, the eigenenergies are discrete.

A direct application that shows the quantum nature of the photonic field is related to the fluctuations of the electric field $\langle(\Delta E)^2\rangle$ in vacuum. For a monochromatic electric field with fixed linear polarization,

$$E = i\varepsilon e^{i\mathbf{k}\cdot\mathbf{x}} a - H.c., \tag{2.28}$$

the mean value $\langle n|E|n\rangle = \langle E\rangle$ is clearly zero, while

$$\langle E^2\rangle = \langle n|E^2|n\rangle = \varepsilon^2 \langle n|aa^\dagger + a^\dagger a|n\rangle = \varepsilon^2 (2n+1) .$$

Thus, the field fluctuations,

$$\langle(\Delta E)^2\rangle = \langle E^2\rangle - \langle E\rangle^2 = 2\varepsilon^2 \left(n + \frac{1}{2}\right) . \tag{2.29}$$

In the vacuum state, i.e., for $n = 0$,

$$\langle(\Delta E)^2\rangle = \varepsilon^2. \tag{2.30}$$

The mean value is zero, but fluctuations are present. These vacuum fluctuations lead to various quantum phenomena, such as spontaneous emission and the Lamb shift.

Coherent States

Coherent states are of great importance because of their unique properties. A coherent state is an eigenstate of the annihilation operator[2] $a|\alpha\rangle = \alpha|\alpha\rangle$. To derive the form of this state, we use the completeness of $|n\rangle$ and equation 2.27,

$$|\alpha\rangle = \left(\sum_n |n\rangle\langle n|\right) |\alpha\rangle = \sum_n |n\rangle\langle 0| \frac{a^n}{\sqrt{n!}} |\alpha\rangle = \langle 0|\alpha\rangle \sum_n \frac{\alpha^n}{\sqrt{n!}} |n\rangle .$$

---

[2] While $|\alpha\rangle$ is the eigenket of a, $a^\dagger$ has no eigenket. On the other hand, a has no eigenbra. As non-Hermitian operators, a and $a^\dagger$ share many peculiar properties.

The normalization $\langle\alpha|\alpha\rangle = 1$ gives

$$1 = |\langle 0|\alpha\rangle|^2 \sum_n \frac{(|\alpha|^2)^n}{n!} = |\langle 0|\alpha\rangle|^2 e^{|\alpha|^2},$$

so $\langle 0|\alpha\rangle = \exp(-|\alpha|^2/2)$. Hence, the coherent state can be written as

$$|\alpha\rangle = e^{-\frac{|\alpha|^2}{2}} \sum_n \frac{\alpha^n}{\sqrt{n!}} |n\rangle = e^{-\frac{|\alpha|^2}{2}} \left[\sum_{n=0}^{\infty} \frac{(\alpha\hat{a}^\dagger)^n}{n!}\right] |0\rangle = e^{-\frac{|\alpha|^2}{2}} e^{\alpha\hat{a}^\dagger} |0\rangle .$$

Using the property $e^{-\alpha^*\hat{a}}|0\rangle = |0\rangle$, we obtain

$$|\alpha\rangle = e^{-\frac{|\alpha|^2}{2}} e^{\alpha\hat{a}^\dagger} e^{-\alpha^*\hat{a}} |0\rangle = \exp\big(\alpha\hat{a}^\dagger - \alpha^*\hat{a}\big) |0\rangle . \tag{2.31}$$

This allows us to define the displacement operator as

$$D(\alpha) = \exp\big(\alpha\hat{a}^\dagger - \alpha^*\hat{a}\big), \tag{2.32}$$

which is unitary[3], $D^\dagger(\alpha) = D^{-1}(\alpha)$, and transforms the vacuum state into a coherent state as $D(\alpha)|0\rangle = |\alpha\rangle$. The action of $D(\alpha)$ on the ladder operators then is given by

$$D(\alpha)^\dagger a D(\alpha) = a + \alpha, \tag{2.33a}$$

$$D(\alpha)^\dagger a^\dagger D(\alpha) = a^\dagger + \alpha^*. \tag{2.33b}$$

That way, its action on x and p is written as

$$D(\alpha)^\dagger x D(\alpha) = x + \sqrt{2}\mathrm{Re}(\alpha), \tag{2.34a}$$

$$D(\alpha)^\dagger p D(\alpha) = p + \sqrt{2}\mathrm{Im}(\alpha). \tag{2.34b}$$

Thus, we understand the reason why $D(\alpha)$ is called the *displacement* operator. In phase space, i.e. $\langle x\rangle$–$\langle p\rangle$ plane, the operator displaces the vacuum state, with origin $(\langle x\rangle, \langle p\rangle) = (0, 0)$, to $(\langle x\rangle, \langle p\rangle) = (\sqrt{2}\mathrm{Re}(\alpha), \sqrt{2}\mathrm{Im}(\alpha))$. We intuitively also see that it preserves the uncertainty relation between x and p, which will be proved below.

An equivalent definition for the displacement operator is

$$U_d = \exp(i[\Delta_p x - \Delta_x p]), \tag{2.35}$$

so its action on the operators x and p is given by

$$U_d^\dagger x U_d = x + \Delta_x, \tag{2.36a}$$

$$U_d^\dagger p U_d = p + \Delta_p. \tag{2.36b}$$

Collecting x and p in a vector form, $R = (x, p)^T$, we can write the displacement operator in a compact form via

$$\Delta_p x - \Delta_x p = \begin{pmatrix} x & p \end{pmatrix} \begin{pmatrix} \Delta_p \\ -\Delta_x \end{pmatrix} = \begin{pmatrix} x & p \end{pmatrix} \begin{pmatrix} 0 & 1 \\ -1 & 0 \end{pmatrix} \begin{pmatrix} \Delta_x \\ \Delta_p \end{pmatrix} = R^T \sigma \Delta_R, \tag{2.37}$$

---

[3] It also holds that $D^\dagger(\alpha) = D(-\alpha)$, so $D(\alpha) a D(\alpha)^\dagger = a - \alpha$.

where we defined the displacement vector $\Delta_R = (\Delta_x, \Delta_p)^T$, so that we obtain

$$U_d = \exp\big(iR^T \sigma \Delta_R\big). \tag{2.38}$$

The action of U_d on R is then $U_d^\dagger R U_d = R + \Delta_R$. In the form of Eq. 2.38, the displacement operator can be easily extended to multi-mode systems, as we will see in Chapter 4. For a single-mode system, U_d and $D(\alpha)$ are equivalent and related via $\Delta_R^T = \sqrt{2}(\mathrm{Re}(\alpha), \mathrm{Im}(\alpha))^T$.

There is a series of properties of coherent states that follow from the canonical properties mentioned above, including:

1. The average number of photons in a coherent state $|\alpha\rangle$ is given by $\langle n\rangle = |\alpha|^2$.

   Proof:

$$\begin{aligned}\langle\alpha|n|\alpha\rangle = \ &\langle\alpha|a^\dagger a|\alpha\rangle = e^{-|\alpha|^2}\sum_{n=0}^{\infty}\frac{(|\alpha|^2)^n}{n!}n \\ &= e^{-|\alpha|^2}|\alpha|^2\frac{\partial}{\partial|\alpha|^2}e^{|\alpha|^2} \\ &= |\alpha|^2.\end{aligned} \tag{2.39}$$

2. The probability of finding n photons follows a Poisson distribution.

   Proof:

$$P(n) = |\langle n|\alpha\rangle|^2 = \frac{e^{-|\alpha|^2}|\alpha|^{2n}}{n!} = \frac{\langle n\rangle^n e^{-\langle n\rangle}}{n!}. \tag{2.40}$$

3. Coherent states are not orthogonal, but they are normalized.

   Proof:

$$\langle\alpha|\alpha\rangle = e^{-|\alpha|^2}\sum_n \frac{(|\alpha|^2)^n}{n!} = 1, \tag{2.41a}$$

$$\langle\alpha|\beta\rangle \neq 0 \Rightarrow |\langle\alpha|\beta\rangle|^2 = e^{-|\alpha-\beta|^2}. \tag{2.41b}$$

4. Coherent states minimize the uncertainty relation, $\Delta x \Delta p = \hbar/2$.

   Proof: Recall that the non-Hermitian operators a and $a^\dagger$ can be combined to write x and p,

$$\frac{1}{2}(a + a^\dagger) = \sqrt{\frac{\omega}{2\hbar}}x, \tag{2.42a}$$

$$\frac{1}{2i}(a - a^\dagger) = \sqrt{\frac{1}{2\hbar\omega}}p. \tag{2.42b}$$

   These satisfy the commutation relation $[x, p] = i\hbar$. The uncertainty relation holds

$$\Delta x \Delta p \geq \frac{\hbar}{2}. \tag{2.43}$$

For a coherent state $|\alpha\rangle$, the variances are

$$\begin{aligned} \langle (\Delta x)^2 \rangle &= \frac{\hbar}{2\omega}, \\ \langle (\Delta p)^2 \rangle &= \frac{\hbar\omega}{2}. \end{aligned}$$

Multiplying these gives

$$\Delta x \Delta p = \sqrt{\frac{\hbar}{2\omega} \cdot \frac{\hbar\omega}{2}} = \frac{\hbar}{2}. \tag{2.44}$$

These properties make coherent states crucial for understanding quantum optics and the quantum behavior of electromagnetic fields. In the Jaynes-Cummings model, the most basic quantum ligh-matter interaction model, the coherent states are responsible for a pure quantum phenomena called collapse and revival [129].

2.2 Quantization of the light-matter interactions

The classical Hamiltonian of the atom (or molecule) is given by

$$H = \frac{\mathbf{p}^2}{2m} + V(\mathbf{x}), \tag{2.45}$$

where the potential $V(\mathbf{x})$ can be Coulomb-like. When interacting with an external field, the operators transform as

$$\mathbf{p} \to \mathbf{p} - e\mathbf{A}, \tag{2.46a}$$

$$H \to H + e\phi, \tag{2.46b}$$

so that the Hamiltonian of an atom interacting with an external electromagnetic field becomes

$$\begin{aligned} H &= \frac{1}{2m}(\mathbf{p} - e\mathbf{A})^2 + V(\mathbf{x}) + e\phi \\ &= \frac{\mathbf{p}^2}{2m} + \frac{e^2}{2m}\mathbf{A}^2 - \frac{e}{2m}(\mathbf{A}\cdot\mathbf{p} + \mathbf{p}\cdot\mathbf{A}) + V(\mathbf{x}). \end{aligned} \tag{2.47}$$

There are several ways to address the above Hamiltonian. We show two approaches based on the Coulomb gauge, where $\boldsymbol{\nabla}\cdot\mathbf{A} = 0$ and $\phi = 0$ (source-free). First, consider the following application to a scalar function $f(\mathbf{x})$, knowing that $\mathbf{p} = -i\hbar\nabla$,

$$\begin{aligned} (\mathbf{A}\cdot\mathbf{p} - \mathbf{p}\cdot\mathbf{A})f(\mathbf{x}) &= \frac{\hbar}{i}\big(\boldsymbol{\nabla}\cdot\mathbf{A} - \mathbf{A}\cdot\boldsymbol{\nabla}\big)f(\mathbf{x}) \\ &= \frac{\hbar}{i}\big[(\boldsymbol{\nabla}\cdot\mathbf{A})f + (\boldsymbol{\nabla}f)\cdot\mathbf{A} - \mathbf{A}\cdot(\boldsymbol{\nabla}f)\big] \\ &= \frac{\hbar}{i}(\boldsymbol{\nabla}\cdot\mathbf{A})f, \end{aligned}$$

where, in the Coulomb gauge, the result is zero, leading to $\mathbf{A}\cdot\mathbf{p} = \mathbf{p}\cdot\mathbf{A}$. The term involving $\mathbf{A}^2$ can be neglected if $\mathbf{A}\cdot\mathbf{p}$ is comparatively much larger. Thus,

$$H = \frac{\mathbf{p}^2}{2m} + V(\mathbf{x}) - \frac{e}{m}\mathbf{A}\cdot\mathbf{p}, \tag{2.48}$$

where the last term represents the atom-field interaction.

Another way to write the Hamiltonian involves expressing the interaction in terms of the electric dipole form. Considering the electric dipole approximation, $\mathbf{A}(\mathbf{x}, t) \to \mathbf{A}(t)$, we take the Hamiltonian in the Coulomb gauge and perform another gauge transformation as

$$H = \frac{1}{2m}\left[\mathbf{p} - e(\mathbf{A} + \boldsymbol{\nabla}\chi)\right]^2 - e\frac{\partial\chi}{\partial t} + V(\mathbf{x}), \tag{2.49}$$

choosing χ such that

$$\begin{aligned} \chi(\mathbf{x}, t) = -\mathbf{A}\cdot\mathbf{x} \quad \Rightarrow \quad & \boldsymbol{\nabla}\chi = -\mathbf{A}, \\ & \frac{\partial\chi}{\partial t} = -\frac{\partial\mathbf{A}}{\partial t}\cdot\mathbf{x} = \mathbf{E}\cdot\mathbf{x}. \end{aligned}$$

This implies that the Hamiltonian can be written as the sum of the atomic Hamiltonian and the electric dipole interaction

$$H = \frac{\mathbf{p}^2}{2m} + V(\mathbf{x}) - \mathbf{d}\cdot\mathbf{E}, \tag{2.50}$$

where $\mathbf{d} = e\mathbf{x}$ is the electric dipole moment. There is an equivalence between these two representations, as the regime where $\mathbf{A}^2$ is negligible coincides with the regime where the electric dipole approximation can be applied. Neglecting the $\mathbf{A}^2$ term, however, may lead to several physical implications. Rzażewski et. al. [121] studied the second quantized versions of Hamiltonians 2.47 and 2.50 and concluded that the absence of the $\mathbf{A}^2$ term is required to obtain a superradiance phase transition. This conclusion leads to what is now called a *no-go theorem* [14], which does not destroy the validity of the Dicke model, as many platforms have been proposed to engineer effective two-level systems with weak $\mathbf{A}^2$ out of multi-level atom systems with tunable transition frequencies or at the right geometry [100, 136, 135].

2.2.1 Second quantized description

The part of the Hamiltonian 2.50 that represents the pure atomic part can be represented quantum mechanically in various ways depending on the system of interest. In this work, we will focus on a case where the system of interest is a non-interacting collection of two-level systems[4]. Since there is no classical analog for spin, there is no need to address second quantization in this context. Let us now focus on the quantization of the interaction Hamiltonian.

---

[4] The potential part of the atomic Hamiltonian can represent spin-spin interactions, which will be taken into consideration in later chapters.

Two-Level Systems Recap

A two-level quantum system is described by a two-dimensional Hilbert space with basis states $|e\rangle$ and $|g\rangle$, corresponding to eigenenergies E_e and E_g, respectively. These states form a complete orthonormal set $\langle e|g\rangle = 0, \langle e|e\rangle = \langle g|g\rangle = 1, \mathbb{1} = |e\rangle\langle e| + |g\rangle\langle g|$.
The Hamiltonian in the energy eigenstate basis is written as: $H_a = E_e\,|e\rangle\langle e| + E_g\,|g\rangle\langle g|$. Introducing the energy difference $\hbar\omega_0 = E_e - E_g$ and rescaling, we have

$$H_a = \frac{\hbar\omega_0}{2}\sigma^z, \tag{2.51}$$

where $\sigma^z = |e\rangle\langle e| - |g\rangle\langle g|$ is the Pauli z operator.
In a two-dimensional space, we define the complete set of independent operators

$$\mathbb{1} = |e\rangle\langle e| + |g\rangle\langle g|\,, \quad \sigma^z = |e\rangle\langle e| - |g\rangle\langle g|\,, \; \sigma^+ = |e\rangle\langle g|\,, \quad \sigma^- = |g\rangle\langle e|\,, \tag{2.52}$$

where σ^+ and σ^- are the fermionic creation and annihilation operators satisfying the anti-commutation relations

$$\{\sigma^+, \sigma^-\} = \mathbb{1}, \; \{\sigma^+, \sigma^+\} = \{\sigma^-, \sigma^-\} = 0. \tag{2.53}$$

Let us consider a generic two-level system with states $|g\rangle$ and $|e\rangle$. The dipole moment operator $\mathbf{d}$ in this basis states can be written as

$$\mathbf{d} = \mathbf{d}_{gg}\,|g\rangle\langle g| + \mathbf{d}_{ee}\,|e\rangle\langle e| + \mathbf{d}_{ge}\,|g\rangle\langle e| + \mathbf{d}_{eg}\,|e\rangle\langle g|\,, \tag{2.54}$$

where $\mathbf{d}_{ij} = \langle i|\,\mathbf{d}\,|j\rangle$. When dealing with a two-level system, the projections $|i\rangle\langle j|$ can be written in terms of the Pauli matrices, as in Eqs. 2.52. Thus, the dipole moment operator becomes

$$\mathbf{d} = \mathbf{d}_0\mathbb{1} + \mathbf{d}_z\sigma^z + \mathbf{d}_y\sigma^y + \mathbf{d}_x\sigma^x, \tag{2.55}$$

where $\mathbf{d}_0 = (\mathbf{d}_{gg} + \mathbf{d}_{ee})/2$, $\mathbf{d}_z = (\mathbf{d}_{gg} - \mathbf{d}_{ee})/2$, and since the dipole operator is Hermitian $\mathbf{d}_{eg} = \mathbf{d}_{ge}^*$ we have $\mathbf{d}_x = \mathrm{Re}(\mathbf{d}_{ge})$ and $\mathbf{d}_y = -\mathrm{Im}(\mathbf{d}_{ge})$. We note that $\mathbf{d}_0$ is just a global shift, $\mathbf{d}_z$ is the longitudinal contribution, and $\mathbf{d}_{ge}$ is the transition dipole moment. In general, for systems under the electric dipole approximation, the atom has no dipole moment when it is in an energy eigenstate, and we consider the off-diagonal elements real. That way, the operator simplifies to

$$\boxed{\mathbf{d} = \mathbf{d}_{ge}\sigma^x}. \tag{2.56}$$

In the many-atom scenario, we assume $\mathbf{d}$ is homogeneous so that $\mathbf{d} = \sum_i \mathbf{d}_{ge}\sigma_i^x$.

Now, to obtain the quantized interaction Hamiltonian, we remember that the electric field operator in the Coulomb gauge

$$\mathbf{E} = i\sum_{\mathbf{k},\alpha} \boldsymbol{\epsilon}_{\mathbf{k}}^{(\alpha)} \varepsilon_{\mathbf{k}} a_{\mathbf{k},\alpha} e^{i(\mathbf{k}\cdot\mathbf{x} - \omega t)} - \text{H.c}, \tag{2.57}$$

so in $\mathbf{d}\cdot\mathbf{E}$, the dot product selects the $\mathbf{d}_{ge}$ component based on the polarization $\boldsymbol{\epsilon}_{\mathbf{k}}^{(\alpha)}$. Thus,

$$H_I = -\mathbf{d}\cdot\mathbf{E} = -i\sum_{\mathbf{k},\alpha,i} \lambda_{\mathbf{k},\alpha}\sigma_i^x a_{\mathbf{k},\alpha} e^{i(\mathbf{k}\cdot\mathbf{x} - \omega t)} - \text{H.c}, \tag{2.58}$$

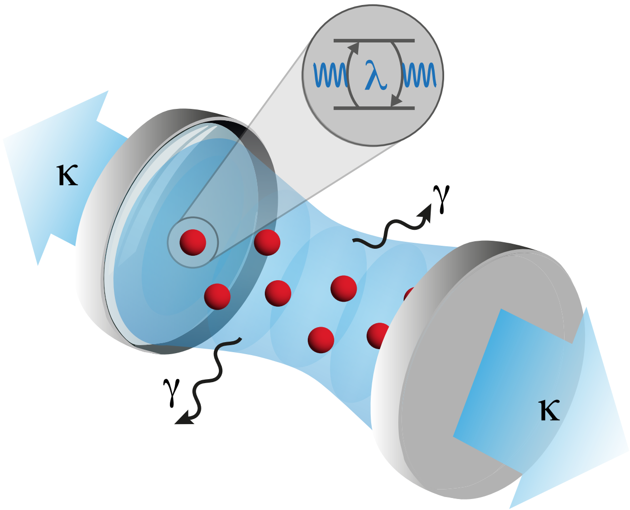

Figure 2.1: Cartoon representation of the considered model. The system is composed of an ensemble of two-level quantum systems (TLSs) in an optical cavity. Each TLS has a separation ω_0 between the two states and is interacting with the cavity field with a interaction strength λ. The decoherence effects κ and γ happen at a much slower rate than the coupling λ.

with the atom-photon interaction strength given by

$$\lambda_{\mathbf{k},\alpha} = \sqrt{\frac{\hbar\omega_{\mathbf{k}}}{2V\varepsilon_0}}(\mathbf{d}_{ge} \cdot \boldsymbol{\epsilon}_{\mathbf{k}}^{(\alpha)}). \tag{2.59}$$

This is the usual form of the interaction strength obtained in the SI units, which may differ especially old articles or textbooks where the CGS is used and some approximations are taken beforehand.

We can explore a few transformations and approximations to transform this Hamiltonian into a more usual and compact form. This Hamiltonian comes from the long-wavelength limit (dipole approximation), where $\mathbf{k} \cdot \mathbf{r} \approx 0$, so $e^{\mathbf{k}\cdot\mathbf{r}} \approx 1$ to maintain consistence with the approximations. The time-dependence given by $e^{i\omega t}$ can be removed in the interaction picture via rotating wave approximation (RWA), where we neglect fast rotating terms with $e^{\pm i(\omega+\omega_0)t}$ and keep dominant terms with $e^{\pm i\Delta t}$, where $\Delta = \omega - \omega_0$ is the detuning which is set to zero (resonant condition). These transformations to obtain the time-independent model have no physical consequences if the system is closed. Finally, one can use $U(1)$ transformations (global phase), e.g. $a \to e^{i\phi}a$ with $\phi = \pi/2$, to remove the imaginary unit and swap the signs in the Hamiltonian.

The interaction Hamiltonian in its final form is written as

$$H_I = \sum_{\mathbf{k},\alpha,i} \lambda_{\mathbf{k},\alpha}\sigma_i^x(a_{\mathbf{k},\alpha} + a_{\mathbf{k},\alpha}^\dagger). \tag{2.60}$$

The schematic representation of an optical cavity interacting with a collection of two-level atoms is shown in Figure 2.1. In the calculations above, we considered a closed system, however, there are two main components that cause losses in the system. First, the cavity is not perfectly sealed, leading to a non-zero probability of photon leakage from the cavity at a rate κ. Second, there is a finite probability, proportional to γ, of light leakage due to the spontaneous emission of photons from the atom's excited state. In this work, we explicitly neglect all dissipation processes by assuming that λ is significantly greater than the loss rates,

$$\boxed{\frac{\lambda^2}{2\gamma\kappa} \gg 1}, \tag{2.61}$$

which implies that the timescales of atom-field interactions are much larger than the timescale at which losses become significant. This assumption is known in the literature as the strong coupling regime.

3

Electron-phonon Systems

Electron-phonon systems describe the interactions between electrons and the vibrational modes of a crystal lattice. These interactions are fundamental in determining various material properties, such as electrical resistivity and thermal conductivity, and play a crucial role in phenomena like superconductivity. By studying these systems, we can gain insight into how electrons move through a material and how lattice vibrations influence this motion, thereby deepening our understanding of the underlying mechanisms in condensed matter physics. When studying strongly-interacting materials, the most general model that comes to mind, which we could call "Theory of everything", is given by the combined contributions from ions and electrons. The Hamiltonian is written as

$$H = \underbrace{-\sum_{j=1}^{N} \frac{1}{2m}\nabla_j^2 - \sum_{\alpha=1}^{M} \frac{1}{2M_\alpha}\nabla_\alpha^2}_{\text{kinetic terms}} \underbrace{-\sum_{j=1}^{N}\sum_{\alpha=1}^{M} \frac{Z_\alpha e^2}{|\mathbf{r}_j - \mathbf{R}_\alpha|}}_{\text{electron-ion Coulomb attraction}}$$

$$+ \underbrace{\sum_{\substack{j,k=1 \\ j<k}}^{N} \frac{e^2}{|\mathbf{r}_j - \mathbf{r}_k|}}_{\text{electron-electron Coulomb repulsion}} + \underbrace{\sum_{\substack{\alpha,\beta=1 \\ \alpha<\beta}}^{M} \frac{Z_\alpha Z_\beta e^2}{|\mathbf{R}_\alpha - \mathbf{R}_\beta|}}_{\text{ion-ion Coulomb repulsion}} , \tag{3.1}$$

where m and e is the electron mass and charge, respectively, M_α is the mass of the α-th ion, and $N = \sum_\alpha Z_\alpha$ to have charge neutrality. This Hamiltonian provides a description of a material by explicitly accounting for all contributions from its atomic constituents. In this formulation, both the individual effects of electrons and nuclei and their mutual interactions are incorporated, ensuring that every microscopic interaction within the material is taken into consideration.

In the following, we treat this Hamiltonian with a series of assumptions and approximations to ultimately obtain a tractable Hamiltonian that describes the systems of interest. For example, when we are only interested in the electronic properties of the system, we assume the ions are too heavy and their motion is slow, so the electrons see them as a static background potential in the Born-Oppenheimer approximation. However, ions' motion can happen and also be induced by the presence of itinerant electrons, making the study of phonons and electron-phonon interactions important. This chapter aims to derive a quantum Hamiltonian that considers strong electron-electron and electron-phonon interactions in a lattice. Starting with the classical description of lattice vibrations, we obtain the quantum Hamiltonian of free phonons, we then second-quantize the electronic part of Eq. 3.1 disregarding the ionic motion, obtaining the celebrated Hubbard, tJ, and Heisenberg models; finally, we show that expanding the electron-ion interaction term up to first order gives rise to a strong electron-phonon interaction, ultimately leading to the famous Holstein model.

3.1 From classical to quantum vibrations

Many physical systems exhibit oscillatory behavior when displaced slightly from equilibrium. Near an energy minimum, the potential energy can be approximated by a quadratic function, leading to a restoring force that is linear in the displacement–which is often a good enough approximation. This phenomenon appears in various contexts, such as a mass on a spring, molecular vibrations, or oscillations in RLC circuits. Figure 3.1 illustrates this idea for a diatomic molecule. Although the actual potential energy (blue curve) may be complex, the parabolic approximation (red curve) accurately describes the restoring force for small deviations from equilibrium, as used in the simple harmonic oscillator model.

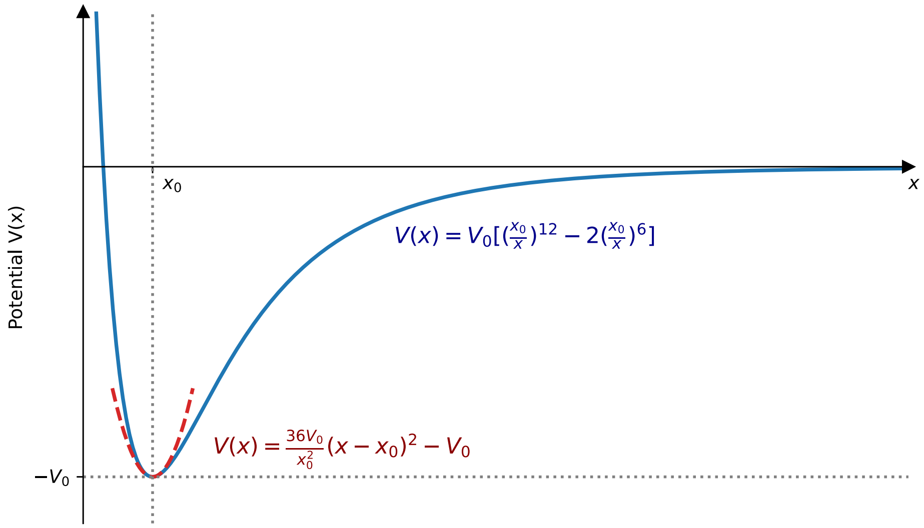

Figure 3.1: Potential energy of a diatomic molecule, described by the Lennard-Jones pair potential, as a function of distance. The blue curve shows the actual potential well, while the red parabola approximates the linear response near the equilibrium position for small oscillations.

This section focuses on how the motion of ions in a crystal lattice can be described as a *collective* harmonic motion. By considering small displacements from equilibrium, the interactions among ions can be modeled as a collection of harmonic oscillators. Upon quantization, these oscillatory modes manifest as phonons—the quanta of vibrational energy in the lattice. The discussion in this section serves as a bridge between the intuitive classical picture of small oscillations and the formal quantized description of vibrational modes [86].

3.1.1 Equilibria and Oscillations

Let us give the formal description of what was described above. First of all, the Lagrangian of a free particle is given by $L = m\dot{q}^2/2$. In the presence of a conservative force, $\mathbf{F} = -\boldsymbol{\nabla} V$, the Lagrangian is written as $L = T - V$, where V is a function of coordinates q only, and T must be quadratic in $\dot{q}$. We want to find the most general Lagrangian that is consistent with the existence of an equilibrium point defined as a point q_{eq} where a particle at rest $\dot{q} = 0$ stays at this point $\ddot{q} = 0$. To find this Lagrangian, we can Taylor expand around the equilibrium point (set $q_{\text{eq}} = 0$ for convenience),

$$L[q, \dot{q}, t] = A + Bq + C\dot{q} + Dq^2 + Eq\dot{q} + F\dot{q}^2 + \text{higher order terms in } q,\ \dot{q}, \text{ and } G(t). \quad (3.2)$$

where A, B, C, D, E, and F are constants, and $G(t)$ is a time-dependent one that may depend of q and $\dot{q}$. From Euler-Lagrange equations, looking for an equilibrium solution such that $q(t) = 0$, $\dot{q} = 0$, and $\ddot{q} = 0$ we obtain

$$L[q, \dot{q}, t] = Dq^2 + F\dot{q}^2 + \text{higher order terms in } q,\ \dot{q}, \quad (3.3)$$

and if we compare with Hooke's Law, we obtain the correspondence $D \to -k/2$ and $F \to m/2$. That way, we derived the Hooke's law and simple harmonic motion with these simple assumptions/constraints. Higher order terms play the role of anharmonicities, which we neglect since we are considering small q. The Euler-Lagrangian equation, in scaled time $t \to \sqrt{|D|/F}t$, reads

$$\frac{\mathrm{d}^2 q}{\mathrm{d}t^2} \pm q = 0, \quad (3.4)$$

with straightforward solutions:

$$\begin{cases} q(t) = \mathrm{Re}(q_0 e^{\pm it}) & \text{for} \quad D < 0 \quad \text{(stable)}, \\ q(t) = \mathrm{Re}(q_0 e^{\pm t}) & \text{for} \quad D > 0 \quad \text{(unstable)}. \end{cases} \quad (3.5)$$

The first equation gives linear oscillations around equilibrium, while the second solution is unstable. It means that the equation of motion that gives stable equilibrium is $\ddot{q} + q = 0$, corresponding to the Lagrangian (in scaled units) $L = (\dot{q}^2 - q^2)/2$.

3.1.2 Normal modes

We found that the Lagrangian that admits oscillations around equilibrium is of the form $L = (\dot{q} + \omega^2 q)/2$. Let us expand this knowledge to an ensemble of particles. For a given system with N degrees of freedom[1], we have a set of generalized coordinates $\{q_i\}$. For a time-independent Lagrangian L, the energy $H = T + V$ is conserved. The stable equilibrium condition is that the potential energy is a minimum, and we set the minimum at $q_i = 0$ for convenience. Expanding the Lagrangian to quadratic order in q_i and $\dot{q}_i$ around equilibrium

---

[1] $N \leq 3M$ Newtonian degrees of freedom, with M the number of particles in three dimensional space.

gives, in matrix notation,

$$T = \frac{1}{2}\dot{\mathbf{q}}^T \cdot \mathbf{T} \cdot \dot{\mathbf{q}} \quad \text{with} \quad T_{ij} = \left.\frac{\partial^2 T}{\partial \dot{q}_i \partial \dot{q}_j}\right|_{\{q_j\}=0,\{\dot{q}_j\}=0}, \tag{3.6}$$

$$V = \frac{1}{2}\mathbf{q}^T \cdot \mathbf{V} \cdot \mathbf{q} \quad \text{with} \quad V_{ij} = \left.\frac{\partial^2 V}{\partial q_i \partial q_j}\right|_{\{q_j\}=0,\{\dot{q}_j\}=0}. \tag{3.7}$$

Both $\mathbf{T}$ and $\mathbf{V}$ are positive-definite[2] symmetric $N \times N$ matrices with T_{ij} and V_{ij} constant matrix elements.

Let us obtain the equations of motion. The Lagrangian is given by $L = \frac{1}{2}\dot{\mathbf{q}}^T \cdot \mathbf{T} \cdot \dot{\mathbf{q}} - \frac{1}{2}\mathbf{q}^T \cdot \mathbf{V} \cdot \mathbf{q}$, so the Euler-Lagrange equations reads

$$\mathbf{T} \cdot \ddot{\mathbf{q}} + \mathbf{V} \cdot \mathbf{q} = 0. \tag{3.8}$$

We look for an oscillatory solution $\mathbf{q}(t) = \mathbf{\Phi} e^{i\omega t}$, where $\mathbf{\Phi}$ is a vector of amplitudes for each coordinate q_i. Plugging it to the Euler-Lagrange equations, we obtain a generalized eigenvalue problem[3],

$$(\mathbf{V} - \omega^2 \mathbf{T}) \cdot \mathbf{\Phi} = 0, \tag{3.9}$$

whose solution is given by $\det(\mathbf{V} - \omega^2\mathbf{T}) = 0$. This term has a N-th order polynomial in ω^2, so there are N solutions ω_α^2, the eigenvalues, which give the *normal mode frequencies*, with corresponding eigenvectors $\mathbf{\Phi}^{(\alpha)}$, the *normal modes*. They have a few interesting properties, namely: ω_α^2 are real and may be degenerate; $\mathbf{\Phi}^{(\alpha)}$ may be chosen real, they form a complete set (the uncoupled basis), they can be chosen orthonormal as ${\mathbf{\Phi}^{(\alpha)}}^T \cdot \mathbf{T} \cdot \mathbf{\Phi}^{(\beta)} = \delta_{\alpha\beta}$, with $\mathbf{T}$ playing the role of the metric; Symmetries lead to no change in V giving a zero frequency mode $\omega_\alpha = 0$.

We can write the general solution in the normal mode basis as

$$\mathbf{q}(t) = \sum_\alpha \rho_\alpha(t) \mathbf{\Phi}^{(\alpha)} \quad \text{or} \quad q_i(t) = \sum_\alpha \rho_\alpha(t) \Phi_i^{(\alpha)}, \tag{3.10}$$

where $\rho_\alpha(t)$ are the normal mode coordinates. We define $R_{i\alpha} = \Phi_i^{(\alpha)}$ and write

$$\mathbf{q}(t) = \mathbf{R} \cdot \boldsymbol{\rho}(t). \tag{3.11}$$

The aforementioned orthogonality condition, written in terms of $\mathbf{R}$ reads

$$\mathbf{R}^T \cdot \mathbf{T} \cdot \mathbf{R} = \mathbb{1}, \tag{3.12}$$

or, equivalently, $\mathbf{R}^T \cdot \mathbf{T} = \mathbf{R}^{-1}$. Using the equations above, we can obtain

$$\boldsymbol{\rho}(t) = \mathbf{R}^T \cdot \mathbf{T} \cdot \mathbf{q}(t) \quad \text{or} \quad q_i(t) = \mathbf{\Phi}_i^{(\alpha)} \cdot \mathbf{T} \cdot \mathbf{q}(t), \tag{3.13}$$

where $\boldsymbol{\rho}(0)$ is given by the initial conditions for $\mathbf{q}$. Interestingly, Eq. 3.12 shows how to diagonalize $\mathbf{T}$. We can use this result to obtain the normal modes and normal mode frequencies. From Eq. 3.9 we can apply the normal mode frequency row vector from the left,

$${\mathbf{\Phi}^{(\alpha)}}^T \cdot \mathbf{V} \cdot \mathbf{\Phi}^{(\beta)} = \omega_\alpha^2 {\mathbf{\Phi}^{(\alpha)}}^T \cdot \mathbf{T} \cdot \mathbf{\Phi}^{(\beta)} = \omega_\beta^2 \delta_{\alpha\beta}, \tag{3.14}$$

---

[2] T must be positive and V is positive due to the equilibrium conditions.

[3] It is called generalized because $\mathbf{T} \neq \mathbb{1}$.

but ${\mathbf{\Phi}^{(\alpha)}}^T\cdot\mathbf{V}\cdot\mathbf{\Phi}^{(\beta)} = (\mathbf{R}^T\cdot\mathbf{V}\cdot\mathbf{R})_{\alpha\beta}$, so that $\mathbf{R}$ diagonalizes both T and V, where $\mathbf{R}^T\cdot\mathbf{V}\cdot\mathbf{R} = \mathbf{\Omega}$ with $\mathbf{\Omega} = \text{diag}(\omega_\alpha^2)$[4]. Thus, we learned that it suffices to diagonalize the matrix $\mathbf{V}$ to obtain the normal modes of the system.

Finally, we want to write both Lagrangian and Hamiltonian of the system in the new coordinates. First, note that

$$T = \frac{1}{2}\dot{\mathbf{q}}^T\cdot\mathbf{T}\cdot\dot{\mathbf{q}} = \frac{1}{2}\dot{\boldsymbol{\rho}}^T\cdot\dot{\boldsymbol{\rho}}, \tag{3.15}$$

$$V = \frac{1}{2}\mathbf{q}^T\cdot\mathbf{V}\cdot\mathbf{q} = \frac{1}{2}\boldsymbol{\rho}^T\cdot\mathbf{\Omega}\cdot\boldsymbol{\rho}, \tag{3.16}$$

so that the Lagrangian is obtained

$$L = \frac{1}{2}\sum_\alpha(\dot{\rho}_\alpha^2 - \omega_\alpha^2\rho_\alpha^2). \tag{3.17}$$

Defining the momentum conjugate to the normal mode coordinates,

$$p_{\rho,\alpha} = \frac{\partial L}{\partial\dot{\rho}_\alpha} = \dot{\rho}_\alpha \tag{3.18}$$

we write the Hamiltonian, $H = \sum p\dot{\rho} - L$, as

$$H = \frac{1}{2}\sum_\alpha(p_{\rho,\alpha}^2 + \omega_\alpha^2\rho_\alpha^2). \tag{3.19}$$

Both 3.17 and 3.19 are the sum of N independent harmonic oscillators.

3.1.3 Phonons

Having established the classical framework for lattice vibrations, we have found that the normal modes of the system correspond to a set of independent harmonic oscillators, each characterized by a well-defined frequency. While this classical approach is sufficient for determining the vibrational spectrum of the crystal, it does not fully capture the behavior of these modes at low temperatures, where thermal energy becomes comparable to or smaller than the quantum scale set by $\hbar\omega$. In this regime, a purely classical treatment fails to explain the observed deviations from the Dulong-Petit law in the heat capacity of solids, as described by the Debye theory. To address these quantum effects, we now transition to a quantum mechanical description, where the vibrational degrees of freedom are quantized, leading to discrete energy levels and the emergence of phonons as the elementary excitations of the lattice. Mathematically, this transition follows naturally by mapping the normal mode coordinates and conjugate momenta to quantum operators that satisfy the fundamental commutation relation $[x, p] = i\hbar$, leading to a second-quantized formulation of lattice vibrations. The procedure is similar to the one given in Chapter 2, where we recall that alternatively

---

[4] Here, the congruence transformation $\mathbf{R}^T\cdot\mathbf{O}\cdot\mathbf{R}$ diagonalizes both T and V. In QM, if $\mathbf{R}$ is a unitary operator, it would mean that T and V commute. However, the equivalence is not true since $\mathbf{R}^T \neq \mathbf{R}$.

we can write H in terms of the Bosonic creation and annihilation operators that satisfy $[a, a^\dagger] = 1$, so that the quantum Hamiltonian for each oscillator is given by

$$H_\alpha = \hbar\omega_\alpha \left(a^\dagger_\alpha a_\alpha + \frac{1}{2} \right). \tag{3.20}$$

An equivalent approach, following Bissbort et. al. [16] is to write the Hamiltonian in the so-called local phonon picture. In our previous derivations, the index α relates to the number of degrees of freedom N, which can be smaller than $3M$. Now, we go back to the $3M$ coordinates and write the harmonic matrix $\mathbf{D}$ as the matrix of second derivatives in V (similar to V_{ij}). This representation is interesting to obtain a good picture of the role of the interactions in the harmonic approximation. We can rewrite the phonon Hamiltonian, in the harmonic approximation, as

$$\begin{aligned} H &= \sum_{n,i} \frac{P^2_{n,i}}{2M_n} + \frac{1}{2} \sum_{n,m,i,j} u_{n,i} D^{ij}_{nm} u_{m,j} && (3.21) \\ &= \sum_{n,i} \frac{P^2_{n,i}}{2M_n} + \frac{1}{2} \sum_{n,m,i,j} u_{n,i} D^{ij}_{nm} u_{m,j} \delta_{nm} \delta_{ij} + \frac{1}{2} \sum_{\substack{n,m,i,j \\ (n,i)\neq(m,j)}} u_{n,i} D^{ij}_{nm} u_{m,j} && (3.22) \\ &= \frac{1}{2} \sum_{n,i} \left(\frac{P^2_{n,i}}{M_n} + D^{ii}_{nn} u^2_{n,i} \right) + \frac{1}{2} \sum_{\substack{n,m,i,j \\ (n,i)\neq(m,j)}} u_{n,i} D^{ij}_{nm} u_{m,j}. && (3.23) \end{aligned}$$

In second quantization, we define

$$\begin{aligned} u_{n,i} &= \sqrt{\frac{1}{2M_n \Omega_{n,i}}} (b_{n,i} + b^\dagger_{n,i}), && (3.24) \\ P_{n,i} &= i \sqrt{\frac{2M_n \Omega_{n,i}}{2}} (b^\dagger_{n,i} - b_{n,i}), && (3.25) \end{aligned}$$

where $D^{ii}_{nn} = M_n \Omega^2_{n,i}$. The first term is a collection of local harmonic oscillators

$$\frac{1}{2} \sum_{n,i} \left(\frac{P^2_{n,i}}{M_n} + M_n \Omega^2_{n,i} u^2_{n,i} \right) = \frac{1}{2} \sum_{n,i} \Omega_{n,i} (b^\dagger_{n,i} b_{n,i} + b_{n,i} b^\dagger_{n,i}). \tag{3.26}$$

The second term represents the interaction part of the Hamiltonian,

$$\frac{1}{2} \sum_{\substack{n,m,i,j \\ (n,i)\neq(m,j)}} u_{n,i} D^{ij}_{nm} u_{m,j} = \frac{1}{2} \sum_{\substack{n,m,i,j \\ (n,i)\neq(m,j)}} \frac{D^{ij}_{nm}}{2M_n \sqrt{\Omega_{n,i} \Omega_{m,j}}} (b_{n,i} b_{m,j} + b_{n,i} b^\dagger_{m,j} + b^\dagger_{n,i} b_{m,j} + b^\dagger_{n,i} b^\dagger_{m,j}). \tag{3.27}$$

The full Hamiltonian can be written in a more convenient way,

$$H = \frac{1}{2}\sum_{n,m,i,j}\Bigg[\delta_{nm}\delta_{ij}\Omega_{n,i}(b^\dagger_{n,i}b_{m,j} + b_{n,i}b^\dagger_{m,j}) \tag{3.28}$$

$$+ \frac{(1-\delta_{nm}\delta_{ij})D^{ij}_{nm}}{2M_n\sqrt{\Omega_{n,i}\Omega_{m,j}}}(b_{n,i}b_{m,j} + b_{n,i}b^\dagger_{m,j} + b^\dagger_{n,i}b_{m,j} + b^\dagger_{n,i}b^\dagger_{m,j})\Bigg] \tag{3.29}$$

$$= \frac{1}{2}\sum_{n,m,i,j}\Bigg[h^{ij}_{nm}(b^\dagger_{n,i}b_{m,j} + b_{n,i}b^\dagger_{m,j}) + g^{ij}_{nm}(b_{n,i}b_{m,j} + b^\dagger_{n,i}b^\dagger_{m,j})\Bigg], \tag{3.30}$$

where

$$g^{ij}_{nm} = \frac{(1-\delta_{nm}\delta_{ij})D^{ij}_{nm}}{2M_n\sqrt{\Omega_{n,i}\Omega_{m,j}}}, \tag{3.31}$$

$$h^{ij}_{nm} = \delta_{nm}\delta_{ij}\Omega_{n,i} + g^{ij}_{nm}. \tag{3.32}$$

Thus the interaction strength is encoded in the matrix g. In the next chapters, we will use the information contained in the matrix g to study the properties of the phononic systems of interest.

3.2 Electrons in a Lattice

In this section, we are interested in obtaining the electronic properties of strongly correlated materials. As discussed in the beginning of this chapter, in this case we can assume that the ions' motion is much slower than the electronic, and employ the Born-Oppenheimer approximation by ignoring the nuclear dynamics in the electronic problem, so the ions' positions are treated as classical fixed parameters. The electrons then feel a fixed background static lattice potential $U_{\text{ion}}(\mathbf{r})$. The Hamiltonian in the second quantized form reads

$$H = \sum_\sigma \int \mathrm{d}^3r\,\Psi^\dagger_\sigma(\mathbf{r})\left[-\frac{1}{2m}\nabla^2 + U_{\text{ion}}(\mathbf{r})\right]\Psi_\sigma(\mathbf{r})$$

$$+ \sum_{\sigma,\sigma'}\int \mathrm{d}^3r\int \mathrm{d}^3r'\,\Psi^\dagger_\sigma(\mathbf{r})\Psi^\dagger_{\sigma'}(\mathbf{r}')V_{ee}(\mathbf{r}-\mathbf{r}')\Psi_{\sigma'}(\mathbf{r}')\Psi_\sigma(\mathbf{r}). \tag{3.33}$$

This general Hamiltonian describes electrons interacting with a static potential, and interacting with each other via Coulomb repulsion V_{ee}. We now employ a series of approximations to reach a more tractable Hamiltonian. First, we assume that the lattice potential is periodic,

$$U_{\text{ion}}(\mathbf{r}+\mathbf{R_i}) = U_{\text{ion}}(\mathbf{r}), \quad \text{with} \quad \mathbf{R_i} = i_1\mathbf{a}_1 + i_2\mathbf{a}_2 + i_3\mathbf{a}_3. \tag{3.34}$$

The Bloch theorem states that the solution of the Schrödinger equation for a periodic potential is given by the Bloch wavefunctions $u_{\mathbf{k},\alpha}(\mathbf{r})$ and energies in electronic bands of the form $\epsilon_{\mathbf{k},\alpha}$. We prefer to work with the Wannier functions, which are equivalent to the Bloch functions, given by the inverse Fourier transform,

$$\phi_{\mathbf{i}\alpha}(\mathbf{r}) = \phi_\alpha(\mathbf{r}-\mathbf{R_i}) = \frac{1}{\sqrt{N}}\sum_{\mathbf{k}} e^{-i\mathbf{k}\cdot\mathbf{R_i}}u_{\mathbf{k},\alpha}(\mathbf{r}). \tag{3.35}$$

We define creation operators for electrons in a Wannier state as

$$c^\dagger_{\mathbf{i}\alpha\sigma} = \int \mathrm{d}^3 r \phi_{\mathbf{i}\alpha}(\mathbf{r})\Psi^\dagger_\sigma(\mathbf{r}) \quad \Rightarrow \quad \Psi^\dagger_\sigma(\mathbf{r}) = \sum_{\mathbf{i}\alpha} \phi^*_{\mathbf{i}\alpha}(\mathbf{r}) c^\dagger_{\mathbf{i}\alpha\sigma}, \tag{3.36}$$

obeying, being Fermions, $\{c_{\mathbf{i}\alpha\sigma}, c^\dagger_{\mathbf{j}\beta\sigma'}\} = \delta_{\mathbf{ij}}\delta_{\alpha\beta}\delta_{\sigma\sigma'}$, $\{c_{\mathbf{i}\alpha\sigma}, c_{\mathbf{j}\beta\sigma'}\} = \{c^\dagger_{\mathbf{i}\alpha\sigma}, c^\dagger_{\mathbf{j}\beta\sigma'}\} = 0$. In the Wannier basis, the Hamiltonian becomes:

$$H = \sum_{\mathbf{ij}\alpha\sigma} t^\alpha_{\mathbf{ij}} c^\dagger_{\mathbf{i}\alpha\sigma} c_{\mathbf{j}\alpha\sigma} + \sum_{\mathbf{ijmn}} \sum_{\alpha\beta\mu\nu} v^{\alpha\beta\mu\nu}_{\mathbf{ijmn}} c^\dagger_{\mathbf{i}\alpha\sigma} c^\dagger_{\mathbf{j}\beta\sigma'} c_{\mathbf{n}\nu\sigma'} c_{\mathbf{m}\mu\sigma}, \tag{3.37}$$

with

$$t^\alpha_{\mathbf{ij}} = \int \mathrm{d}^3 r \phi^*_{\mathbf{i}\alpha}(\mathbf{r}) \left[-\frac{1}{2m}\nabla^2 + U_{\text{ion}}(\mathbf{r}) \right] \phi_{\mathbf{j}\alpha}(\mathbf{r}) \tag{3.38}$$

and

$$v^{\alpha\beta\mu\nu}_{\mathbf{ijmn}} = \int \mathrm{d}^3 r \int \mathrm{d}^3 r' \phi^*_{\mathbf{i}\alpha}(\mathbf{r}) \phi^*_{\mathbf{j}\beta}(\mathbf{r}') V_{ee}(\mathbf{r} - \mathbf{r}') \phi_{\mathbf{m}\mu}(\mathbf{r}) \phi_{\mathbf{n}\nu}(\mathbf{r}'). \tag{3.39}$$

This is a general Hamiltonian for electrons in a lattice. In the following, we make some assumptions to obtain the Hubbard model.

3.2.1 Hubbard Model

Let us simplify the Hamiltonian by making some extra assumptions: 1- all bands, but the lowest, have very high energies, and thus are electronically unavailable – in this case we drop the band index and work only with the lowest band; 2- the lower band is a s-band, so it has rotational symmetry – so that the hopping elements depends only on the distance between sites **i** and **j**. Therefore, we assume that the matrix elements of both t and v decrease fast with $|\mathbf{R_i} - \mathbf{R_j}|$, so we can restrict to nearest-neighbor sites only, arriving at the *generalized* Hubbard model

$$\begin{aligned} H = {} & -t \sum_{\langle \mathbf{i},\mathbf{j} \rangle} \sum_\sigma (c^\dagger_{\mathbf{i}\sigma} c_{\mathbf{j}\sigma} + c^\dagger_{\mathbf{j}\sigma} c_{\mathbf{i}\sigma}) + U \sum_{\mathbf{i}} n_{\mathbf{i}\uparrow} n_{\mathbf{i}\downarrow} + V \sum_{\langle \mathbf{i},\mathbf{j} \rangle} n_{\mathbf{i}} n_{\mathbf{j}} \\ & + X \sum_{\langle \mathbf{i},\mathbf{j} \rangle} \sum_\sigma (c^\dagger_{\mathbf{i}\sigma} c_{\mathbf{j}\sigma} + c^\dagger_{\mathbf{j}\sigma} c_{\mathbf{i}\sigma})(n_{\mathbf{i}-\sigma} + n_{\mathbf{j}-\sigma}) + J \sum_{\langle \mathbf{i},\mathbf{j} \rangle} \mathbf{S_i} \cdot \mathbf{S_j} \\ & + Y \sum_{\langle \mathbf{i},\mathbf{j} \rangle} (c^\dagger_{\mathbf{i}\uparrow} c^\dagger_{\mathbf{i}\downarrow} c_{\mathbf{j}\downarrow} c_{\mathbf{j}\uparrow} + c^\dagger_{\mathbf{j}\downarrow} c^\dagger_{\mathbf{j}\uparrow} c_{\mathbf{i}\uparrow} c_{\mathbf{i}\downarrow}), \end{aligned} \tag{3.40}$$

where $n_{\mathbf{i}\sigma} = c^\dagger_{\mathbf{i}\sigma} c_{\mathbf{i}\sigma}$, $n_{\mathbf{i}} = n_{\mathbf{i}\uparrow} + n_{\mathbf{i}\downarrow}$, $\mathbf{S_i} = \frac{1}{2}\sum_{\sigma\sigma'} c_{\mathbf{i}\sigma} \boldsymbol{\sigma}_{\sigma\sigma'} c_{\mathbf{i}\sigma'}$, and

$t = -t_{\mathbf{ij}}$ the hopping between neighboring sites,
$U = v_{\mathbf{iiii}}$ the on-site Hubbard repulsion,
$V = v_{\mathbf{ijij}}$ the Coulomb repulsion between between neighboring sites,
$X = v_{\mathbf{iiij}}$ the bond-charge interaction,
$J = -2v_{\mathbf{ijji}}$ the Heisenberg exchange interaction between neighboring sites,
$Y = v_{\mathbf{iijj}}$ the hopping between pairs of electrons.

The symmetries of the Hamiltonian are in $\mathcal{N} = \sum_{\mathbf{i}} n_{\mathbf{i}}$ number of electrons, $\mathcal{M} = \mathcal{N}_\uparrow - \mathcal{N}_\downarrow$ magnetization, and total spin $\mathbf{S} = \sum_{\mathbf{i}} \mathbf{S}_{\mathbf{i}}$. Hubbard [66] noticed, for some transition metals, that one can neglect all terms apart from t and U, leaving the well-known Hubbard model

$$H_{\text{Hubbard}} = -t \sum_{\langle \mathbf{i},\mathbf{j} \rangle \sigma} (c^\dagger_{\mathbf{i}\sigma} c_{\mathbf{j}\sigma} + \text{H.c.}) + U \sum_{\mathbf{i}} n_{\mathbf{i}\uparrow} n_{\mathbf{i}\downarrow}. \tag{3.41}$$

3.2.2 t–J and Heisenberg Models

Schrieffer–Wolff transformation

In quantum mechanics, the Schrieffer–Wolff (SW) transformation is used to obtain an effective Hamiltonian that describes the low energy physics of the system. Consider the Hamiltonian,

$$H = H_0 + V. \tag{3.42}$$

The unitary transformation can be written as $H' = e^S H e^{-S}$, so that $S^\dagger = -S$. If H is Hermitian, so is H'. They share the same eigenvalues and $|\psi\rangle \to e^S |\psi\rangle$ does not change the expectation values. We can expand H' via BCH formula,

$$\begin{aligned} H' &= H + [S, H] + \frac{1}{2}[S, [S, H]] + \cdots \\ &= H_0 + V + [S, H_0] + [S, V] + \frac{1}{2}[S, [S, H_0]] + \frac{1}{2}[S, [S, V]] + \cdots . \end{aligned} \tag{3.43}$$

The idea is to make the Hamiltonian diagonal to first order in V. We choose the generator S such that $V + [S, H_0] = 0$. It also implies that $\frac{1}{2}[S, [S, H_0]] = -\frac{1}{2}[S, V]$, so

$$H' = H_0 + \frac{1}{2}[S, V] + \mathcal{O}(V^3). \tag{3.44}$$

This is the standard form of the SW transformed Hamiltonian. Neglecting $\mathcal{O}(V^3)$, it describes the low energy physics.

The Hubbard model describes the behavior of conduction band electrons and itinerant magnetism for arbitrary filling. The large Hilbert space is still tractable numerically for small enough system sizes. We now turn to the problem where we want to describe strongly interacting localized spins on a lattice. That is, at half-filling, when the ground state is described by one electron per site we can obtain the Heisenberg model. Additionally, there is an intermediate model between these two, the t-J model, that is related to the low energy physics of the Hubbard model. The Schrieffer–Wolff transformation can be used to extract the low-energy physics of strongly interacting systems if the energy scales is chosen such that the higher energy states are unavailable in a given subset. Let us work in the case of near half-filling $N_e/N < 1$ to understand the role of the transformation in this system. For example, considering two sites, we can have $N_e = 0, 1, 2, 3, 4$ electrons, so that there are 16 possible states. Schematically, half of the processes are shown in Fig. 3.2 (the other half are their spin flipped counterparts). In (a) and (b) the number of doubly occupied sites remain unchanged, while in (c) and (d) it increases or decreases the number of doubly occupied sites.

Thus, only processes (c) and (d) contribute to the on-site energy U. This is the information that we need for the SW transformation: the hopping Hamiltonian can be split into two parts $H_t = H_t^{(0)} + H_t^{(\pm)}$, with $H_t^{(\pm)} = H_{t,d+} + H_{t,d-}$ where $H_{t,d\pm}$ increases (decreases) the number of doubly occupied sites, and $H_t^{(0)}$ is the hopping to empty sites.

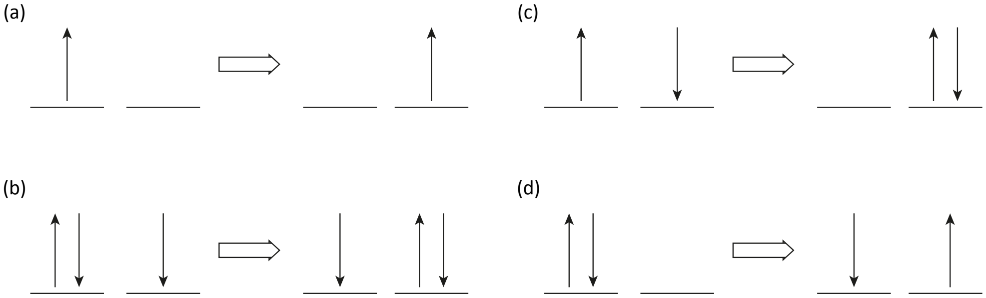

Figure 3.2: Schematic representation of the possible states of a two-site system.

The goal is to eliminate the high-energy contributions $H_t^{(\pm)}$ from the Hubbard Hamiltonian to obtain an effective low energy description, as

$$H' = e^S (H_t^{(0)} + H_t^{(\pm)} + H_U) e^{-S} = H_t^{(0)} + H_U + \mathcal{O}(t^2/U). \tag{3.45}$$

We have to find the generator S, to obtain the terms of the order $\mathcal{O}(t^2/U)$. Following the usual procedure, we write

$$\begin{aligned} H' &= H + [S, H] + \frac{1}{2}[S, [S, H]] + \cdots && (3.46)\\ &= H_U + H_t^{(0)} + H_t^{(\pm)} + [S, H_U] + [S, H_t^{(0)}] + [S, H_t^{(\pm)}] && (3.47)\\ &+ \frac{1}{2}[S, [S, H_U]] + \frac{1}{2}[S, [S, H_t^{(0)}]] + \frac{1}{2}[S, [S, H_t^{(\pm)}]] + \cdots . && (3.48) \end{aligned}$$

We want to find S such that $H_t^{(\pm)} + [S, H_U] = 0$ so, to lowest order, the operator does not change the number of doubly occupied sites. We note that $[H_{t,d\pm}, H_U] = \mp U H_{t,d\pm}$, so $S = (H_{t,d+} - H_{t,d-})/U$, which greatly simplifies H',

$$H' = H_U + H_t^{(0)} - \frac{1}{2}[S, [S, H_U]] + [S, H_t^{(0)}] + \frac{1}{2}[S, [S, H_t^{(0)}]] + \frac{1}{2}[S, [S, H_t^{(\pm)}]] + \cdots . \tag{3.49}$$

We now want to remove higher order terms and any high energy term remaining. Let us check the order of magnitude of the remaining terms. First, we observe that $[S, H_t^{(0)}] = \mathcal{O}(t^2/U)$, and thus $[S, [S, H_t^{(0)}]] = \mathcal{O}(t^3/U^2)$ is neglected. Secondly, $[S, [S, H_t^{(\pm)}]] = -[S, [S, [S, H_U]]] = \mathcal{O}(t^3/U^2)$ is also neglected. Lastly, the term $[S, H_t^{(0)}]$ involves changing the number of doubly occupied sites, but can be easily removed via a second-order correction $S \to S + S^{(2)}$. The term $-\frac{1}{2}[S, [S, H_U]]$ is obtained via $[S, H_{t,d\pm}] = [H_{t,d+}, H_{t,d-}]/U$. The effective low energy Hamiltonian becomes

$$H' = H_U + H_t^{(0)} + \frac{1}{U}[H_{t,d+}, H_{t,d-}]. \tag{3.50}$$

In the last term, the product $H_{t,d+}H_{t,d-}$ does not contribute, as we are interested in the low energy regime near half-filling. That way, for the same reason, H_U is also neglected. We are left with a term that creates and destroys one doubly occupied site $H_{t,d-}H_{t,d+}$. Finally, after some algebra, we obtain the t-J Hamiltonian

$$H_{tJ} = -t \sum_{\langle \mathbf{i},\mathbf{j}\rangle\sigma} (c^{\dagger}_{\mathbf{i}\sigma} c_{\mathbf{j}\sigma} + \text{H.c.}) + \frac{4t^2}{U} \sum_{\langle \mathbf{i},\mathbf{j}\rangle} \left(\mathbf{S}_{\mathbf{i}} \cdot \mathbf{S}_{\mathbf{j}} - \frac{1}{4} n_{\mathbf{i}} n_{\mathbf{j}} \right), \tag{3.51}$$

where the first term comes from $H_t^{(0)}$. The possibility to doubly occupy a site is excluded, so the hopping term corresponds to hopping of empty sites, as we are working in a reduced Hilbert space now[5]. Hubbard and t-J models agree in the $U \gg t$ limit, as the strong on-site repulsion forbids (strongly penalizes) double occupancy.

At half-filling, $N_e/N = 1$, the system's ground state is characterized by exactly one electron per site, such that the hopping does not contribute in the t-J model. We are left with a pure antiferromagnetic ($J > 0$) Heisenberg Hamiltonian,

$$H_{\text{Heisenberg}} = J \sum_{\langle \mathbf{i},\mathbf{j}\rangle} \mathbf{S}_{\mathbf{i}} \cdot \mathbf{S}_{\mathbf{j}}. \tag{3.52}$$

A more detailed discussion of the derivations can be found in the book by Eckle [37].

3.3 Electron-phonon interactions

In the last part of this chapter, we aim to obtain the electron-phonon interactions. We start from the Hamiltonian 3.1 and study the electron-ion term, which can be written as

$$H_{\text{el-ion}} = \sum_{n,m=1}^{N_c} \sum_{\alpha=1}^{N_b} V_{\text{el-ion}}(\mathbf{r}_n - \mathbf{R}_{m\alpha}), \tag{3.53}$$

where N_c is the number of cells and N_b the number of basis atoms in the unit cell, with $\mathbf{R}_{n\alpha}(t) = \mathbf{R}_n + \boldsymbol{\rho}_\alpha + \mathbf{u}_{n\alpha}(t) = \mathbf{R}^0_{n\alpha} + \mathbf{u}_{n\alpha}(t)$. This can be expanded in power series in ion displacements u, providing

$$\begin{aligned} H_{\text{el-ion}} &= \sum_{n} \sum_{m,\alpha} V_{\text{el-ion}}(\mathbf{r} - \mathbf{R}^0_{m\alpha} - \mathbf{u}_{m\alpha}) \\ &\approx \sum_{n} \sum_{m,\alpha} V_{\text{el-ion}}(\mathbf{r}_n - \mathbf{R}^0_{m\alpha}) - \sum_{n} \sum_{m,\alpha} \mathbf{u}_{m\alpha} \cdot \boldsymbol{\nabla}_{\mathbf{R}_{m\alpha}} V_{\text{el-ion}}(\mathbf{r}_n - \mathbf{R}_{m\alpha}) \Big|_{\mathbf{R}^0_{m\alpha}} \\ &\equiv H^{(0)}_{\text{el-ion}} + H^{(1)}_{\text{el-ion}}, \end{aligned} \tag{3.54}$$

where we neglected higher order terms, $\mathcal{O}(u^2)$. The constant term $H^{(0)}_{\text{el-ion}}$ is incorporated in the periodic potential for the electrons, while the electron-phonon interaction is encoded

---

[5] Alternatively, one can explicitly write the hopping term in a way that only hopping of empty sites can happen: $c^{\dagger}_{i\sigma} \to c^{\dagger}_{i\sigma}(1 - n_{i\sigma})$.

in the first order term. The gradient can be straightforwardly evaluated writing $V_{\text{el-ion}}$ in reciprocal space

$$V_{\text{el-ion}}(\mathbf{r}-\mathbf{R}_{n\alpha}) = \frac{1}{V}\sum_{\mathbf{Q}} e^{i\mathbf{Q}\cdot(\mathbf{r}-\mathbf{R}_{n\alpha})}V_{\mathbf{Q}}, \tag{3.55}$$

$$\boldsymbol{\nabla}_{\mathbf{R}_{m\alpha}} V_{\text{el-ion}}(\mathbf{r}_n-\mathbf{R}_{m\alpha})\Big|_{\mathbf{R}^0_{m\alpha}} = \frac{-i}{V}\sum_{\mathbf{Q}} \mathbf{Q}e^{i\mathbf{Q}\cdot(\mathbf{r}-\mathbf{R}^0_{n\alpha})}V_{\mathbf{Q}}. \tag{3.56}$$

Thus, we can write the second quantized electron-phonon Hamiltonian as

$$\mathcal{H}_{\text{el-ph}} = \sum_{b,k,\sigma}\sum_{b',k',\sigma'} \langle b,k,\sigma|\, H^{(1)}_{\text{el-ion}}\, |b',k',\sigma'\rangle\, c^{\dagger}_{b,k,\sigma}c_{b',k',\sigma'}, \tag{3.57}$$

where

$$\begin{aligned}\langle b,k,\sigma|\, H^{(1)}_{\text{el-ion}}\, |b',k',\sigma'\rangle &= -\int d\mathbf{r}\Psi^*_{b,k,\sigma}(\mathbf{r})\sum_{n,\alpha}\mathbf{u}_{n\alpha}\cdot\boldsymbol{\nabla}_{\mathbf{R}_{n\alpha}}V_{\text{el-ion}}(\mathbf{r}-\mathbf{R}_{n\alpha})\Big|_{\mathbf{R}^0_{n\alpha}}\Psi_{b',k',\sigma'}(\mathbf{r})\\ &= \frac{i}{V}\sum_{n,\alpha,\mathbf{Q}}\mathbf{Q}\cdot\mathbf{u}_{n\alpha}e^{-i\mathbf{Q}\cdot\mathbf{R}^0_{n\alpha}}V_{\mathbf{Q}}\int d\mathbf{r}\Psi^*_{b,k,\sigma}(\mathbf{r})e^{i\mathbf{Q}\cdot\mathbf{r}}\Psi_{b',k',\sigma'}(\mathbf{r}),\end{aligned} \tag{3.58}$$

where the displacement operator is written as

$$\mathbf{u}_{n\alpha} = \sum_{\mathbf{q}}\sum_{j=1}^{3N_b}\sqrt{\frac{\hbar}{2M_\alpha\omega_j(\mathbf{q})}}\boldsymbol{\xi}^{(j)}_\alpha(\mathbf{q})(b_{j,\mathbf{q}}+b^{\dagger}_{j,-\mathbf{q}})\frac{e^{i\mathbf{q}\cdot\mathbf{R}_n}}{\sqrt{N}}. \tag{3.59}$$

Note that $e^{-i\mathbf{Q}\cdot\mathbf{R}^0_{n\alpha}} = e^{-i\mathbf{Q}\cdot\mathbf{R}_n}e^{-i\mathbf{Q}\cdot\boldsymbol{\rho}_\alpha}$, and in Eq. 3.58 will appear $\sum_n e^{i(\mathbf{q}-\mathbf{Q})\cdot\mathbf{R}_n} = N\delta_{\mathbf{q},\mathbf{Q}}$. The electron-phonon Hamiltonian reads

$$\begin{aligned}\mathcal{H}_{\text{el-ph}} &= \frac{i}{\sqrt{N}}\sum_{\mathbf{q},j,\alpha}\sum_{b,k,\sigma}\sum_{b',k',\sigma'}\sqrt{\frac{\hbar}{2M_\alpha\omega_j(\mathbf{q})}}\mathbf{q}\cdot\boldsymbol{\xi}^{(j)}_\alpha(\mathbf{q})e^{-i\mathbf{q}\cdot\boldsymbol{\rho}_\alpha}V_{\mathbf{q}}\alpha_{q,b,k,\sigma,b',k',\sigma'}(b_{j,\mathbf{q}}+b^{\dagger}_{j,-\mathbf{q}})c^{\dagger}_{b,k,\sigma}c_{b',k',\sigma'}\\ &= \sum_{\mathbf{q},j}\sum_{b,k,\sigma}\sum_{b',k',\sigma'}\frac{1}{\sqrt{N}}M_{q,j,b,k,\sigma,b',k',\sigma'}(b_{j,\mathbf{q}}+b^{\dagger}_{j,-\mathbf{q}})c^{\dagger}_{b,k,\sigma}c_{b',k',\sigma'},\end{aligned} \tag{3.60}$$

where we defined the overlap integral

$$\alpha_{q,b,k,\sigma,b',k',\sigma'} = \frac{1}{\Omega}\int d\mathbf{r}\Psi^*_{b,k,\sigma}(\mathbf{r})e^{i\mathbf{q}\cdot\mathbf{r}}\Psi_{b',k',\sigma'}(\mathbf{r}), \tag{3.61}$$

and the coupling strength

$$M_{q,j,b,k,\sigma,b',k',\sigma'} = \frac{i}{\Omega}\sum_{\alpha}\sqrt{\frac{\hbar}{2M_\alpha\omega_j(\mathbf{q})}}\mathbf{q}\cdot\boldsymbol{\xi}^{(j)}_\alpha(\mathbf{q})e^{-i\mathbf{q}\cdot\boldsymbol{\rho}_\alpha}V_{\mathbf{q}}\alpha_{q,b,k,\sigma,b',k',\sigma'}, \tag{3.62}$$

with $\Omega = V/N$. The imaginary unit is removed via a global phase transformation. This is the most general Hamiltonian that considers electron-phonon interactions. In the following, we make a series of approximations and assumptions to obtain the celebrated Holstein model, the most basic and paradigmatic model for electron-phonon interactions.

3.3.1 Holstein model

Let us evaluate the overlap integral above in terms of the Wannier functions whitin some approximations. First, consider $H^{(1)}_{\text{el-ion}}$ is independent of spin, implying $\sigma = \sigma'$, and then the overlap integral is also independent of the spin. In terms of the Wannier functions, we evaluate α as

$$\begin{aligned}\Omega\alpha_{q,b,k,b',k'} &= \int d\mathbf{r}\Psi^*_{b,k}(\mathbf{r})e^{i\mathbf{q}\cdot\mathbf{r}}\Psi_{b',k'}(\mathbf{r}) \\ &= \frac{1}{N}\sum_{\mathbf{R}\mathbf{R}'} e^{-i\mathbf{k}\cdot\mathbf{R}}e^{i\mathbf{k}'\cdot\mathbf{R}'}\int d\mathbf{r}e^{i\mathbf{q}\cdot\mathbf{r}}\phi^*_b(\mathbf{r}-\mathbf{R})\phi_{b'}(\mathbf{r}-\mathbf{R}'). \end{aligned} \tag{3.63}$$

Within the tight-binding approximation, the overlap between distinct sites is extremely small, and terms like $\mathbf{R} \neq \mathbf{R}'$ are vanishing

$$\Omega\alpha_{q,b,k,b',k'} = \frac{1}{N}\sum_{\mathbf{R}} e^{i(\mathbf{k}'-\mathbf{k})\cdot\mathbf{R}}\int d\mathbf{r}e^{i\mathbf{q}\cdot\mathbf{r}}\phi^*_b(\mathbf{r}-\mathbf{R})\phi_{b'}(\mathbf{r}-\mathbf{R}). \tag{3.64}$$

As we have done in the Hubbard model, we consider the case where all bands, but the lowest, are very high in energy, so that they are unavailable. We fix to the lower Bloch band and drop the band indices,

$$\begin{aligned}\Omega\alpha_{q,k,k'} &= \frac{1}{N}\sum_{\mathbf{R}} e^{i(\mathbf{k}'-\mathbf{k})\cdot\mathbf{R}}\int d\mathbf{r}e^{i\mathbf{q}\cdot\mathbf{r}}|\phi(\mathbf{r}-\mathbf{R})|^2 \\ &= \frac{1}{N}\sum_{\mathbf{R}} e^{i(\mathbf{k}'-\mathbf{k})\cdot\mathbf{R}}e^{i\mathbf{q}\cdot\mathbf{R}}\int d\mathbf{r}e^{i\mathbf{q}\cdot\mathbf{r}}|\phi(\mathbf{r})|^2, \end{aligned} \tag{3.65}$$

but $\frac{1}{N}\sum_{\mathbf{R}} e^{i(\mathbf{q}+\mathbf{k}'-\mathbf{k})\cdot\mathbf{R}} = \delta_{\mathbf{q}+\mathbf{k}',\mathbf{k}}$ and define $\rho_0 = \int d\mathbf{r}e^{i\mathbf{q}\cdot\mathbf{r}}|\phi(\mathbf{r})|^2$. We also consider that the all eigenmode frequencies of the phonon Hamiltonian ω_j, but the lowest, lie in a very high energy band, so that they are effectively frozen out at the energy scales of interest. We thus fix eigenmode to the lowest and drop the index. In the Einstein approximation, the dispersion relation $\omega(\mathbf{q})$ is disregarded, which is a valid assumption when the dispersion is weak. Additionally, the remaining factors (the polarization vectors, phase factors, and potentials) vary weakly with $\mathbf{q}$, so $M_{\mathbf{q}} \approx M_0$. Having the momentum space dependence only on the operators, we can Fourier transform the Hamiltonian back to real space, obtaining the Holstein model

$$H_{\text{Holstein}} = g\sum_{i\sigma}(b^\dagger_i + b_i)c^\dagger_{i\sigma}c_{i\sigma}, \tag{3.66}$$

where g contains M_0 and normalization factors. This is the most basic model describing electron-phonon systems, where an electron at a site i interacts with a local phonon at the same site. We observe that many assumptions and approximations made here were also taken into account to obtain the Hubbard model. This shows that both models are compatible in a sense that they describe the system in similar energy scales. The combination of these models is called the Hubbard-Holstein model, which is central to our study on strongly interacting electron-phonon systems.

4

Gaussian and non-Gaussian states

Gaussian and non-Gaussian states are both central to understanding quantum many-body systems, each contributing distinct insights into the underlying physics. Gaussian states, due to their simplicity and broad applicability, provide a natural starting point for analyzing systems governed by quadratic Hamiltonians and are essential for clarifying quantum correlations and entanglement in bosonic systems. Although non-Gaussian states occupy a relatively niche area, they are vital to our approach, as they introduce critical features necessary for capturing complex quantum phenomena that extend beyond the Gaussian framework. In this chapter, we begin by outlining the fundamental properties of quadratic Hamiltonians and presenting the tools for constructing and analyzing Gaussian states. We then examine the transformations that connect Gaussian and non-Gaussian states, highlighting their importance in describing the ground states of interacting systems. By the chapter's end, readers will have developed a robust foundation in both types of states, setting the stage for the advanced methods and applications discussed in later chapters.

4.1 Quadratic Hamiltonians

The use of quadratic Hamiltonians to model quantum dynamics is widespread, particularly when higher-order terms are insignificant or negligible, which is frequently true for quantum light fields. Moreover, quadratic Hamiltonians provide a reliable approximation in various experimental scenarios of significant interest, including ion traps, optomechanical systems, and several other systems. The quantum harmonic oscillator is a classical example in quantum mechanics, and the second quantized description of light reveals that photons behave as quantum harmonic oscillators.

A quadratic Hamiltonian is defined as a Hamiltonian with polynomial of order two in the canonical operators, x and p. In general, this class of Hamiltonians can be written as

$$H = \frac{1}{2}(Ax^2 + Bp^2 + C(xp + px)) + Dx + Ep \tag{4.1}$$

the terms x^2, p^2, xp, and px represent quadratic operators in phase space. In quantum optics, x and p are seen as continuous non-commuting variables. The position and momentum of a photon are not well defined, and x and p may represent multiple positions and momenta in systems with multiple degrees of freedom. Therefore, x and p are usually referred as *quadrature operators*.

4.1.1 Quadrature parametrization

The quadrature parametrization is done by defining the quadrature notation $R = (x, p)^T$. Let us obtain the canonical commutation relations (CCR) in terms of the quadrature vector,

$$[R, R^T] = \begin{pmatrix} [x,x] & [x,p] \\ [p,x] & [p,p] \end{pmatrix} = \begin{pmatrix} 0 & i \\ -i & 0 \end{pmatrix} = i\Omega, \tag{4.2}$$

with $\Omega = \begin{pmatrix} 0 & 1 \\ -1 & 0 \end{pmatrix}$. Note that Ω is anti-symmetric $\Omega^T = -\Omega$ and $\Omega^2 = -\mathbb{1}$, so it is also a real orthogonal transformation, $\Omega^T\Omega = \mathbb{1}$.

Generally, we have a finite set of canonical degrees of freedom represented by pairs of self-adjoint canonical operators x_n and p_n that obeys $[x_n, p_m] = i\delta_{nm}$ ($\hbar = 1$). In quantum optics, the canonical degrees of freedom are called *modes*, and we will borrow this terminology from now on. The question that may arises comes from the way we define the quadrature vector in multimode systems. Let us construct $R' = (x_1, p_1, \ldots, x_n, p_n)^T = (R_1, \ldots, R_n)$, so the CCR is given by

$$[R', R'^T] = i\bigoplus_{n=0}^{n}\Omega = i\tilde{\Omega}. \tag{4.3}$$

Equivalently, we can re-order the canonical operators as $R = (x_1, x_2, \ldots, x_n, p_1, p_2, \ldots, p_n)^T \equiv (x, p)^T$, with $x = (x_1, x_2, \ldots, x_n)^T$ and $p = (p_1, p_2, \ldots, p_n)^T$, that yields

$$[R, R^T] = i\sigma, \tag{4.4}$$

with

$$\sigma = \begin{pmatrix} 0_n & \mathbb{1}_n \\ -\mathbb{1}_n & 0_n \end{pmatrix}, \tag{4.5}$$

where $\mathbb{1}_n$ and 0_n are, respectively, the $n \times n$ identity and null matrices. As Ω and $\tilde{\Omega}$, σ is an anti-symmetric, real orthogonal matrix, and $\sigma^2 = \mathbb{1}_n$. In this study, we adopt the ordering convention $R = (x_1, x_2, \ldots, x_n, p_1, p_2, \ldots, p_n)^T$. Finally, in terms of R, a general quadratic Hamiltonian can be written as

$$H = R^T h R + R^T \alpha, \tag{4.6}$$

where h is a positive-definite symmetric real matrix and α is a vector of real numbers.

4.1.2 The Symplectic Group

The linear term in the quadratic Hamiltonian [conf. Eq. 4.6] can be absorbed in the first term by a simple change of variables. Let us then consider the Heisenberg evolution of the quadratic Hamiltonian $H = R^T h R$,

$$\begin{aligned}\dot{R} = i[H,R] &= \frac{i}{2}[R^T h R, R] \\ &= \frac{i}{2}\begin{pmatrix}[x^T h_{xx} x + x^T h_{xp} p + p^T h_{xp}^T x + p^T h_{pp} p, x] \\ [x^T h_{xx} x + x^T h_{xp} p + p^T h_{xp}^T x + p^T h_{pp} p, p]\end{pmatrix} \\ &= \begin{pmatrix} h_{xp} x + h_{pp} p \\ -h_{xx} x - h_{xp} p\end{pmatrix} = \sigma h R, \end{aligned} \tag{4.7}$$

where h_{xx}, h_{pp}, h_{xp} are $n \times n$ symmetric blocks of the symmetric matrix h, $x = (x_1, x_2, \ldots, x_n)^T$, and $p = (p_1, p_2, \ldots, p_n)^T$. The solution is straightforward, given by $R(t) = e^{\sigma h t} R(0)$. The transformation $e^{\sigma h t}$ must preserve the CCR given that the result represents the action of a unitary operation. This can be rephrased by stating that $e^{\sigma h t}$ is part of the group of linear canonical transformations, a concept well-established in classical Hamiltonian mechanics. This group is commonly referred to as the real symplectic group in $2n$-dimensional space, denoted by $\mathrm{Sp}(2n, \mathbb{R})$. A matrix S is in the symplectic group if it satisfies

$$S^T \sigma S = \sigma, \tag{4.8}$$

where the so defined σ is the symplectic matrix which encodes the CCR in the quadrature notation formalism. This condition means that S preserves the "symplectic form" of phase space, that is, preserves the CCR, ensuring that the geometry of the Hamiltonian flows remains consistent under transformation. Additionally, the operators x^2, p^2, and $(xp + px)$ relate to the symplectic group $\mathrm{Sp}(2n, \mathbb{R})$, which is the group of transformations that preserve the symplectic structure. In phase space, the symplectic structure is preserved by transformations that keep the fundamental commutation relations intact i.e., $[x, p] = i$ in quantum mechanics or the Poisson bracket $\{x, p\} = 1$ in classical mechanics.

In general, the symplectic group $\mathrm{Sp}(2n, \mathbb{R})$ is defined as the group of $2n \times 2n$ matrices that preserve the symplectic form in a $2n$–dimensional phase space. Here, n would correspond to the number of degrees of freedom or particle pairs in the system. For a one-dimensional phase space (i.e., one degree of freedom), $\mathrm{Sp}(2, \mathbb{R})$ applies, while for a system with two degrees of freedom (e.g., two particles), the appropriate group would be $\mathrm{Sp}(4, \mathbb{R})$.

4.1.3 Diagonalizing Quadratic Hamiltonians

The relationship between quadratic Hamiltonians and symplectic algebra comes from the structure of quadratic forms in classical and quantum mechanics. This quadratic form can often be simplified using symplectic transformations, which preserve the canonical structure of the phase space. Symplectic transformations can rotate and scale the coordinates x and p in phase space, which allows us to find a new coordinate system where the Hamiltonian is diagonal. This is particularly useful in systems like oscillators, where diagonalization corresponds to finding the normal modes. The symplectic transformation that removes the cross-term in a quadratic Hamiltonian is essentially a rotation in phase space, often represented by a *squeeze transformation* or a *canonical transformation.* This transformation changes the phase-space coordinates $R = (x, p)$ to new coordinates $\tilde{R} = (\tilde{x}, \tilde{p})$ where the Hamiltonian takes a diagonal form without cross-terms.

For example, for a single-mode quadratic Hamiltonian of the form $H = R^T hR$, we can apply a symplectic transformation that rescales and rotates R by a matrix in $\mathrm{Sp}(2, \mathbb{R})$ to remove terms like $(xp + px)$. One specific transformation is

$$\begin{pmatrix} \tilde{x} \\ \tilde{p} \end{pmatrix} = \begin{pmatrix} \cosh\theta & \sinh\theta \\ \sinh\theta & \cosh\theta \end{pmatrix} \begin{pmatrix} x \\ p \end{pmatrix}, \tag{4.9}$$

where the parameter θ (often related to the "squeeze" factor) is chosen based on the coefficients in the original Hamiltonian. The right value of θ will turn the Hamiltonian into a simpler form like

$$H = \frac{1}{2}(\tilde{x}^2 + \tilde{p}^2) = \frac{1}{2}\tilde{R}^T\tilde{R}, \tag{4.10}$$

where $\tilde{x}$ and $\tilde{p}$ are transformed variables. This diagonalization is equivalent to finding the eigenvalues and eigenvectors of the Hamiltonian matrix and allows the Hamiltonian to describe independent harmonic oscillators.

This transformation preserves the symplectic structure of the phase space, meaning that it retains the fundamental commutation or Poisson relations between $\tilde{x}$ and $\tilde{p}$. By selecting the appropriate parameters for the transformation, the Hamiltonian is diagonalized, which simplifies the analysis of the system's dynamics. Thus, the operators x^2, p^2, and $(xp + px)$ indeed relate to symplectic groups in that they generate transformations in phase space that preserve its symplectic structure. These transformations are crucial for simplifying and diagonalizing quadratic Hamiltonians by symplectic methods, making the system's dynamics easier to analyze. These symplectic transformations are widely used in fields like quantum optics and classical mechanics, where phase-space methods are crucial for simplifying quadratic Hamiltonians through diagonalization.

4.1.4 The Squeeze Operators

The term “squeeze” mentioned above comes from the behavior of the transformation in phase space. The matrix

$$S(\theta) = \begin{pmatrix} \cosh\theta & \sinh\theta \\ \sinh\theta & \cosh\theta \end{pmatrix} \tag{4.11}$$

is known as a squeezing transformation because it scales x and p differently. Specifically:

- When $\theta > 0$, $\cosh\theta > 1$ and $\sinh\theta > 0$, one of the variables is “stretched” while the other is “compressed” or squeezed;
- This is a canonical transformation, meaning it preserves the phase-space volume (the symplectic structure), but it redistributes the spread of x and p.

In classical mechanics, squeezing can relate to changing the shape of an ellipse in phase space, representing different momentum and position distributions. In quantum optics and in quantum mechanics in general, the squeezing transformations are represented by unitary operators and are crucial for altering uncertainties in x and p without violating the uncertainty principle. The standard definition of the single-mode squeeze operator is

$$U_S = \exp\left(\frac{1}{2}[z^* a^2 - z a^{\dagger 2}]\right). \tag{4.12}$$

where $z = |z|e^{i\varphi}$. The action on the ladder operators is written as

$$U_S^\dagger a U_S = a\cosh|z| - e^{i\varphi}a^\dagger \sinh|z|, \tag{4.13a}$$

$$U_S^\dagger a^\dagger U_S = a^\dagger \cosh|z| - e^{-i\varphi}a^\dagger \sinh|z|. \tag{4.13b}$$

Therefore, its action on x and p is given by

$$U_S^\dagger x U_S = \frac{1}{\sqrt{2}}\left[a^\dagger\bigg(\cosh|z| - e^{i\varphi}\sinh|z|\bigg) + a\bigg(\cosh|z| - e^{-i\varphi}\sinh|z|\bigg)\right], \tag{4.14a}$$

$$U_S^\dagger p U_S = \frac{i}{\sqrt{2}}\left[a^\dagger\bigg(\cosh|z| + e^{i\varphi}\sinh|z|\bigg) - a\bigg(\cosh|z| + e^{-i\varphi}\sinh|z|\bigg)\right]. \tag{4.14b}$$

A special case happens when we choose z to lie in the real axis of the complex plane. For example, fixing $\varphi = \pi$, so $e^{\pm i\pi} = -1$, we obtain,

$$U_S^\dagger x U_S = e^{z}x, \tag{4.15a}$$

$$U_S^\dagger p U_S = e^{-z}p. \tag{4.15b}$$

We now observe more clearly that the squeeze operator squeezes or stretches x and p depending on the squeeze parameter z. This shows a clear relationship with the aforementioned squeeze matrix.

Let us now introduce a general squeeze operator for an arbitrary number of modes and expanded degrees of freedom. We define a operator acting on $R = (x, p)^T$, with $x = (x_1, x_2, \ldots, x_n)^T$ and $p = (p_1, p_2, \ldots, p_n)^T$,

$$U_S = \exp\bigg(-\frac{i}{2}R^T\xi R\bigg), \tag{4.16}$$

where ξ is a symmetric $2n \times 2n$ matrix. Thus, the action of U_S on R reads

$$U_S^\dagger R U_S = e^{\sigma\xi}R \equiv SR, \tag{4.17}$$

with $S = e^{\sigma\xi}$ belonging to the symplectic group $\mathrm{Sp}(2n, \mathbb{R})$, where $S^T\sigma S = \sigma$ and σ is the symplectic matrix.

Note that if the diagonal terms in ξ vanish, we obtain, in the single-mode case, $-iR^T\xi R/2 = z({a^\dagger}^2 - a^2)/2$, showing the correspondence between standard and general photon squeeze unitary operators, when a single parameter simplification is chosen.

4.2 Gaussian states

In section 4.1.3, a brief introduction to the diagonalization of general quadratic Hamiltonians were shown. To recap, consider a general quadratic Hamiltonian for n modes

$$H = \frac{1}{2}R^T h R, \tag{4.18}$$

where $R = (x_1, x_2, \dots, x_n, p_1, p_2, \dots, p_n)^T$ is the quadrature vector and h is a symmetric $2n \times 2n$ matrix. The CCR are given by Eq. 4.4.

The Williamson theorem states that any positive-definite symmetric matrix h can be written as $h = S^T \nu S$, where S is a symplectic matrix ($S\sigma S^T = \sigma$) and ν is a diagonal matrix of eigenvalues (positive, corresponding to normal modes) [147]. Under the symplectic transformation S, the quadratures transform as $R \to SR$. Substituting this into the Hamiltonian gives

$$H = \frac{1}{2} R^T h R = \frac{1}{2}(SR)^T \nu (SR) = \frac{1}{2}\tilde{R}^T \nu \tilde{R}, \tag{4.19}$$

in terms of the transformed quadratures $\tilde{R} = SR$. This is now diagonal in the transformed basis. Each term corresponds to a decoupled mode with eigenfrequency ν_i. The symplectic transformation associated with h can be implemented by a squeezing operator. Specifically, the symplectic matrix acts on the quadratures, modifying their variances and correlations according to the squeezing parameters. The unitary operator $U_S = \exp\left(-\frac{i}{2} R^T \xi R\right)$ in Hilbert space generates this action. Thus, the diagonalization of h corresponds to a squeezing transformation in the phase space of the quadratures.

To describe *all pure Gaussian states*, displacement is necessary in addition to squeezing. A general quadratic Hamiltonian can include linear terms of the form $R^T \alpha$, where α is a vector representing a shift in phase space,

$$H = \frac{1}{2} R^T h R + R^T \alpha. \tag{4.20}$$

The linear term $R^T \alpha$ is eliminated by a displacement operator $U_d(\Delta_R)$ (defined in Eq. 2.38), where Δ_R corresponds to the shift $U_d(\Delta_R)^\dagger R U_d(\Delta_R) = R + \Delta_R$, with $\Delta_R = (\Delta_x, \Delta_p)$, where Δ_x and Δ_p being N-dimensional displacement vectors. After applying the displacement, the Hamiltonian becomes quadratic in the new phase-space coordinates, leaving the diagonalization by the squeeze operator intact. Thus, the most general pure Gaussian state is generated by

$$|GS\rangle = U_d U_S |0\rangle . \tag{4.21}$$

This is consistent with the fact that all pure Gaussian states are generated by unitary operations derived from quadratic Hamiltonians acting on the vacuum state. More generally, Gaussian states are all the the ground and thermal states of quadratic Hamiltonians with a positive definite Hamiltonian matrix.

A Gaussian state can be fully specified by

- The displacement vector

  $$(\Delta_R)_i = \langle GS| R_i |GS\rangle , \tag{4.22}$$

  representing the first moments (mean values) of the quadratures. Since the displacement operator modifies the mean values of R, the first moments of the state directly encode the displacement vector.

- The covariance matrix Γ, which encodes second-order moments,

  $$\Gamma_{ij} = \frac{1}{2}\langle GS|\{\delta R_i, \delta R_j\}|GS\rangle, \tag{4.23}$$

where $\delta R = R - \langle R \rangle$ are the fluctuations of the quadratures around their mean values and $\{A, B\} = AB + BA$ is the anticommutator. Diagonal elements Γ_{ii} represent the variances of the quadratures, e.g., $\langle (\delta x_i)^2 \rangle$, while off-diagonal elements Γ_{ij} represent the correlations between different quadratures, e.g., $\langle \delta x_i \delta p_j \rangle$. The covariance matrix Γ thus provides a complete description of the spread and correlations of the quadrature fluctuations in a Gaussian state. For pure states, which is our case, the covariance matrix can be written in terms of a symplectic transformation S acting on the vacuum state,

$$\Gamma = SS^T. \tag{4.24}$$

This is analogous to how a multivariate normal distribution is specified by its mean vector and covariance matrix in probability theory.

In summary, the Gaussian state is a coherent squeezed state, so the unitary Gaussian operator is a combination of squeeze and displacement,

$$U_{GS} = U_d U_S = \exp\big(iR^T \sigma \Delta_R\big) \exp\left(-\frac{i}{2} R^T \xi R\right). \tag{4.25}$$

It transforms R as,

$$U_{GS}^\dagger R U_{GS} = SR + \Delta_R. \tag{4.26}$$

4.3 Unitary Dressing Transformations

This section introduces unitary dressing transformations as a key tool for handling two distinct interaction regimes. In the weak-coupling limit, the Hamiltonians are well-approximated as quadratic, making Gaussian states accurate, as detailed in the previous sections. However, when interactions become strong, this approximation fails and methods like the Lang-Firsov transformation become essential. We outline these transformations and explain how they enable a more accurate description of the system, thereby preparing us for the construction of non-Gaussian states in the next section.

4.3.1 Lang-Firsov transformation

Let us consider the popular Holstein model, defined in Chapter 3, which assumes an on-site coupling of spinless electrons with a dispersionless lattice vibration mode,

$$H = -t \sum_{\langle i,j \rangle} (c_i^\dagger c_j + H.c.) + \omega \sum_i b_i^\dagger b_i + g \sum_i n_i (b_i^\dagger + b_i), \tag{4.27}$$

Our task is to diagonalize the Hamiltonian. If the electron-phonon interaction is strong, the hopping term can be treated as a perturbation. In this case, the Hamiltonian would be diagonalizable if we get rid of the coupling term. It can be done via the Lang-Firsov canonical transformation. Before carrying out the formal transformation, we first motivate its results with a few intuitive arguments. The harmonic oscillator potential in the presence of a external force is written as

$$V(x) = \frac{1}{2} m\omega^2 x^2 - Fx. \tag{4.28}$$

For the electron-phonon coupling, the external force depends on the occupation n_{el} of the electronic state and the coupling constant g, giving $F = -\sqrt{2}gn_{el}$. To diagonalize this classical potential, complete the square

$$\begin{aligned} V(x) &= \frac{1}{2}m\omega^2x^2 + \sqrt{2}gn_{el} \\ &= \frac{1}{2}m\omega^2\left(x + \frac{\sqrt{2}gn_{el}}{m\omega^2}\right)^2 - \frac{(\sqrt{2}gn_{el})^2}{2m\omega^2}. \\ &= \frac{1}{2}\hbar\omega\left(\frac{x}{l} + \frac{\sqrt{2}g}{\hbar\omega}n_{el}\right)^2 - \frac{g^2}{\hbar\omega}n_{el}^2, \end{aligned} \tag{4.29}$$

where in the last line the equation was rewritten using the oscillator length scale $l = \sqrt{\hbar/m\omega}$. Thus, we obtain a shifted harmonic-oscillator potential, by $x_{\text{shift}} = -\frac{\sqrt{2}gn_{el}}{m\omega^2}$, and an additional negative energy shift $-\frac{g^2}{\hbar\omega}n_{el}^2$ corresponding to the energy gain due to polaron formation.

Now we turn to the explicit Lang-Firsov canonical transformation $\tilde{H} = e^S H e^{-S}$. The transformation must be unitary to preserve the Hermiticity of the Hamilton operator, so the transformation's generator S must be anti-Hermitian, $S^\dagger = -S$. The appropriate choice for S to eliminate the electron-phonon coupling is

$$S = \frac{g}{\omega}\sum_i n_i(b_i^\dagger - b_i). \tag{4.30}$$

Using the BCH formula, the transformed operators become

$$\tilde{b}_i = b_i - \frac{g}{\omega}n_i, \tag{4.31a}$$

$$\tilde{c}_i = c_i e^{-\frac{g}{\omega}(b_i^\dagger - b_i)}. \tag{4.31b}$$

This physically reflects a shift of the ions' equilibrium position,

$$\langle\tilde{x}_i\rangle = \langle x_i\rangle - \frac{\sqrt{2}g}{\omega}\langle n_i\rangle, \tag{4.32}$$

as expected from our semi-classical observations. The rotated Hamiltonian after the Lang-Firsov transformation is written as

$$\tilde{H} = -t\sum_{\langle ij\rangle}(c_i^\dagger c_j \Lambda_i^\dagger \Lambda_j + H.c.) + \omega\sum_i b_i^\dagger b_i - \frac{g^2}{\omega}\sum_i n_i^2, \tag{4.33}$$

where $\Lambda_i = \exp\Big\{-\frac{g}{\omega}(b_i^\dagger - b_i)\Big\}$. After applying the Lang-Firsov transformation to the Holstein model, the electron-phonon coupling term is eliminated, and the phonon operators instead appear in the modified hopping term. This introduces phonon-assisted processes into the hopping dynamics. However, in the limit of strong electron-phonon coupling, these processes can be treated perturbatively. To leading order, this results in a simplified Hamiltonian where the electron hopping is renormalized, effectively decoupling the phonon contributions from the electronic degrees of freedom.

4.3.2 The dressing transformation

The Lang-Firsov canonical transformation is useful in the strong coupling perturbation theory, where the modification in the hopping term is seen as a exponentially decaying effective nearest-neighbor hopping. However, away from the limiting regimes, we are still left with a electron-phonon coupling in the kinetic term, so the Hamiltonian is not diagonalized in this basis. Generally, we can construct an operator U_λ with a tunable variable λ.

We define the unitary operator U_λ inspired by the Lang-Firsov transformation, where it depends on a set of arbitrary variables $\{\lambda_i\}$. The specific form of U_λ strongly depends on the system of interest. Our main focus is in light-matter and electron-phonon systems, we will define the respective operators in the following.

Transformation in electron-phonon systems

Consider the aforementioned Holstein Hamiltonian,

$$H = -t\sum_{\langle i,j\rangle}(c_i^\dagger c_j + H.c.) + \frac{\omega}{2}\sum_i (x_i^2 + p_i^2) + g'\sum_i n_i x_i. \tag{4.34}$$

The dressing transformation is written as

$$U_\lambda = \exp\left\{ i\frac{g'}{\omega}\lambda \sum_i n_i p_i \right\}. \tag{4.35}$$

Similarly to the LF transformation, the transformed operators become

$$\tilde{x}_i = x_i - \frac{g'}{\omega}\lambda n_i, \tag{4.36a}$$

$$\tilde{c}_i = c_i e^{i\frac{g'}{\omega}\lambda p_i}. \tag{4.36b}$$

Thus, the rotated Hamiltonian, up to constant terms, reads

$$\tilde{H} = -t\sum_{\langle ij\rangle}(c_i^\dagger c_j \Lambda_i^\dagger \Lambda_j + H.c.) + \frac{\omega}{2}\sum_i (x_i^2 + p_i^2) + g'(1-\lambda)\sum_i n_i x_i + \frac{g'^2}{2\omega}(\lambda-2)\lambda\sum_i n_i^2, \tag{4.37}$$

where $\Lambda_i = \exp\{i\frac{g}{\omega}\lambda p_i\}$.

The transformation offers decoupling of electrons and phonons in the potential energy term, while adds electron-phonon coupling in the kinetic term. The kinetic part of the Hamiltonian is decoupled when $\lambda = 0$, while the potential part has no interaction when $\lambda = 1$. That way, in variational approaches, which will be introduced in the next chapter, λ is treated as a variational parameter in the range $[0, 1]$.

Generalizations

In the simple example given above, the dressing transformation considers a single parameter λ. However, even for the standard Holstein model, it would be more accurate to consider a set of parameters $\{\lambda_{ij}\}$ due to the multi-mode phononic nature of the system. For more complex systems, where interactions appear in distinct forms that would involve not only x, we can also consider $\lambda = (\lambda^x, \lambda^p)^T$. Finally, a more general dressing transformation is written as

$$U_\lambda = \exp\left\{ i\frac{g'}{\omega}\sum_{i,j,\sigma} n_{i\sigma}(\lambda_{ij}\cdot R_j)\right\}, \tag{4.38}$$

with $\lambda_{ij} = (\lambda^x_{ij}, \lambda^p_{ij})^T$.

Transformation in light-matter systems

The most paradigmatic model for light-matter interactions, the Dicke model, defined in Eq. 1.1 and widely studied in this work, is given by

$$\begin{aligned} H &= \omega\left(a^\dagger a + \frac{1}{2}\right) + \frac{\omega_0}{2}\sum_{i=1}^{N}\sigma_i^z + \frac{g}{\sqrt{N}}\sum_{i=1}^{N}\sigma_i^x(a+a^\dagger) \\ &\equiv \frac{\omega}{2}(x^2+p^2) + \omega_0 s^z + g' s^x x, \end{aligned} \tag{4.39}$$

where $x = (a^\dagger + a)/\sqrt{2}$, $p = i(a^\dagger - a)/\sqrt{2}$, $s^\alpha = \sum_i \sigma_i^\alpha/2$, and $g' = 2g/\sqrt{j}$ with $j = N/2$.

The dressing transformation is written as

$$U_\lambda = \exp\left\{ i\lambda\frac{g'}{\omega}s^x p\right\}. \tag{4.40}$$

It transforms x as,

$$U_\lambda^\dagger x U_\lambda = x - \frac{\lambda g'}{\omega}s^x, \tag{4.41}$$

where we used $e^{sB}Ae^{-sB} = A + s[B,A]$. The unitary operator also transforms the spin operators. We can use the properties of the spin Lie algebra to calculate the spin rotations. Let us first consider a single spin system, we obtain the rotation for the given transformation $U = e^{i\frac{\theta}{2}\sigma^x}$ as

$$e^{-i\frac{\theta}{2}\sigma^x}(\mathbf{u}\cdot\sigma)e^{i\frac{\theta}{2}\sigma^x} = u_x\sigma^x + \sigma^y(u_y\cos\theta - u_z\sin\theta) + \sigma^z(u_z\cos\theta + u_y\sin\theta), \tag{4.42}$$

where $\mathbf{u} = (u_x, u_y, u_z)$ and $\sigma = (\sigma^x, \sigma^y, \sigma^z)$. In our case, the dressing transformation is given by the collective spin $s^\alpha = \sum_j \sigma_j^\alpha/2$. Defining,

$$U_\lambda = \exp\left\{ i\lambda\frac{g'}{\omega}s^x p\right\} \equiv \exp\left\{ i\frac{\theta(\lambda)}{2}\sum_j \sigma_j^x\right\} = \prod_j \exp\left\{ i\frac{\theta(\lambda)}{2}\sigma_j^x\right\} \tag{4.43}$$

with $\theta(\lambda) = \lambda g' p/\omega$. Let us inspect the rotation of a spin at a given site i,

$$\begin{aligned} U_\lambda^\dagger(\mathbf{u}\cdot\sigma_i)U_\lambda &= \left(\prod_j \exp\left\{ i\frac{\theta(\lambda)}{2}\sigma_j^x\right\}\right)^\dagger (\mathbf{u}\cdot\sigma_i)\left(\prod_j \exp\left\{ i\frac{\theta(\lambda)}{2}\sigma_j^x\right\}\right) \\ &= e^{-i\frac{\theta}{2}\sigma_N^x}\dots e^{-i\frac{\theta}{2}\sigma_i^x}\dots e^{-i\frac{\theta}{2}\sigma_1^x}(\mathbf{u}\cdot\sigma_i)e^{i\frac{\theta}{2}\sigma_1^x}\dots e^{i\frac{\theta}{2}\sigma_i^x}\dots e^{i\frac{\theta}{2}\sigma_N^x} \\ &= e^{-i\frac{\theta}{2}\sigma_i^x}(\mathbf{u}\cdot\sigma_i)e^{i\frac{\theta}{2}\sigma_i^x} \\ &= u_x\sigma_i^x + \sigma_i^y(u_y\cos\theta - u_z\sin\theta) + \sigma_i^z(u_z\cos\theta + u_y\sin\theta). \end{aligned} \tag{4.44}$$

That way, for $\mathbf{u} = \hat{\mathbf{e}}_\alpha$, with $\alpha = x, y, z$, we have[1]

$$\begin{aligned} U_\lambda^\dagger \sigma_i^x U_\lambda &= \sigma_i^x, &(4.45a)\\ U_\lambda^\dagger \sigma_i^y U_\lambda &= \sigma_i^y \cos\theta + \sigma_i^z \sin\theta \\ &= \sigma_i^y (\cos\theta + i\sigma_i^x \sin\theta) \\ &= \sigma_i^y e^{i\theta\sigma_i^x}, &(4.45b)\\ U_\lambda^\dagger \sigma_i^z U_\lambda &= \sigma_i^z \cos\theta - \sigma_i^y \sin\theta \\ &= \sigma_i^z (\cos\theta + i\sigma_i^x \sin\theta) \\ &= \sigma_i^z e^{i\theta\sigma_i^x}. &(4.45c)\end{aligned}$$

Finally, the transformation of s^z is obtained:

$$U_\lambda^\dagger s^z U_\lambda = \frac{1}{2}\sum_j \sigma_j^z \exp\left\{ i\left(\frac{\lambda g'}{\omega} p\right)\sigma_j^x \right\} \tag{4.46}$$

$$\equiv s^z \cos\left(\frac{\lambda g'}{\omega} p\right) + i s^x \sin\left(\frac{\lambda g'}{\omega} p\right), \tag{4.47}$$

where we used $\sigma^j\sigma^k = \delta_{kj}\mathbb{1} + i\varepsilon_{jkl}\sigma^l$ and $e^{ia\sigma^\alpha} = \cos a + i\sigma^\alpha \sin a$. Note that both forms are useful in distinct problems, such as averaging over the phonon or spin base states. The operators p and s^x are invariant through the U_λ transformation.

The Dicke Hamiltonian under the transformation is written as,

$$\tilde{H} = \frac{\omega}{2}(x^2 + p^2) + \frac{\omega_0}{2}\sum_j \sigma_j^z \Lambda_j + g'(1-\lambda)s^x x + \frac{{g'}^2}{2\omega}(\lambda - 2)\lambda {s^x}^2, \tag{4.48}$$

with $\Lambda_j = \exp\left\{ i\frac{\lambda g'}{\omega}\sigma_j^x p \right\}$. The transformation offers partial decoupling of spins and photons, adding an extra all-to-all spin-spin interaction, while also introduces spin-photon coupling in the free spin term.

Generalizations

For systems with more complex spin-photon and spin-spin interactions, and inhomogeneous coupling strengths or multiple modes, a more general transformation is written as

$$U_\lambda = \exp\left\{ i\frac{g'}{\omega}\sum_{i,j,\alpha} s_i^\alpha (\lambda_{ij\alpha} \cdot R_j) \right\}, \tag{4.49}$$

with $\lambda_{ij\alpha} = (\lambda_{ij\alpha}^x, \lambda_{ij\alpha}^p)^T$ and $\alpha = x, y, z$.

---

[1] The same conclusion is achieved via BCH formulas.

4.4 Non-Gaussian States

The Gaussian state ansatz, discussed in Section 2, provides an efficient framework for diagonalizing and understanding systems described by quadratic bosonic Hamiltonians. However, systems with more complex interactions, such as electron-phonon coupling or non-linear terms, require going beyond Gaussian states. Consider, for instance, the Hamiltonian $H = p^2 + x^2 + xs^z$, where s^z is a spin operator coupled to the bosonic quadrature x. In this case, Gaussian states alone cannot fully diagonalize the system because of the explicit coupling between bosonic and spin degrees of freedom.

To address this challenge, we construct the *non-Gaussian state ansatz* (NGS), which combines Gaussian states with dressing transformations to introduce controlled entanglement between bosonic and fermionic degrees of freedom. The non-Gaussian state is defined as

$$|\psi\rangle = U_\lambda(|GS\rangle \otimes |\phi\rangle), \tag{4.50}$$

where $|GS\rangle = U_{GS}|0\rangle$ is the Gaussian state in the Fock basis, as described in Section 2, $|\phi\rangle$ is the many-body fermionic state (e.g., describing ions or spins), and U_λ, described in Section 3, is the dressing transformation, which entangles the bosonic and fermionic subsystems.

The operator U_λ, inspired by the Lang-Firsov transformation, is crucial for capturing the effects of bosonic-fermionic interactions. By modifying the basis states of the system, U_λ enables a variational approach to diagonalize Hamiltonians that go beyond purely quadratic forms.

Example: Dicke model

The Dicke model, discussed in Chapter 2, is a paradigmatic model that involves spin-photon interactions. By completing squares, we observe that this Hamiltonian is quadratic in the photon degrees of freedom:

$$H = \frac{\omega}{2}p^2 + \frac{\omega}{2}\left(x + \frac{g'}{\omega}s^x\right)^2 + \left(\omega_0 s^z - \frac{g'^2}{2\omega}s^{x2}\right). \tag{4.51}$$

We then observe that the spin-photon interaction adds an effective photon-mediated all-to-all spin interaction, similar to the polaron-shifting in the Holstein model. For this Hamiltonian, the Gaussian ansatz can effectively describe the bosonic subsystem alone, but it cannot capture the spin-photon correlations induced by the coupling term $g's^x$. In this case, the dressing transformation U_λ generates a new basis where the resulting states are entangled in a non-Gaussian way. The new basis states accounts for both the quadratic bosonic system and the spin-photon interaction, providing a more accurate representation of the system's ground and possibly excited states.

The NGS is given by a combination of the aforementioned approaches: a Gaussian state and a dressing transformation. The new basis states that aim to diagonalize the system is then called non-Gaussian states,

$$|\psi\rangle = U_\lambda(|GS\rangle \otimes |\phi\rangle), \tag{4.52}$$

where $|\phi\rangle$ is the many-body state of the ions and $|GS\rangle = U_{GS}|0\rangle$ in the Fock basis.

5

The Hybrid Method

There are only a handful of quantum mechanical problems for which exact analytical solutions are known. Classic examples include the particle-in-a-box, harmonic oscillator, rigid rotor, and the hydrogen atom, where the Schrödinger equation can be solved precisely. However, as the number of interacting particles increases—especially in systems involving more than two particles—analytical solutions become practically impossible, requiring the development and use of approximate methods. Variational methods play a central role in addressing such complex problems in classical and quantum mechanics. These methods, deeply rooted in the calculus of variations, have historical origins in surveying and optics. The rope stretchers of ancient Egypt measured distances by stretching corded ropes between two points to determine the shortest path. In Geographia (Bk 1, Ch 2), Claudius Ptolemy emphasized correcting deviations from a straight course. In ancient Greece, Euclid stated in Catoptrica that the angle of incidence equals the angle of reflection, and Hero of Alexandria later demonstrated that this corresponds to the shortest path and least time. The first explicit variational principles emerged in the 17th and 18th centuries: Fermat's principle of least time (1662) described the path of light in optics, while Maupertuis' principle of least action (1744) extended such ideas to mechanics. Euler and Lagrange formalized variational calculus in the 18th century, culminating in Hamilton's formulation, which provided a unifying framework for classical mechanics. Originally employed by Lord Rayleigh in 1873 to compute vibration frequencies in mechanical systems, variational methods have since found profound applications in quantum mechanics. From Feynman's path integral formulation to the Hartree-Fock method and beyond, variational approaches have become indispensable for calculating approximate wave functions [87, 76].

In many-body physics, where exact solutions are hard to find, variational methods provide a powerful framework. Systems such as multi-electron atoms, molecules, and the theory of superconductivity exemplify scenarios where these techniques can shine. Variational Monte Carlo exemplifies a powerful variational method, employing stochastic sampling to optimize a trial wavefunction and approximate ground states of quantum systems. The density matrix renormalization group (DMRG), widely used in this work, exemplifies a variational method, employing a matrix product state (MPS) ansatz to efficiently approximate ground states of quantum systems. Variational methods, based solely on the variational principle—which is the foundation of our hybrid approach—provide a powerful framework for approximating ground states by optimizing a trial wavefunction to minimize energy. While these methods are both important and effective, their accuracy and applicability strongly depend on the choice of the trial wavefunction, which must be carefully designed to capture the essential correlations of the system. While these methods have achieved remarkable success, they also encounter limitations when applied to strongly interacting systems. DMRG, despite its efficiency in one-dimensional systems, faces challenges in higher dimensions and for systems with long-range correlations. Similarly, purely variational approaches can falter when the ansatz fails to adequately capture the complexities of the system. Exact method, such as the exact diagonalization (ED), addresses some of these issues, but struggles with scalability due to the exponential growth of the Hilbert space.

To address these limitations, this chapter introduces a hybrid method that combines the strengths of a variational non-Gaussian state (NGS) optimization with either DMRG or ED solvers. The NGS-DMRG/ED method is designed to overcome the specific challenges posed by strongly correlated systems, such as hybrid spin-photon and electron-phonon interactions, by leveraging an ansatz that entangles photonic and atomic components through a controlled variational approach. This method not only bridges the gap between purely variational techniques and many-body solvers but also provides a flexible framework that can adapt to the demands of different systems. This chapter is split into three parts: a quick recap about the variational principle, followed by a discussion about time-dependent variational principles and the geometrical formulation adopted in our work; finally, we present our hybrid numerical approach.

5.1 The variational principle

To estimate the ground state of a given system, we can try to establish an upper bound for the ground state energy. Suppose that the (unknown) set of eigenstates of the Hamiltonian H is given by $H\left|\psi_j\right\rangle = E_j\left|\psi_j\right\rangle$. If we take a normalized trial wavefunction $|\phi\rangle$, how close can we get to the ground state? To define this limit, we can write the energy $\mathcal{E} = \langle\phi| H |\phi\rangle$ in terms of the true basis set as

$$\mathcal{E} = \sum_{ij} \langle\phi|\psi_i\rangle \langle\psi_i| H |\psi_j\rangle \langle\psi_j|\phi\rangle = \sum_i |\langle\phi|\psi_i\rangle|^2 E_i = E_0 + \sum_{i\neq 0} |\langle\phi|\psi_i\rangle|^2 (E_i - E_0), \tag{5.1}$$

but both $|\langle\phi|\psi_i\rangle|^2$ and $(E_i - E_0)$ should be positive, thus

$$\boxed{\mathcal{E} \geq E_0}. \tag{5.2}$$

So it makes an upper bound of the ground state energy. The lower we can make the energy $\mathcal{E}$, the closer it will be to the actual ground state energy, and $|\phi\rangle$ to $|\psi_0\rangle$.

The *variational method* explores that upper bound limit by choosing a clever trial wavefunction, the ansatz, $|\phi(\alpha)\rangle$, and minimizing $\mathcal{E}(\alpha)$ over the *variational* parameter α. We know from calculus that when the first derivative equals to zero we obtain an extreme point, while the sign of the second derivative being positive or negative denotes if it is a maximum or a minimum. Thus, next step to obtain the best approximation is to calculate

$$\frac{\partial \mathcal{E}}{\partial \alpha} = 0 \quad \text{and} \quad \left.\frac{\partial^2 \mathcal{E}}{\partial \alpha^2}\right|_{\alpha_0} \geq 0. \tag{5.3}$$

Note that in this example $|\psi(\alpha)\rangle$ is a family of wavefunctions of a single parameter α. This is usually not the case, as in general a set of variational parameters form the wavefunction ansatz, and a simple analytical minimization is not possible. In strongly-correlated many-body systems, which is the main interest of this work, the wavefunction ansatz can have a level of complexity that makes the use of numerical optimization methods necessary. However, the key for obtaining a good approximation is the first step, as a perfect choice of the trial wavefunction leads to the true ground state. On the other hand, if you guess poorly, the upper bound is too large, and the result is not helpful. The error $\mathcal{E} - E_0$ can be obtained by writing the trial wavefunction in terms of the true ground state and a small wavefunction orthogonal to it as $|\phi\rangle = |\psi_0\rangle + |\delta\rangle$,

$$\mathcal{E} = \langle\phi| H |\phi\rangle = E_0 + \langle\delta| H |\delta\rangle \equiv E_0 + \mathcal{O}(\delta^2), \tag{5.4}$$

which means the error is quadratic. Here, we used $H|\psi_0\rangle = E_0$ (with E_0 real) and the orthogonality condition $\langle\delta|\psi_0\rangle = 0$. It is of major importance to choose a wavefunction that is motivated by the physics of the system, preserves important symmetries, has a convergent integral, asymptotes correctly, and so on.

5.2 Time-dependent variational principles

In the traditional (time-independent) variational approach, one chooses a family of trial wavefunctions $\{|\Psi(\boldsymbol{\alpha})\rangle\}$ that depend on a set of variational parameters $\boldsymbol{\alpha}$. By minimizing the expectation value of the Hamiltonian, $\langle\Psi(\boldsymbol{\alpha})| H |\Psi(\boldsymbol{\alpha})\rangle$, one obtains an approximate ground state. While this method is extremely useful for stationary problems, many physical processes require a fully time-dependent treatment governed by the Schrödinger equation

$$i\hbar\frac{\partial}{\partial t}|\psi(t)\rangle = H|\psi(t)\rangle\,. \tag{5.5}$$

For complex or many-body systems, solving this equation directly can become prohibitively expensive. Time-dependent variational methods address this challenge by extending the variational principle to *dynamics*.

5.2.1 The Dirac–Frenkel-McLachlan Variational Principle: Geometrical Formulation

A particularly elegant formulation of the time-dependent variational method is given by the Dirac–Frenkel-McLachlan variational principle [115, 12, 79]. In essence, one restricts the wavefunction to lie on a (possibly high-dimensional) *submanifold* $\mathcal{M}$ of the full Hilbert space $\mathcal{H}$. A point $u \in \mathcal{M}$ may represent, for instance, a Slater determinant for fermionic systems, a Gaussian wave packet, or a tensor-network state; the key is that u must remain in $\mathcal{M}$ throughout the time evolution.

Let $\mathcal{M} \subset \mathcal{H}$ be a smooth manifold of trial states. For each $u \in \mathcal{M}$, its tangent space is denoted $T_u\mathcal{M}$[1]. We are interested in approximating the solution $\psi(t)$ of the Schrödinger

---

[1] The tangent space consists of the derivatives of all differentiable paths on $\mathcal{M}$ passing through u.

equation with a path $u(t)$ on the manifold $\mathcal{M}$, assuming that initially $u(0) = \psi(0) \in \mathcal{M}$. The path $t \mapsto u(t) \in \mathcal{M}$ is chosen such that the time derivative $\dot{u}(t) \in T_u\mathcal{M}$ is as closest as possible to $(1/i\hbar)Hu$. In other words, the residual in the Schrödinger equation must be orthogonal to the tangent space [33],

$$\left\langle v \middle| \frac{\mathrm{d}u}{\mathrm{d}t} - \frac{1}{i\hbar}Hu \right\rangle = 0 \quad \forall v \in T_u\mathcal{M}. \tag{5.6}$$

Interestingly, following the equation above, one observes that if $\mathcal{H} = L^2(\mathbb{R}^{3N})$ describes N spinless fermions without pairing, and $\mathcal{M}$ is the set of all N-particle Slater determinants, it yields what is known today as the time-dependent Hartree–Fock equations.

An equivalent alternative definition, that lies on the fact that the path can be also determined by choosing its derivative as the orthogonal projection of $(1/i\hbar)Hu$ onto the tangent space, was derived by Frenkel [47]. Defining $P_{T_u\mathcal{M}}$ as an orthogonal projection operator onto $T_u\mathcal{M}$, one can write

$$\frac{\mathrm{d}u}{\mathrm{d}t} = P_{T_u\mathcal{M}}\left(\frac{1}{i\hbar}Hu\right). \tag{5.7}$$

However, these approaches were criticized by McLachlan [94] who instead proposed the a least-squares approach alternative where one has to minimize $||\dot{u} - (1/i\hbar)Hu||^2$, which ends up with a similar condition to Dirac's,

$$\mathrm{Im}\left\langle v \middle| \frac{\mathrm{d}u}{\mathrm{d}t} - \frac{1}{i\hbar}Hu \right\rangle = 0 \quad \forall v \in T_u\mathcal{M}. \tag{5.8}$$

Both variational principles were investigated by several authors, showing that these are equivalent if both v and v^* are possible variations. Thus, in the Dirac–Frenkel-McLachlan variational principle, the condition $T_u\mathcal{M}$ *is a complex linear space* holds, with $v, v^* \in T_u\mathcal{M}$.

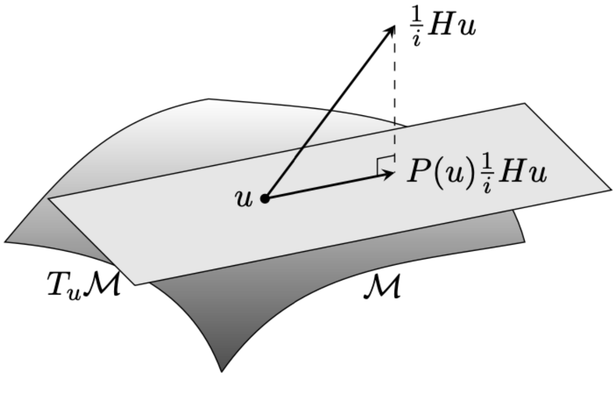

Figure 5.1: Vectors and manifolds for the Dirac-Frenkel-MacLachlan variational method. At a point u we obtain the tangent space to the manifold $\mathcal{M}$. The standard evolution has to be projected back to the tangent space via $P(u)$. Adapted from [11].

This succinctly encodes the principle's geometric character: at each instant, the system evolves in the "best possible direction" within the chosen manifold, as close as possible (in the Hilbert space norm) to the exact direction $Hu/i\hbar$. Figure 5.1 illustrates that the true

Schrödinger evolution is tilted out of $\mathcal{M}$ so, at every time step, it gets projected back onto the tangent space to remain on $\mathcal{M}$. This geometric viewpoint is particularly useful for many-body systems. In general, one can choose sophisticated ansätze, such as quasifree states with pairing, tensor network states, or correlated Gaussian states—for which the tangent space is still substantially smaller than the full Hilbert space. This is why the time-dependent variational method is so powerful, it replaces the full wavefunction evolution problem with a set of ordinary (or low-dimensional partial) differential equations for the time dependence of the variational parameters that define the ansatz $|u(\alpha(t))\rangle$.

With this geometric perspective in hand, we are now prepared to describe how the imaginary-time variant of the time-dependent variational method can be used to obtain ground-state wavefunctions efficiently.

5.2.2 Imaginary-time evolution

For a time-independent Hamiltonian H, the time-dependent Schrödinger (TDSE) in one dimension has a straightforward solution. We first solve the eigenvalue problem, i.e. the time-independent Schrödinger equation, $H|\psi_n\rangle = E_n|\psi_n\rangle$, write $|\Psi(t)\rangle$ in the eigenstates basis (at $t = 0$), and solve the equation. Thus, one can obtain its time dependence as

$$|\Psi(t)\rangle = \sum_n c_n e^{-iE_n t/\hbar}|\psi_n\rangle . \tag{5.9}$$

By a simple change of variables, $\tau = it$, Eq. 5.5 becomes

$$-\hbar\frac{\partial}{\partial\tau}|\Psi(\tau)\rangle = H|\Psi(\tau)\rangle , \tag{5.10}$$

which has solution

$$|\Psi(\tau)\rangle = \sum_n c_n e^{-E_n\tau/\hbar}|\psi_n\rangle . \tag{5.11}$$

While the TDSE shows a oscillatory solution with a frequency proportional to the eigenenergy E_n [conf. Eq. 5.9], we observe in Eq. 5.11 that in an imaginary time τ, the system shows an exponential decay with a rate proportional to E_n.

The important takeaway from the imaginary-time representation is its asymptotic behavior. For a large enough $\tau \gg 1$, the dominant term in the sum, i.e. the slowest decaying, is $n = 0$, that is,

$$|\Psi(\tau \gg 1)\rangle \approx c_0 e^{-E_0\tau/\hbar}|\psi_0\rangle . \tag{5.12}$$

Therefore, by evolving the system in “imaginary time”, we can obtain the ground state of the Hamiltonian as the long imaginary time limit. This will only work if in the initial state there is some overlap with the ground state. If not, the long imaginary time evolution will instead lead to the lowest energy state present in the initial expansion.

In practice, the eigenbasis is unknown, and one can rely on the imaginary-time evolution of the variational state ansatz $|\Psi(\tau)\rangle \equiv |\Psi(\boldsymbol{\alpha}(\tau))\rangle$ knowing that the lowest state whitin the variational manifold will be achieved. This is usually a less expensive and more physically driven way to minimize the variational parameters, which substitutes the trivial minimization (Eq. 5.3) from basic calculus. The most direct approach is to simply follow Eq. 5.10 and then renormalize $|\Psi(\tau)\rangle$ after each step to keep its norm finite. This procedure progressively filters out higher-energy components until only the ground-state component remains (up to an overall norm). An alternative (but equivalent) method is to explicitly shift the Hamiltonian by some reference energy $(H-E)\,|\Psi(\tau)\rangle$. If E were exactly the ground-state energy, $|\Psi(\tau)\rangle$ would remain at fixed norm rather than decaying or blowing up exponentially. In practice, E is replaced by the instantaneous variational energy $\langle\Psi(\tau)|\,H\,|\Psi(\tau)\rangle$, which serves as a self-consistent guess for the current state's energy and stabilizes the algorithm. Another possibility is to work with $|\Psi'(\alpha,\kappa,\phi)\rangle = e^{\kappa+i\phi}\,|\psi(\alpha)\rangle$, where the evolution of $\kappa(\tau)$ will ensure normalization and ϕ here works just as a global phase but in the context of combining multiple $|\Psi\rangle$ it becomes also necessary. In this work, we did not use $|\Psi'\rangle$ and take advantage of the geometric formulation of the method instead. In the left hand side of Eq. 5.10, we obtain the tangent vectors $|v_\mu\rangle$ via $\frac{\partial}{\partial\tau}\,|\Psi(\alpha_\mu)\rangle = \frac{\mathrm{d}\alpha^\mu}{\mathrm{d}\tau}\,|v_\mu\rangle$, shortly described in the previous subsection. However, two Hilbert space vectors can represent the same variation on $|\Psi\rangle$ if they differ by $|v\rangle - |\tilde{v}\rangle = c\,|\Psi\rangle$. Instead, we choose a unique representative by requiring $\langle v|\Psi\rangle = 0$, so that the tangent vectors are given by $|V_\mu\rangle = \mathbb{Q}_\Psi \frac{\partial}{\partial\alpha^\mu}\,|\Psi(\alpha)\rangle$. In that way, we can identify the tangent space at each point with a Hilbert space $\mathcal{H}_\Psi^\perp = \mathrm{span}_{\mathbb{R}}\{|V_\mu\rangle\}$. Indeed, one has to identify the tangent space vectors and project the right hand side onto the tangent space as

$$\mathbb{Q}_\Psi\partial_\tau\,|\Psi(\tau)\rangle = -\mathbb{P}_\Psi(H-E(\tau))\,|\Psi(\tau)\rangle\,. \tag{5.13}$$

obtaining the imaginary equations of motion $\partial_\tau\boldsymbol{\alpha}(\tau) = \Phi(\tau)$, where $\Phi(\tau)$ is the flow map. Here, $\mathbb{P}_\Psi$ is defined as the projection onto the tangent space.

This procedure guarantees the monotonic decrease of energy while maintaining the normalization of the wave function. The tangential plane projection leads to a set of imaginary equations of motion for the variational parameters in τ, the flow equations.

5.3 Density matrix renormalization group

The density matrix renormalization group (DMRG) is a powerful numerical method designed to study strongly correlated one-dimensional quantum systems [143, 144]. It works by iteratively building up the system in a controlled way and retaining only the most relevant states at each step. By partitioning the system into a system block and an environment block, DMRG uses the eigenvalue spectrum of the reduced density matrix to select the optimal subspace that best approximates the target state, usually the ground state. Mathematically, if the full system is in a pure state $|\psi\rangle$, the reduced density matrix for the system block is defined as $\rho_S = \mathrm{Tr}_E\,|\psi\rangle\,\langle\psi|$, where the S and E subscripts denote system and environment, respectively, which can be diagonalized as $\rho_S\,|\alpha\rangle = w_\alpha\,|\alpha\rangle$. The states with the largest eigenvalues w_α are retained to form an optimal truncated basis. In practice, one keeps M states such that the truncation error $\epsilon = 1 - \sum_{\alpha=1}^{M} w_\alpha$, is minimized. In terms of the Schmidt decomposition, the wave function can be written as

$$|\psi\rangle = \sum_{\alpha=1}^{\chi} \sqrt{w_\alpha}\,|\alpha\rangle_S\,|\alpha\rangle_E\,, \tag{5.14}$$

and the approximation made by retaining only the M dominant terms is variationally optimal. This approach is equivalent to optimizing over a class of matrix-product states, which naturally capture the entanglement structure of one-dimensional systems. The success of DMRG relies on the typically rapid decay of the eigenvalues in many gapped systems, allowing for high accuracy with a small number of retained states. For further details, see Schollwöck's review [125].

5.4 The hybrid approach

The methods described in this chapter are extremely useful to numerically obtain a good approximation of the ground state properties of a multitude of strongly correlated systems, and can be easily applied to study dynamics as well. However, hybrid systems, such as electrons and phonons or atoms and light, combine distinct components, fermions and bosons, each with unique nature and demand, that pose significant challenges to these traditional methods. Bosonic systems belong to an infinite-dimensional Hilbert space with possibly large occupation numbers, which means that variationally working on a much narrow Hilbert space denoted by e.g. non-Gaussian states can be much more efficient [58, 24] than exact numerical methods where the Hilbert space must be truncated to a given small occupation number. On the other hand, fermionic degrees of freedom exhibit strong correlations that require many-body techniques [143, 144, 146, 83], such as DMRG, or quantum computational approaches [39, 27, 21]. While these methods have proven effective in certain classes of systems, they are limited when applied to hybrid systems. Introducing correlations between components can be done using efficient techniques such as the Lang-Firsov (LF) transformation [41], as shown in chapter 4, and Jastrow wavefunctions [72, 106]. For instance, an initial attempt to circumvent these numerical challengies on electron-phonon models was proposed by Takada et al. [132]. Building a non-Gaussian variational ansatz (without squeeze) they obtained an effective electronic Hamiltonian which has a analytical approximate solution. The minimized variational parameters from the average energy are plugged into the energy expression giving a good approximation of the ground state energy of the Hubbard-Holstein model. This procedure is limited to systems where the effective Hamiltonian has an analytic solution. Along these lines, Wang et al. developed a hybrid method that treats the effective Hamiltonian with an exact numerical method while the bosonic component is described by a non-Gaussian state which is treated via variational optimization as well. The so-called non-Gaussian exact diagonalization (NGSED) method iteratively refines the solution at each step until convergence [138, 139].

In chapter 6, we apply the hybrid method for electron-phonon systems, in special the Hubbard-Holstein model, to investigate its critical phenomena. Moreover, as shown in chapter 7, we developed an adaptation of this method for light-matter systems enabling the investigation of the phases with strong spin interactions. However, in both cases, we swapped ED by DMRG. In short, through the NGS-type of wavefunctions, the ground state of the Hamiltonian can be obtained by minimizing the variational energy given by,

$$\begin{aligned} E(\boldsymbol{\Delta}_R, \boldsymbol{\xi}, \lambda, |\phi\rangle) = \langle H \rangle_{\text{NGS}} &= \langle \phi | \langle \psi_{\text{ph}} | U_\lambda^\dagger H U_\lambda | \psi_{\text{ph}} \rangle | \phi \rangle \\ &= \langle \phi | H_{\text{eff}} | \phi \rangle . \end{aligned} \tag{5.15}$$

There are two types of variational parameters to optimize, corresponding to the self-consistent iterations of two solvers: the variational parameters $\boldsymbol{\Delta}_R, \boldsymbol{\xi}, \lambda$ determine the NGS transforma-

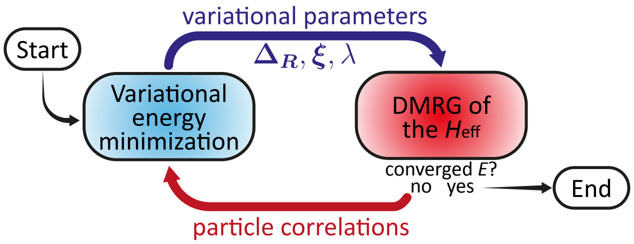

Figure 5.2: Flow diagram of the NGS-DMRG method. Starting with an initial guess we minimize the variational energy, obtaining the optimal variational parameters. We then feed them back into the effective Hamiltonian which is solved via DMRG giving the particle correlations. The workflow is repeated until convergence.

tion and the bosonic state, optimized through the imaginary-time equations of motion; the many-body state $|\phi\rangle$ is represented by the MPS variational states and the tensor coefficients are obtained with DMRG. In the latter step, all other variational parameters are fixed and $|\phi\rangle$ can be obtained by solving the effective fermionic Hamiltonian given by

$$H_{\rm eff}(\boldsymbol{\Delta}_R, \boldsymbol{\xi}, \lambda) = \langle\psi_{\rm ph}| U_\lambda^\dagger H U_\lambda |\psi_{\rm ph}\rangle\,. \tag{5.16}$$

The effective Hamiltonian, obtained after tracing out the bosonic degrees of freedom, is useful for understanding the nature of the induced effective fermionic interactions. Additionally, the ground state of the many-body fermionic subsystem $|\phi\rangle$ is related to the ground state of the effective Hamiltonian. Note that since the $H_{\rm eff}$ does not include the unbounded bosonic Hilbert space, there is no necessity to traversing and truncating the bosonic Hilbert space. As shown in Fig. 5.2, these two iterations optimize all variational parameters in the wavefunction in a self-consistent manner, ensuring the energy decrease.

In the following chapters, we examine the ground-state properties of various multi-component systems. When these systems involve distinct, interacting components, a method able to span the entire Hilbert space becomes essential. Although developing such a framework is a significant work, it ultimately proves worthwhile, as demonstrated by the results presented in this thesis.

6

Simulations of electron-phonon coupling models

A number of theoretical proposals for quantum simulation of electron-phonon models using molecules as well as ions exists [113, 108, 59, 68]. However, they have stringent requirements and can lack versatility. For example, in order to crystallize the molecules one needs extremely low temperatures, while in ion-atom systems the relevant energy scales are quite separated. Here we focus on a different type of mixture involving an array of Rydberg atoms and a ground state gas. In most experimental realizations, the Rydberg states are repelled by optical traps and the laser field must be turned off during experiments. However, recent developments allow for keeping the tweezer array on as well as to achieve state-insensitive traps [148, 95], leading to long lifetimes and opening the door towards a new simulation platform.

In our recent work [96], we extended this notion providing a scheme for quantum simulation of strongly correlated many-body systems. To begin, we study the phonon spectrum of a Rydberg chain showcasing its tunability. Then we argue that the array can be seen as a periodic potential for the neutral atoms (see Fig. 6.1(a)). Following that, we derive and study the full system Hamiltonian which contains atom-phonon coupling. Finally, we discuss further prospects for quantum simulation in this setup.

6.1 Quantum simulations in a Rydberg–neutral atom setup

The simplest and widely used Hamiltonian that takes into account both electron-electron and electron-phonon interactions is the Hubbard-Holstein (HH) model,

$$H = -t \sum_{\langle i,j\rangle\sigma} (c^\dagger_{i\sigma} c_{j\sigma} + \text{H.c.}) + U \sum_i n_{i\uparrow} n_{i\downarrow} + \omega \sum_i b^\dagger_i b_i + g \sum_{i\sigma} n_{i\sigma} (b^\dagger_i + b_i)\,,$$

obtained in chapter 3 under a series of approximations. The model features surprisingly rich physics as phonon-induced interactions compete with the Hubbard term [81], leading to emergence of two insulating orders with a metallic phase possibly appearing at their interplay [142, 132, 26, 63, 133, 150, 138]. The model can be easily extended which considerably increases its complexity. For instance, one could modify the last term of Eq. (6.1) by introducing nonlocal electron-phonon couplings. The extended version of the model is written

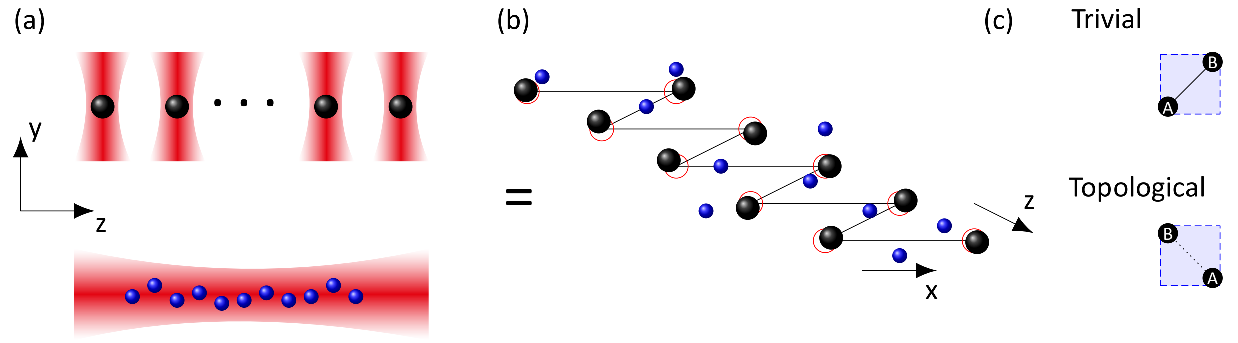

Figure 6.1: (a) Top: Red-detuned optical tweezers generating the Rydberg lattice; bottom: state-insensitive trap for the ground state atomic cloud. (b) The proposed platform. Strongly interacting Rydberg atoms (black balls) are trapped in an array of tweezers (red circles). The cloud of neutral atoms (small blue balls) is placed in a periodic lattice potential due to the Rydberg chain. The lines are to guide the eyes. (c) The unit cells generating two lattice geometries with the base atoms labeled as A and B; the interactions shown here are strong (weak) for the trivial (topological) scenario, respectively.

as

$$\mathcal{H}_{e-ph} = \sum_{\mathbf{q}} g_{\mathbf{q}}(b^\dagger_{\mathbf{q}} + b_{-\mathbf{q}})\rho_{\mathbf{q}}, \tag{6.1}$$

where $\rho_{\mathbf{q}} = \sum_{\sigma i} n_{i\sigma} e^{-i\mathbf{q}\cdot\mathbf{r}_i}$ is the electron density. While retaining a simple form, this term is rather general due to the set of free parameters $g_{\mathbf{q}}$ and can describe long-range couplings with nontrivial structure.

Furthermore, the phonon as well as electron dispersion can feature a richer and more realistic structures. To showcase this, here we use a zig-zag configuration of Rydberg atoms with anisotropic interactions instead of a more standard linear (1D), square (2D), or cubic arrangement (3D). This choice is motivated by a recent experiment [30] which emulated the physics of the Su-Schrieffer-Heger model with topological edge states in a similar setup.

6.1.1 Topological Rydberg lattice

In our approach, the Rydberg atoms are constantly individually trapped by an array of harmonic potentials (optical tweezers) and interact with each other via dipolar interactions, which can be induced by an external field. That way, the potential energy is written as

$$V = \frac{1}{2}\sum_{n,\alpha} M_\alpha[\boldsymbol{\nu}_n(\mathbf{R}_{n\alpha} - \bar{\mathbf{R}}_{n\alpha})]^2 \quad + \sum_{\substack{nm\alpha\beta \\ (n,\alpha)\neq(m,\beta)}} \frac{V_{\mathrm{dd}}}{|\mathbf{R}_{n\alpha,m\beta}|^3}\left[1 - 3(\hat{\mathbf{m}}\cdot\hat{\mathbf{R}}_{n\alpha,m\beta})^2\right], \tag{6.2}$$

where M_α is the Rydberg atomic mass, V_{dd} is the dipole-dipole interaction constant, and $\hat{\mathbf{R}}_{n\alpha,m\beta} = \hat{\mathbf{R}}_{n\alpha} - \hat{\mathbf{R}}_{m\beta}$. The first term represents the collection of harmonic traps (optical tweezers) with frequency $\boldsymbol{\nu}_n$ that are located at fixed positions $\bar{\mathbf{R}}_{n\alpha} = \mathbf{R}_n + \boldsymbol{\rho}_\alpha$, with $\mathbf{R}_n = na\hat{\mathbf{z}}$ the cell position and $\boldsymbol{\rho}_\alpha$ the basis coordinates, forming a zig-zag chain in the x–z plane, while the second term represents the dipole-dipole interaction, where $\hat{\mathbf{m}} = \mathbf{m}/m$ is the magnetic dipole moment direction that is fully defined by its polar θ and azimuthal ϕ angles. As shown in Fig. 6.1(b)-(c), there are two zig-zag configurations, defined via: $\boldsymbol{\rho}_{A,B} = \mp\Delta/2\hat{\mathbf{x}} \mp d/2\hat{\mathbf{z}}$ and $\boldsymbol{\rho}_{A,B} = \mp\Delta/2\hat{\mathbf{x}} \pm d/2\hat{\mathbf{z}}$, the length Δ sets the distance between the two legs, while d is the spacing between the atoms in the same leg. While for $\hat{\mathbf{m}} = (0,1,0)^T$ (out of the plane), the interactions are isotropic, when $\hat{\mathbf{m}} \cdot \hat{\mathbf{R}}_{n\alpha,m\beta} = \cos\theta_m$ these two geometric configurations correspond, respectively, to the trivial and topological configurations [30, 130] [see Fig. 6.1(c)]. The trivial geometry corresponds to to forming pairs of dimers, while the topological one corresponds to leaving out two unpaired atoms at the chain edges. The dimerization happens because the trivial lattice is formed by a sequence of strong and weak bonds between neighboring atoms in legs A and B, while in the topological case the first (and last) weak bonds leaves two uncoupled atoms at the edges. We set $\theta_m = \cos^{-1}(1/\sqrt{3})$ such that there is no interaction along $\hat{\mathbf{z}}$, so that atoms in the same subchain do not interact. For simplicity, we fix $\boldsymbol{\nu}_n = \boldsymbol{\nu}$ with $\nu_{x,y,z} = \nu$ and choose $M_\alpha = M$.

Current stat-of-the-art experiments enable an arbitrary 3D setting of the tweezer traps with separations of the order of single μm. The trap frequencies can be varied as well and are typically in the ∼kHz regime. The interactions between the atoms depends on the choice of Rydberg states and can remain strong over the typical trap separation. Furthermore, it can be precisely tuned by using external electromagnetic fields, for instance by inducing and orienting the dipole moments [141].

6.1.2 Phonon spectrum

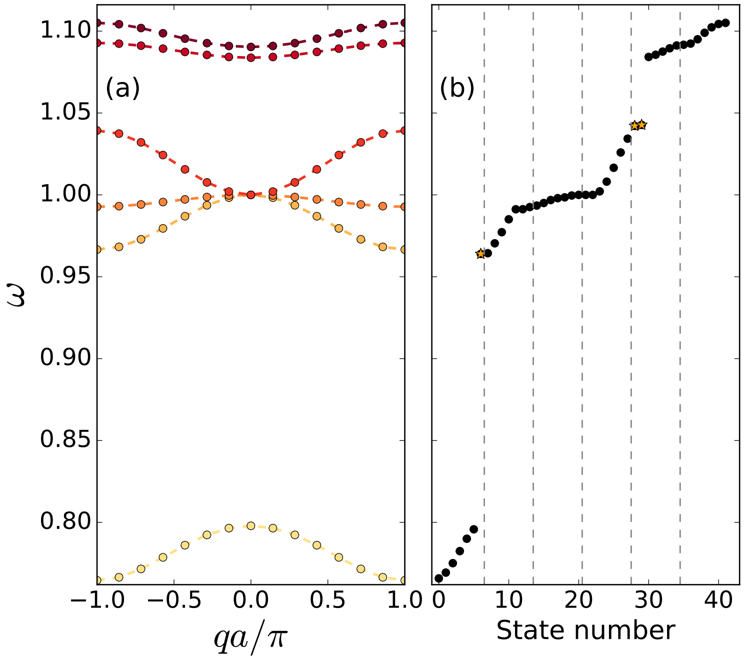

Figure 6.2: The phonon dispersion relation for (a) the translationally invariant case, (b) the topological band structure of the finite chain for $N = N_b N_c = 14, d = 2, \Delta = 1, a = 2d, \theta = \theta_m$, and $\phi = 0$. The edge states are highlighted as yellow stars in the panel (b).

We now turn to the phonon structure of the Rydberg chain. In the harmonic approximation, the normal modes are obtained from diagonalizing the harmonic matrix D, whose elements are given by all second derivatives of the potential energy at equilibrium [see Chapter 3]. Interestingly, there is only one relevant interaction length scale $\ell^5 = 3V_{dd}/M\nu^2$ within this approximation, which is widely tunable by means of the trap frequencies as well as the choice of the Rydberg level, as the dipole-dipole interaction strength scales as n^4. We further express all other length scales describing the array geometry in units of ℓ and energies in the corresponding characteristic units $M\nu^2\ell^2$. Assuming an alkaline earth atom and 10^6Hz trapping frequency, we obtain $\ell \sim 10^4$ Bohr radii.

The trivial geometry allows us to invoke translational invariance, such that $D_{\alpha i}^{\beta j}(|\mathbf{R}_n - \mathbf{R}_m|) = D_{\alpha i}^{\beta j}(\mathbf{R}_p)$ and one can reduce the problem in the quasimomemtum space to the $3N_b \times 3N_b$ dynamical matrix [86] $\tilde{D}_{\alpha i}^{\beta j}(\mathbf{q}) = \sum_n D_{\alpha i}^{\beta j}(\mathbf{R}_n) e^{i\mathbf{q}\cdot\mathbf{R}_n}$. Here, for each of the $N = N_b N_c$ allowed $\mathbf{q}$ there are $3N_b$ normal modes with frequencies $\omega_j(\mathbf{q})$ and corresponding eigenvectors $\boldsymbol{\xi}_\alpha^{(j)}(\mathbf{q})$ obeying $\sum_\alpha \boldsymbol{\xi}_\alpha^{(j)}(\mathbf{q}) \cdot \boldsymbol{\xi}_\alpha^{(j')}(\mathbf{q}) = \delta_{j,j'}$, where $j = 1, \cdots, 3N_b$ and $\alpha = 1, \cdots, N_b$, with N_c the number of cells and $N_b = 2$ the number of basis atoms. Due to the chosen geometry, in our example the quasimomentum is $\mathbf{q} = q\hat{\mathbf{z}}$ as the system is quasi-1D. Figure 6.2(a) shows its exemplary dispersion relation in the quasimomentum space.

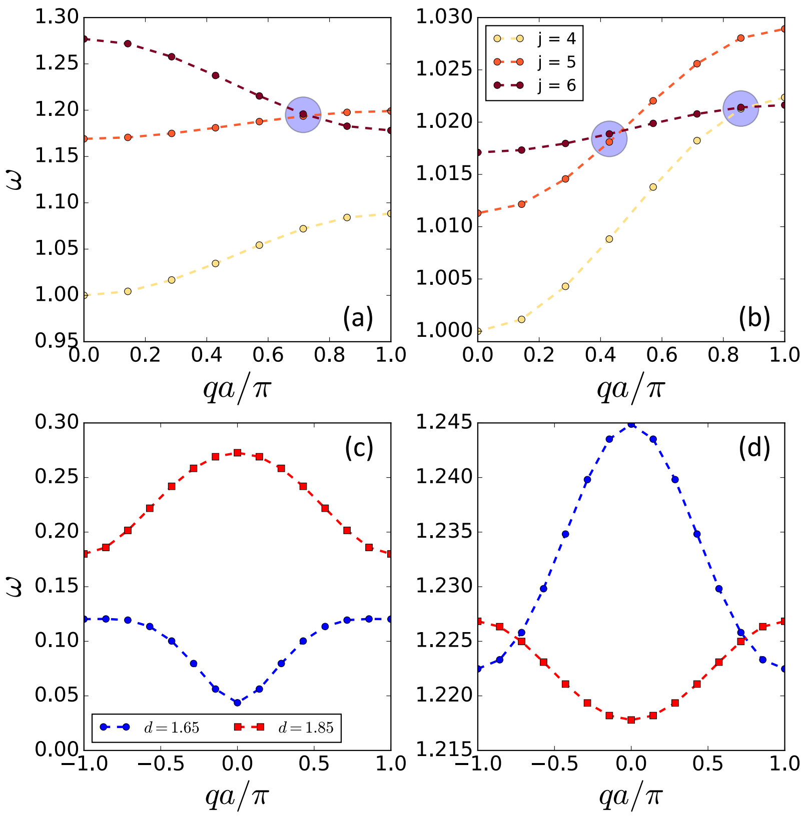

Figure 6.3: (top) Phonon spectrum of the three highest bands highlighting band crossings with a blue circle. As an example, we show for (a) $d = 1.5$ and (b) $d = 2.5$, with $N = N_b N_c = 14, \Delta = 1, a = 2d, \theta = \theta_m$, and $\phi = 0$. (bottom) Phonon spectrum of the (c) first band and (b) last band for $d = 1.65, 1.85$. We can see that there is a concavity change by varying d between the values shown. Here we set $N = N_b N_c = 14, \Delta = 1, a = 2d, \theta = \theta_m$, and $\phi = 0$.

For the topological configuration, the translational invariance can no longer be assumed.

In Figure 6.2(b) we show the dispersion relation calculated from direct diagonalization of the harmonic matrix. We observe three points which are disconnected from the bands: one in the first and two in the fifth band, which we associate with the edge states. It is important to note that even for larger N, we still see only these three disconnected points.

The system is widely tunable in terms of band geometry and shows a rich behavior which exhibits concavity changes and multiple band crossings, as shown in Fig. 6.3 for $d = 1.5$ and $d = 2.5$ for the three highest phonon modes. Furthermore, both highest and lowest bands are changing their concavity with varying the distance d. We show in Fig. 6.3 two examples of such concavity change. It is demanding to find numerically the critical value at which the concavity changes, as one encounters instabilities in the atom equilibrium positions. As demonstrated in the figure, it is located between $d = 1.65$ and $= 1.85$ for both the first and the last band.

6.1.3 Local phonon couplings

To gain more insight into the phonon mode structure, we write the second quantized Hamiltonian in the local phonon picture as [see chapter 3]

$$H = \frac{1}{2}\sum_{nmij}\left[h^{ij}_{nm}(b^{\dagger}_{n,i}b_{m,j} + b_{n,i}b^{\dagger}_{m,j}) + g^{ij}_{nm}(b_{n,i}b_{m,j} + b^{\dagger}_{n,i}b^{\dagger}_{m,j})\right], \tag{6.3}$$

with $g^{ij}_{nm} = (1 - \delta_{nm}\delta_{ij})D^{ij}_{nm}/2M\sqrt{\Omega_{n,i}\Omega_{m,j}}$ and $h^{ij}_{nm} = \delta_{nm}\delta_{ij}\Omega_{n,i} + g^{ij}_{nm}$, and $n, m \in [0, N]$ being the overall atom index where $N = N_b N_c$, as defined in chapter 3.

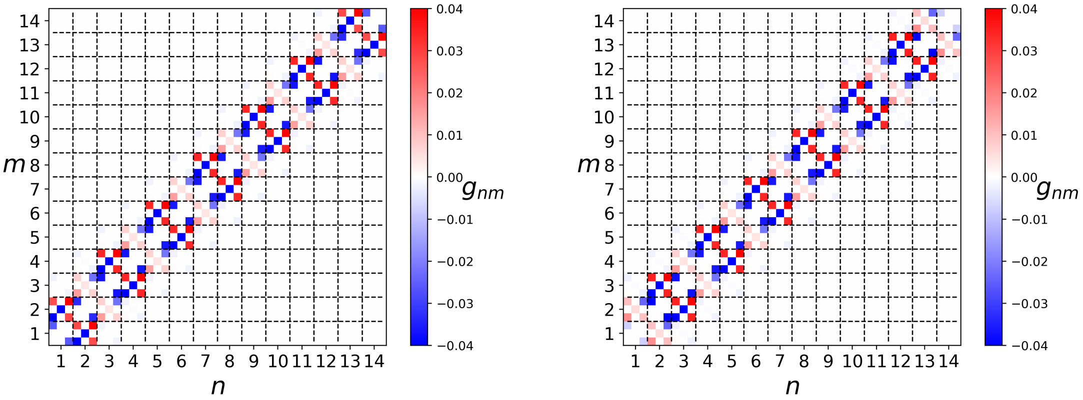

Figure 6.4: Elements of the interaction matrix g for trivial (left) and topological (right) configurations. We saturated the colors for a better visualization. The interactions for $|n - m| = 1$ are alternating between strong and weak. Here we fixed $N = 14, d = 2, \Delta = 1, a = 2d, \theta = \theta_m$, and $\phi = 0$.

The g matrix has $9N^2$ elements describing nine possible couplings between each pair of lattice sites in all directions, that is, for a given pair n and m there are 9 interactions to consider: xx, xy, yx, yy, and so on. We show in Fig. 6.4 the elements of the interaction matrix g in a grid. Each box shows the nine matrix elements of g_{nm}. In this figure, it is possible to see the staggered nature of the interactions between cells. The main difference between topological and trivial is whether the edges are weakly or strongly interacting with the bulk.

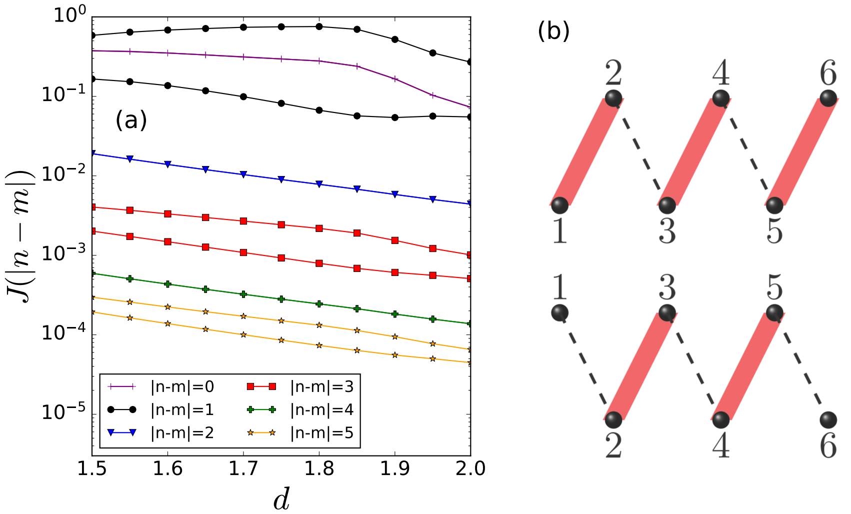

Figure 6.5: (a) Couplings between local phonons as a function of d for different pairs n, m for $N = 14, d = 2, \Delta = 1, a = 2d, \theta = \theta_m$, and $\phi = 0$ and (b) trivial and topological geometries where the lines depict the strong (red thick line) and weak (black dashed line) links (see text).

For visualization, we show in Fig. 6.5(c) the quantity $J(|n-m|) = \sum_{ij} g^{ij}_{nm}$ for distinct values of $|n-m|$ and d. The terms with odd $|n-m|$ describe the overall coupling between two different legs for two cases corresponding to the majority of weak or strong bonds between the sites. Such staggered nature can be directly associated with the SSH model. Even $|n-m|$ values provide the interactions along the same sublattice [see Fig. 6.5(d)] which do not vanish even at the magic angle θ_m due to displacements of atoms from equilibrium. As the trap separation d decreases, interactions in general become stronger. However, the intracell couplings feature a maximum near $d \approx 1.8$, which is related to the system geometry and coincides with the concavity change of the lowest band, indicating the presence of geometric frustration.

We have so far demonstrated that phonons in Rydberg atom arrays are capable of simulating complex solid state systems with highly tunable band structure. Extension to a two-dimensional setup would enable the occurrence of chiral edge states. Implementation of driving into the system with lasers can induce additional nonequilibrium dynamics [51].

6.1.4 The atom-phonon Hamiltonian

The atom-phonon Hamiltonian comes from the general electron-phonon Hamiltonian obtained in Chapter 3. It is written in terms of a overlap integral for which we evaluate in terms of the Wannier functions within some approximations. First, consider the potential is independent of the spin, so $\sigma = \sigma'$ and then α is independent of the spin. Secondly, within the tight-binding approximation, terms $\mathbf{R} \neq \mathbf{R}'$ are vanishing. Thirdly, for our neutral atom system, we restrict to the lowest Bloch band and tight-binding approximation as well. Lastly,

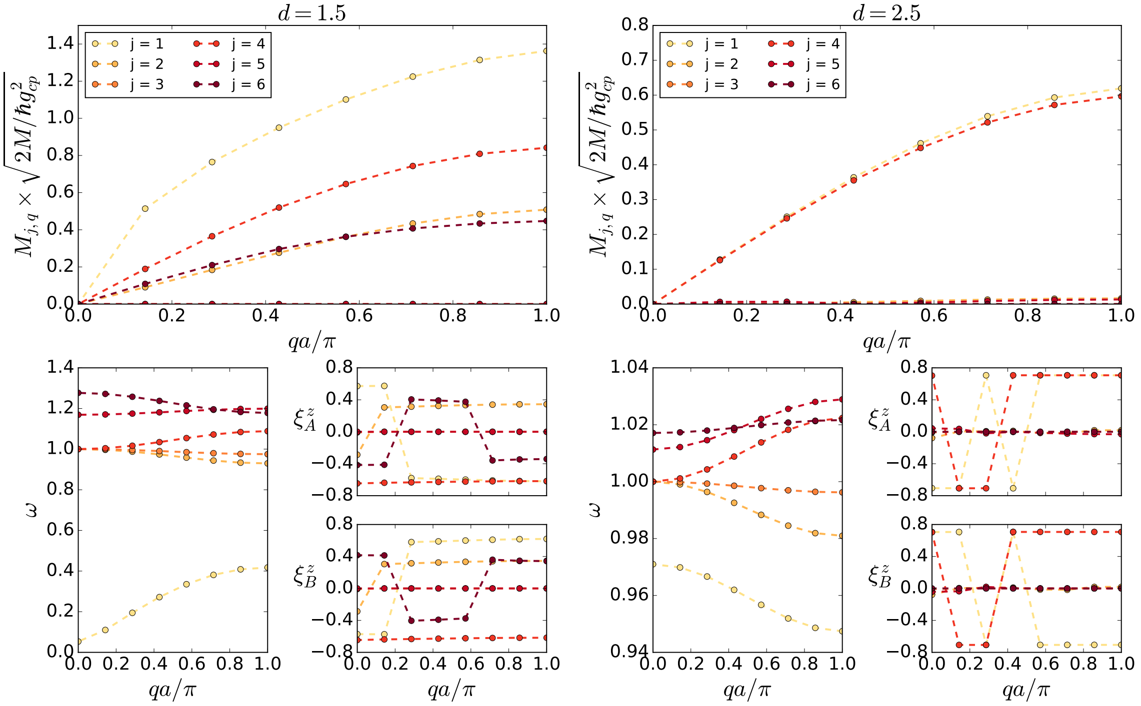

Figure 6.6: Interaction strength $M_{j,q}$ for $d = 1.5$ and $d = 2.5$. We show two examples where there is a clear distinction between multi-band and two-band regimes. The corresponding phonon spectra and eigenvector component in z direction are shown in the bottom panels. Here $N = 14, \Delta = 1, a = 2d, \theta = \theta_m, \phi = 0$.

in a zig-zag chain where $\mathbf{q} = q\hat{\mathbf{z}}$, the dot product in $M_{j\mathbf{q}}$ restricts the couplings and, as a result, transverse states without a z component do not interact with the atoms. The neutral atom-phonon Hamiltonian becomes

$$\mathcal{H}_{\text{a-ph}} = \sum_{q,k,j,\sigma} \frac{1}{\sqrt{N}} M_{j,q}(b_{j,q} + b_{j,-q}^{\dagger}) c_{k+q,\sigma}^{\dagger} c_{k,\sigma}, \tag{6.4}$$

with

$$M_{jq} = \sum_{\alpha} \sqrt{\frac{\hbar g_{cp}^2}{2M\omega_{jq}}} q \xi_{\alpha,z}^{(j)}(q) e^{-iq\rho_{\alpha}^{z}} \rho_0(q), \tag{6.5}$$

where a Fermi pseudopotential with magnitude g_{cp} was taken into account for V_q. Here we used Ortner *et al.* approximation for the lattice Wannier functions [108], which for composite lattices may need to be modified [89, 54, 101] but does not qualitatively impact our results. Thus,

$$\rho_0(q) = \int d\mathbf{r} e^{iqz} |\phi_0(\mathbf{r})|^2 \approx \frac{8\pi^2 \sin(qd/2)}{4\pi^2 qd - q^3 d^3}, \tag{6.6}$$

Therefore, we aim to study the interactions described by

$$\sqrt{\frac{2M}{\hbar g_{cp}^2}} M_{jq} = \frac{q\rho_0(q)}{\sqrt{\omega_{jq}}} \sum_{\alpha} |\xi_{\alpha,z}^{(j)}(q)| e^{-iq\rho_{\alpha}^{z}}. \tag{6.7}$$

The interaction strength inversely depends on the eigenvalues ω_j and directly depends on the z component of the eigenvectors $\xi_{\alpha,z}^{(j)}$, while ρ_0 and $e^{-iq\rho_\alpha^z}$ will just shape the interaction pattern. In other words, to understand the interaction behavior, one needs both ω_j and $\xi_{\alpha,z}^{(j)}$. If we change $\xi_{\alpha,z}^{(j)} \to -\xi_{\alpha,z}^{(j)}$ (for all j), the orthonormality condition still holds. That is why there is a modulus in Eq. 6.7.

In Fig. 6.6 we show two exemplary situations in which the coupling term crosses over from a two-band to multi-band structure. Its overall magnitude can be easily controlled independently by manipulating the Rydberg-atom interaction strength. For a better understanding, we show in the bottom panels of Fig. 6.6 the phonon spectrum and the z component of the corresponding states. As we can see, when d is big compared with the other lengths, only the first and 4th band are generating noticeable oscillations in z–direction. Decreasing the distance between the Rydberg atoms, other bands also acquire vibrational components along the z axis. This is the limitation of the quasi-1D platform as only longitudinal phonons can contribute. In addition, the atom-phonon coupling to the first phonon band shows a non-monotonic behavior with d due to the change in the band shape. As we can see in Fig. 6.7, from $d = 1.5$ to 1.65 the band is flattening, which increases the interaction strength due to the phonon energy being in the denominator. After the concavity changing transition, the band starts to widen and increase in amplitude again.

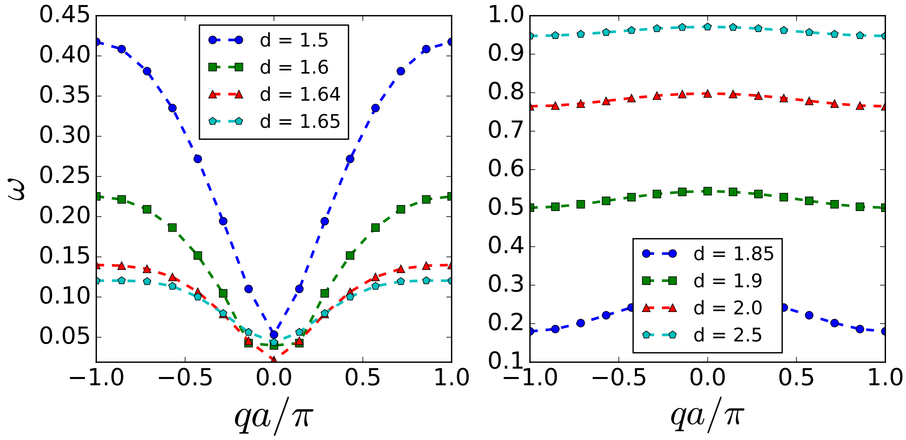

Figure 6.7: Phonon spectrum of the first band and for many values of d. In the left panel, the phonon frequency is decreasing with an increasing d, while in the right panel it is the opposite case. Here $N = 14, \Delta = 1, a = 2d, \theta = \theta_m$, and $\phi = 0$.

6.1.5 Discussion

To obtain the full Hamiltonian we proceed to adding the second subsystem composed of ground state atoms. Their van der Waals interaction with the Rydberg atoms can be described by a Fermi pseudopotential with tunable magnitude g_{cp}, omitting off-diagonal terms which are small due to low dipole moment of the ground electronic state [145, 141]. $V_{\text{Ry-a}}(\mathbf{r}_n - \mathbf{R}_{m\alpha})$ and $V_{\text{Ry-Ry}}(\mathbf{R}_{n\alpha} - \mathbf{R}_{m\beta})$ can be expanded in power series in Rydberg displacements u, providing the periodic potential for the atoms. Within the tight-binding approximation, the bare atomic Hamiltonian without phonons is described by the Hubbard model.

The whole system is described by an extended Hubbard-Holstein model

$$\begin{aligned}\mathcal{H}_{\mathrm{EHH}} = & -t \sum_{\langle n,m\rangle\sigma} (c^{\dagger}_{n\sigma}c_{m\sigma} + \mathrm{H.c.}) + U\sum_{m} n_{m\uparrow}n_{m\downarrow} + \sum_{j,q} \hbar\omega_{j,q} b^{\dagger}_{j,q}b_{j,q} \\ & + \sum_{q,k,j,\sigma} \frac{1}{\sqrt{N}} M_{j,q}(b_{j,q} + b^{\dagger}_{j,-q})c^{\dagger}_{k+q,\sigma}c_{k,\sigma},\end{aligned} \tag{6.8}$$

with nontrivial phonon structure including the possibility for topological bands and nonlocal couplings. The summations in n and m relate to the site index while in j accounts for the phonon bands. Phonon-induced interactions can induce long-range attraction between the fermions and enhance the formation of pairs and conductivity. While one can study the limiting cases of weak or very strong coupling analytically, e.g. by means of a generalized Lang-Firsov transformation [81, 63, 108, 150], we stress that due to the competition of terms the problem calls for a thorough numerical study in order to verify and interpret the quantum simulator output.

We observe that the interaction strength is highly dependent on the phonon energy and structure. Indeed, the other functions appearing in Eq. 6.5 will mostly affect the overall strength the coupling profile. In order to design the desired interaction between ground state atoms and phonons one thus needs to focus on the phonon part. The proposed Rydberg lattice setup turns to be perfect for such situation since it is a rich and highly controllable platform as discussed earlier.

6.1.6 Experimental feasibility and simulation prospects

We now argue that each quantity in (6.8) can be tuned with some degree of independence and can reach several kHz, providing sufficiently fast dynamics to operate within the Rydberg atom lifetime. Let us first discuss the parameter values achievable in current experiments. For simplicity, here we work with a quasi-one-dimensional chain with linear configuration of Rydberg atoms of equidistant separation d. The van der Waals C_6 coefficient between the ground state and Rydberg atom grows with the principal quantum number as $\sim n^5$ [57], in contrast to n^{11} scaling for both atoms excited [1]. Still, this leads to the characteristic range of the potential $R_6 = (2\mu C_6/\hbar^2)^{1/4}$ [23] being widely tunable. Assuming Rb*-Li pair one obtains $R_6 \approx 300$nm already for $n \sim 50$, meaning that interactions within the lattice are strong.

One can then proceed with estimation of the extended Hubbard-Holstein Hamiltonian parameters. Assuming tight-binding approximation, we obtain the tunneling coefficient [108] $t \approx 4E_r^2 d/\pi^2 g_{cp}$ where $E_r = \frac{\pi^2\hbar^2}{2md^2}$ and m is the atomic mass. Note that in order to make t appropriately large, using light atoms such as lithium seems to be the most convenient option. Meanwhile, $M_{\mathrm{a-ph}} \propto \sqrt{\frac{\hbar g_{cp}^2}{2M\omega}}$ with M being the mass of the Rydberg atoms. Even though the coupling term $\propto g_{cp}$ while $t \propto 1/g_{cp}$, tuning the spacing and tweezers trap frequency allows for manipulating the parameters independently. The Hubbard U term is independently tunable using a magnetic Feshbach resonance [23]. Assuming $d \sim 1\mu$m and $g_{cp} \sim 10^4$Hz, we obtain $M_{\mathrm{a-ph}}$ in the same range and $t \approx 3$kHz, comparable to other energy scales. For high enough

n all parameters will exceed the Rydberg level decay rate Γ, as highly excited states can reach lifetimes of the order of a millisecond.

A reliable quantum simulator requires initializing the system with high fidelity. This may require some optimization steps. For instance, direct excitation of a chain of atoms trapped in tweezers to a Rydberg state at small separation is a nontrivial task due to the Rydberg blockade phenomenon [13]. In order to circumvent it, one can either utilize optimal control protocols [99, 92], or excite the atoms further away from each other and then bring them to the designated positions. For alkali atoms, this protocol can be challenging [9], but alkaline earth-based setups [148] can offer an advantage here. Similarly, loading the lattice efficiently is desired due to the finite lifetime of the system. Here we would suggest to prepare the ground state atoms in a separate set of optical tweezers and subsequently release them into the lattice. Experimentally, the system provides a number of possible measurements such as time-of-flight and *in situ* imaging of atoms, as well as phonon state tomography of the chain. Studying the dynamics after a quench or under driving should does not impose any additional challenge.

We also notice that a class of extended Hubbard-Holstein models could also be studied with a possibly simpler system in the spirit of variational quantum simulation [78, 97]. In this scenario one would use an ansatz for the phonon part in order to calculate the effective fermionic Hamiltonian classically, and then find the ground state of the reduced system by implementing it in experiment and obtaining a new candidate phonon state for the next iteration.

6.2 Hybrid numerical approach for el-ph systems

In the first part of this chapter, we show that extended-Hubbard-Holstein (EHH) models can be quantum simulated with Rydberg atoms coupled to neutral atoms. We showed that in such platform the electron-phonon coupling strength may strongly depend on the phonon dispersion characteristics of the Rydberg atom chain. We now turn to the numerical analysis of electron-phonon models through the hybrid method described in chapter 5. Before studying such complex scenario, we need to first understand how the method is applied to the basic one-dimensional Hubbard-Holstein model. In the following, we give a short analysis of this model, obtaining results that agree well with the literature.

6.2.1 General setup

Let us consider the Hubbard-Holstein model in one-dimension which assumes on-site electron-electron and electron-phonon couplings, where the phonons are assumed as dispersionless lattice vibration modes,

$$H = -t \sum_{\langle i,j\rangle\sigma} (c_{i\sigma}^{\dagger} c_{j\sigma} + H.c.) + U \sum_i n_{i\uparrow} n_{i\downarrow} + \frac{\omega}{2} \sum_i (x_i^2 + p_i^2) + g' \sum_i n_{i\sigma} x_i. \tag{6.9}$$

where $n_{i\sigma} = c_{i\sigma}^{\dagger} c_{i\sigma}$. The non-Gaussian state ansatz is given by

$$|\Psi\rangle = U_{\lambda}(|\psi_{\rm ph}\rangle \otimes |\psi_{\rm el}\rangle), \tag{6.10}$$

where $|\psi_{\rm el}\rangle$ is the many-body state of the electrons, $|\psi_{\rm ph}\rangle = U_{GS}\,|{\rm vac}\rangle$, and

$$U_\lambda = \exp\left\{ i\frac{g'}{\omega}\sum_{i,j,\sigma} n_{i\sigma}\lambda_{ij}p_j \right\}. \tag{6.11}$$

The effective electronic Hamiltonian obtained from $H_{\rm eff} = \langle\psi_{\rm ph}|\, U_\lambda^\dagger H U_\lambda\, |\psi_{\rm ph}\rangle$ reads

$$H_{\rm eff} = -\sum_{\langle i,j\rangle\sigma}[t^{ij}_{\rm eff}c^\dagger_{i\sigma}c_{j\sigma} + H.c.] + \frac{\omega}{4}{\rm Tr}\{\Gamma\} + \frac{\omega}{2}\Delta_R^T\Delta_R - \sum_{i\sigma}\mu^i_{\rm eff}n_{i\sigma} + \sum_{i,j,\sigma,\sigma'}V^{ij}_{\rm eff}n_{i\sigma}n_{j\sigma'}, \tag{6.12}$$

where we defined the effective chemical potential

$$\mu^i_{\rm eff} = g'\sum_j(\lambda_{ij}-\delta_{ij})\Delta^j_x + \frac{U}{2}, \tag{6.13}$$

the effective spin-spin interaction strength

$$V^{ij}_{\rm eff} = \frac{g'^2}{2\omega}\left[\sum_n \lambda_{in}\lambda_{jn} - 2\lambda_{ij} + \frac{\omega U}{g'^2}\delta_{ij}\right], \tag{6.14}$$

and the effective hopping strength

$$t^{ij}_{\rm eff} = t\exp\left\{\frac{-ig'}{\omega}(\Delta_R^T\mathcal{W})_{ij}\right\}\exp\left\{-\left(\frac{g'}{2\omega}\right)^2(\mathcal{W}^T\Gamma\mathcal{W})_{ij}\right\}, \tag{6.15}$$

with

$$(\mathcal{W}^T\Gamma\mathcal{W})_{ij} = \sum_{kml} w_{ijk}S^{px}_{km}S^{px}_{lm}w_{ijl} + \sum_{kml} w_{ijk}S^{pp}_{km}S^{pp}_{lm}w_{ijl}, \tag{6.16}$$

and similarly for $(\Delta_R^T\mathcal{W})_{ij}$, where $w_{ijk} = \lambda_{ik} - \lambda_{jk}$ and $\Gamma = SS^T$.

6.2.2 Homogeneous parametrization

Considering a homogeneous parametrization, such that Δ_x, Δ_p, Γ, and λ are defined by a single parameter each, we can greatly simplify not only the effective Hamiltonian, but also the variational optimization. Note that $\Gamma = SS^T$ with $S = e^{\sigma\xi}$, so the symmetric matrix ξ is defined such that it only has anti-diagonal elements (all equals to the scalar ξ). In this scenario, the effective electronic Hamiltonian becomes a shifted/distorted Hubbard-Holstein model, it reads

$$H_{\rm eff} = -t_{\rm eff}\sum_{\langle i,j\rangle\sigma}(c^\dagger_{i\sigma}c_{j\sigma} + H.c.) + U_{\rm eff}\sum_i n_{i\uparrow}n_{i\downarrow} + \frac{\omega}{2}(\Delta_x^2+\Delta_p^2)N + \frac{\omega}{2}\cosh(2\xi) - \mu_{\rm eff}\sum_{i\sigma}n_{i\sigma}, \tag{6.17}$$

where we defined the effective hopping

$$t_{\rm eff} = t\exp\left\{-\left(\frac{g'\lambda}{2\omega}e^{-\xi}\right)^2\right\}, \tag{6.18}$$

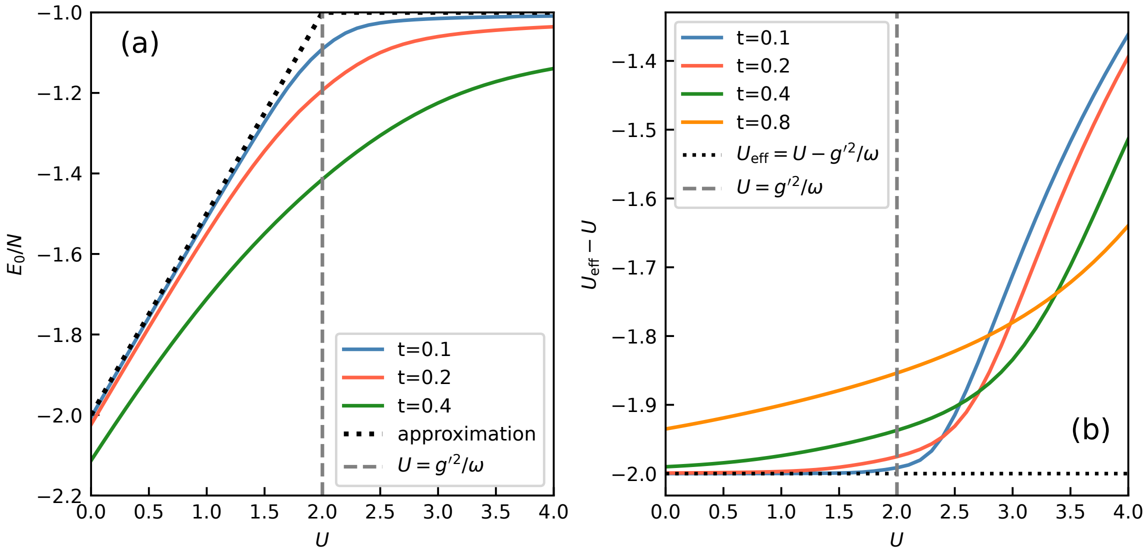

Figure 6.8: (a) Average energy and (b) Effective electron-electron interaction as a function of the Hubbard interaction for distinct t with fixed $g = 1.0$ and $N = 6$.

the effective chemical potential,

$$\mu_{\text{eff}} = g'(\lambda - 1)\Delta_x - \frac{g'^2}{2\omega}\lambda(\lambda - 2), \tag{6.19}$$

and the effective on-site electron-electron (Hubbard) interaction

$$U_{\text{eff}} = \left(U - \frac{g'^2}{\omega}\right) + \frac{g'^2}{\omega}(\lambda - 1)^2. \tag{6.20}$$

As one can see, the presence of electron-phonon interactions renormalizes the hopping, creating a smaller effective hopping. The two competing interactions, electron-electron and electron-phonon, generates an effective electron-electron interaction that can be either repulsive ($U_{\text{eff}} > 0$) or attractive ($U_{\text{eff}} < 0$) depending on g'^2/ω, U, and λ. In the rotated Hamiltonian, obtained from the canonical Lang-Firsov transformation ($\lambda = 1$), the effective Hubbard interaction is $\tilde{U} = U - g'^2/\omega$. In the anti-adiabatic limit, $\tilde{U} = 0$ is the transition point from two regions that are known to correspond to charge-density wave (CDW) and spin-density wave (SDW) phases, which we will characterize below. Additionally, an effective chemical potential takes place.

We begin the numerical analysis calculating the ground state energy as a function of the Hubbard interaction U and distinct hopping strengths $t = 0.1, 0.2, 0.4$ for $g = 1.0$ [see Fig. 6.8]. We observe that close to the anti-adiabatic regime, $t = 0.1\omega$, the average energy, defined as $E_0 = (\mathcal{E}_{\min} - \omega/2)/N$, is well approximated by $E_0 = U/2 - g'^2/\omega$ if $U < g'^2/\omega$ and $E_0 = -g'^2/2\omega$ otherwise, when U is away from g'^2/ω, deep in the CDW/SDW phases. We show in Fig. 6.8 that the effective electron-electron interaction is well approximated by $U_{\text{eff}} \approx \tilde{U}$ when $U < g'^2/\omega$, and the CDW-SDW phase boundaries are easy to define. We set $t = 0.2\omega$ from now on, since in the low-frequency regime $\omega < t$ the phase boundaries are not easy to define and the numerical calculations are reportedly hard to converge [138].

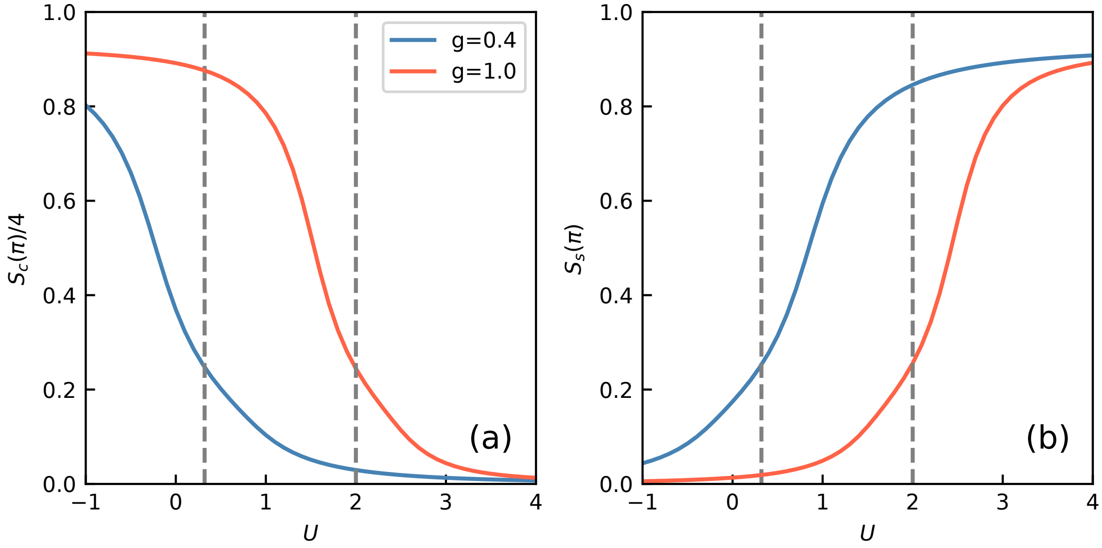

Figure 6.9: Charge and spin structure factors at $q = \pi$ for $g = 0.4$ and 1.0 with $N = 10$ and $t = 0.2$ as a function of the Hubbard repulsion.

6.2.3 Charge- and spin- density wave phases

A large U tends to localize electrons and, at half-filling, favors magnetic (typically antiferromagnetic) correlations. In one-dimensional systems, these magnetic correlations are often described in terms of a spin density wave (SDW), because of the Mermin–Wagner theorem, long-range magnetic order is strictly absent at finite temperature in 1D. What one finds instead are quasi-long-range spin correlations with a characteristic wave vector ($q = \pi$), hence the term spin density wave. This description emphasizes the spatial modulation of the spin correlations. Essentially, SDW and AFM describe the same underlying physics, because the dominant spin correlations are antiferromagnetic in nature. The Holstein part of the model couples the electrons to local lattice distortions (phonons). A sufficiently strong electron–phonon coupling can lead to an effective attraction between electrons. This effective attraction may result in the formation of charge order, such as a charge density wave (CDW), where the electronic density modulates periodically. The competition between these two phases is often characterized by the sign of the effective interaction parameter U_{eff}. If U_{eff} becomes negative, the system tends to favor CDW order, while a positive U_{eff} supports magnetic (SDW/AFM) correlations. U_{eff} is a function of λ which varies with U, but for a small t, as described above, it is well approximated by $U_{\text{eff}} \approx \tilde{U}$ for $U < g'^2/\omega$, since λ approaches unity.

To characterize the aforementioned phases, we compute the corresponding charge and spin structure factors. These structure factors provide quantitative measures of how correlations decay in space and help distinguish between the competing phases in the model. The charge structure factor $S_c(q)$, is the Fourier transform of the charge-charge correlation function that measures how the electron density at one site is correlated with that at another. It reads

$$S_c(q) = \frac{1}{N} \sum_{ij} e^{-iq(i-j)} \langle n_i n_j \rangle. \tag{6.21}$$

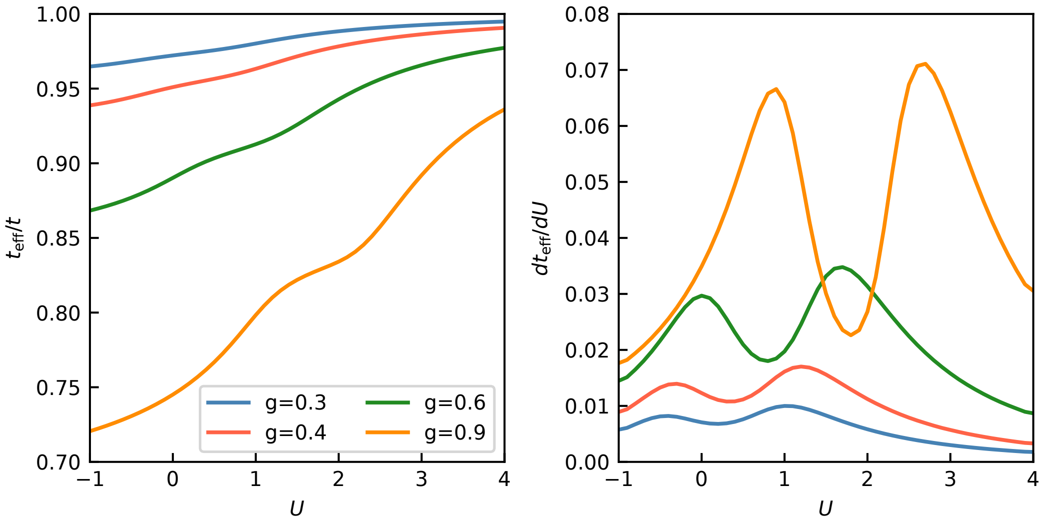

Figure 6.10: Effective hopping integral t_{eff} and its derivative in terms of t for various U and g. t_{eff} approaches t for a increasing U. Parameters: $t = 0.2$ and $N = 6$.

A pronounced peak at $q = \pi$ indicates the presence of charge ordering, supporting a CDW phase. Similarly, the spin structure factor $S_s(q)$ is obtained from the spin–spin correlation function. It is given by

$$S_s(q) = \frac{1}{N} \sum_{ij} e^{-iq(i-j)} \langle S_i^z S_j^z \rangle \tag{6.22}$$

where the spin operator is defined as $S_i^z = \frac{1}{2}(n_{i\uparrow} - n_{i\downarrow})$. A dominant peak at $q = \pi$ signals strong antiferromagnetic correlations, typical of the SDW (or AFM) phase.

We show in Fig. 6.9 the structure factors at $q = \pi$ as a function of U. For an interaction $U < g'^2/\omega$ the charge (spin) structure factor tends to a large (vanishing) value characteristic of the CDW phase. On the other hand, for a large U, the charge (spin) structure factor tends to a vanishing (large) value, as expected by the SDW phase. However, close to the transition $U_{\text{eff}} \approx \tilde{U}$, the structure factors do not sharply change but instead show distinct features. This is related to an intermediate phase that exists in the CDW-SDW crossover region.

6.2.4 Possibility of a metallic phase in the crossover region

In addition to the phases of small and large Hubbard repulsion, a phase between the two regimes arises away from the anti-adiabatic limit. A transient change of behavior is pronounced in the effective hopping strength, which is transmitted to the relevant observables. We see in Eq. 6.15 that $t_{\text{eff}}/t \leq 1$, since g, λ, and ξ are positive. From a tight-binding limit point of view, the effective mass is inversely proportional to the effective hopping. That way, a small t_{eff} relates to a large effective mass of polarons, which suggests an immobile bipolaron state or CDW. We show in Fig. 6.10 that the effective hopping t_{eff} is indeed much smaller than t specially for $U < g'^2/\omega$ and we only reach $t_{\text{eff}} = t$ for a large U. Around the CDW-SDW crossover region, we observe kinks in t_{eff} which can be better seen from its

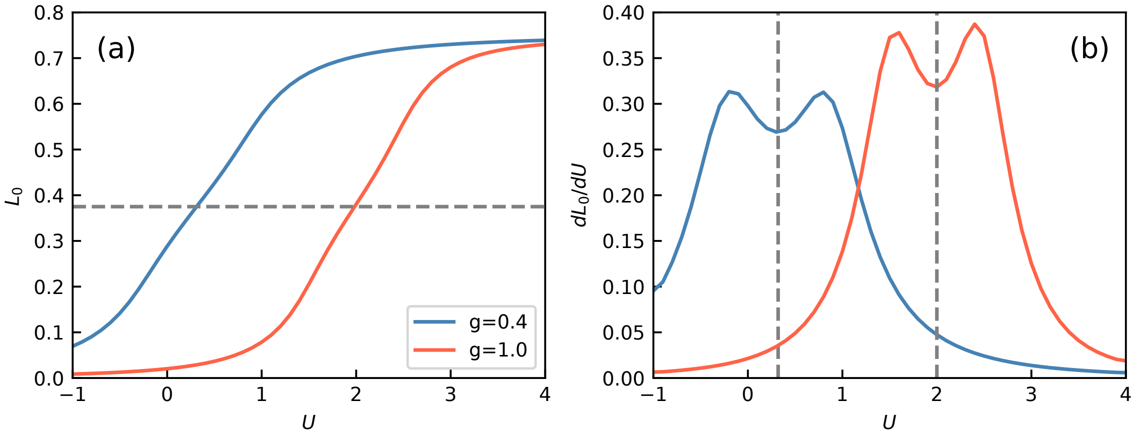

Figure 6.11: Local moment and its derivative versus U for a fixed $N = 10$ and $t = 0.2$ with $g = 0.4$ and $g = 1.0$. Around the U corresponding to $L_0 = 3/8$, we observe a distinct behavior that indicates the existence of a possible intermediate phase.

derivative. We show that $\mathrm{d}t_{\text{eff}}/\mathrm{d}U$ peaks in the two sides of the crossover region, indicating a possible intermediate phase. This indication becomes less and less visible for a decreasing g, as shown in Fig. 6.10.

Several authors have indicated that such intermediate phase is a metallic phase [132, 80, 40]. In a metallic phase, the local moment operator, defined as

$$L_0 = \frac{1}{N}\sum_i \langle \mathbf{S}_i^2 \rangle = \frac{3}{4} - \frac{3}{2N}\sum_i \langle n_{i\uparrow} n_{i\downarrow} \rangle, \tag{6.23}$$

should equal 3/8 as in the non-interacting electron gas. We observe in Fig. 6.11 that this value is achieved at $U \approx g'^2/\omega$. The derivative of L_0 shows a similar behavior compared to t_{eff}: the kinks around $U = g'^2/\omega$ reflects an intermediate region where $L_0 \approx 3/8$ and its first derivative with respect to U shows a deceleration around $U = g'^2/\omega$ that increases for an increasing g (or N). While this is useful to have some initial insights, the characterization of this intermediate phase requires extra effort. For example, in Ref. [138] the authors calculate multiple observables in the 2D EHH model to show that this phase is way more involved.

In the first section we have shown a promising platform for quantum simulation in which the coupling strength strongly depends on the phononic characteristics of the Rydberg atom lattice. It shows us that one can obtain some even more interesting interactions by tuning the atomic system into more complex phonon behavior. In the last section, we turn to the numerical analysis of a simpler model, not only showing the capabilities of the numerical method but also benchmarking it against the literature. The clear next step is to, in parallel, develop realistic quantum simulation setups with complex phonon structure and to extended the numerical calculations to the full ansatz given by Eq. 6.10 to work for any EHH model of the form of Eq. 6.8. This study is still an on-going project, and thus is not shown in this thesis.

7

Cavity QED with strongly interacting emitters

We consider a chain of N possibly interacting two-level systems embedded in a single-mode cavity field [see Fig. 7.1]. In principle, there are multiple possible sources of loss causing dissipation, but we focus on the regime where light-matter coupling is strong enough and dominates. The two-level system can be experimentally implemented in multiple ways beyond the classical examples of ions or electrons, namely superconducting circuits [29], color centers [152], trapped ions [122], quantum dots [88], ultracold atoms [10, 119, 28, 110], and even organic molecules [43]. Throughout this work, we represent the two-level systems as 1/2 spins. In principle, the $s = 1/2$ spins could be arranged in arbitrary geometry and connectivity. The spins couple to the photons via the standard minimal coupling scheme. Additionally, short-range interactions between emitters induce Heisenberg-like spin-spin interactions in the effective description. The Hamiltonian is then composed of the sum of the free Hamiltonians of the cavity and of the spins, and the interacting spin-photon and spin-spin Hamiltonians as

$$\begin{aligned} H &= H_0^{\text{cavity}} + H_0^{\text{spin}} + H_I^{\text{spin-photon}} + H_I^{\text{spin-spin}} \\ &= H^{\text{Dicke}} + H^{\text{XYZ}}, \end{aligned} \tag{7.1}$$

where, in the absence of spin-spin interactions, the system is governed by the Dicke Hamiltonian given by

$$\begin{aligned} H^{\text{Dicke}} &= \omega\left(a^\dagger a + \frac{1}{2}\right) + \frac{\varepsilon}{2}\sum_{i=1}^{N}\sigma_i^z + \frac{g}{\sqrt{N}}\sum_{i=1}^{N}\sigma_i^x(a + a^\dagger) \\ &\equiv \frac{\omega}{2}(x^2 + p^2) + \varepsilon s^z + g' s^x x. \end{aligned} \tag{7.2}$$

In this setup, each two-level qubit is represented by a local spin operator $s_n^\alpha = \sigma_n^\alpha/2$, while the photonic operators are given by $x = (a^\dagger + a)/\sqrt{2}$ and $p = i(a^\dagger - a)/\sqrt{2}$, with a and $a^\dagger$ denoting the photon annihilation and creation operators, respectively. Here, ω designates the cavity frequency and ε the atomic transition frequency, both set as $\omega = \varepsilon = 1$. Moreover, g represents the collective coupling strength, and $g' = 2g/\sqrt{N/2}$ accounts for the mode volume, with N the number of emitters. In the Dicke model, the spin interactions are absent, and the spin-photon interaction is site-independent, the spatial coordinates are irrelevant and one

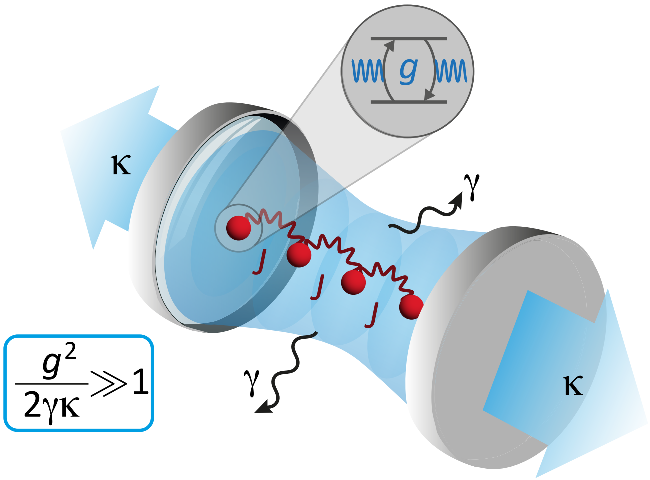

Figure 7.1: Sketch of the considered model. The system is composed of an ensemble of two-level quantum systems (TLSs) in an optical cavity. They can anisotropically interact with their nearest-neighbors with an exchange rate $\mathbf{J} = (J_x, J_y, J_z)$. The cavity can exhibit photon loss with a rate κ. The TLSs can also spontaneously decay, causing dissipation at a rate γ. Each TLS has a separation ε between the two states and is interacting with the cavity field with a interaction strength g. Although all these processes are present, the condition $g^2/2\gamma\kappa \gg 1$ guarantees that the dissipation happens at a much slower rate compared to the light-matter interaction.

can define a collective spin operator $s^\alpha = \sum_j s_j^\alpha$. Additionally, the Hamiltonian commutes with the total spin $s^2 = (s^x)^2 + (s^y)^2 + (s^z)^2$, meaning that one can greatly reduce the number of states involved. The Hilbert space in this case is spanned by a collective spin $\{|j, m\rangle, m = -j, -j+1, \cdots, j-1, j\}$, with $j = N/2$, such that there are only $N+1$ atomic degrees of freedom instead of 2^N. The spin-spin interaction breaks this symmetry and prevents using the collective spin approach. In this work, short-range Coulomb interactions between atoms are not neglected in the second quantization, leading to nearest-neighbor Heisenberg-type spin-spin interactions, which are unavoidable in reality. This generalization can be described by the addition of the spin-spin interaction term H^{XYZ}. In the homogeneous scenario and considering nearest-neighbor interactions, this term is described by the Heisenberg Hamiltonian, which reads

$$H^{\mathrm{XYZ}} = -\sum_{\langle i,j\rangle} \sum_{\alpha=x,y,z} J_\alpha s_i^{(\alpha)} \cdot s_j^{(\alpha)}, \tag{7.3}$$

where $\langle i, j\rangle$ depicts nearest-neighbor sites i and j. It contains a family of models depending on the choice of the exchange parameters J_x, J_y, and J_z. To study the effect of coupling spins to light, we focus on two particular examples: $J_x = J_y = 0$ and $J_z = 4J$, the Dicke-Ising model, and $J_x = J_y$ with varying J_z, which we call Dicke-XXZ model. We note that ε can also be interpreted as a classical longitudinal field which breaks the degeneracy between the spin projections.

While the large Hilbert space of the spin part can still be handled numerically truncating the maximum number of photons allowed $n_{\max}$ to a small number, with ED or DMRG, the photonic state in principle requires an infinite-dimensional wavefunction. Truncating this space to a finite number of Fock states cannot ensure convergent results and requires a more robust approach.

7.1 The Hybrid Numerical Method

We now turn to the description of the numerical approach used in this work. In short, we treat the photonic space variationally using a Gaussian state. Then, tracing out the photonic degrees of freedom leads to an effective spin Hamiltonian for which we obtain the ground state via DMRG. The procedure is repeated iteratively, minimizing the photonic variational parameters and updating the effective spin Hamiltonian at each step until convergence. We are going to split the analysis into two distinct ansätze: the Gaussian state (GS) and the non-Gaussian state (NGS) ansatz. We will scrutinize the method in these two scenarios in the following.

In the first scenario, we consider the wave function of the system to be separable. This simple assumption is justified by the known result for the Dicke model stating that in the strong coupling regime and in the thermodynamic limit the photonic subspace is well described by a coherent state [75]. In addition, coherent states and the semi-classical approximation are intertwined, since they can provide a quantum-classical connection. The semi-classical approximation is often used to describe the behavior of the field in the limit of *large photon numbers*. In this case, the coherent state becomes very close to a classical wave, and the behavior of the field can be approximated by classical wave equations. However, despite this similarity to classical waves, the coherent states still retain certain quantum features, such as the fluctuations in the number of photons and the Heisenberg uncertainty principle. A straightforward generalization is to use a GS. The Gaussian representation provides a robust framework for examining photonic states in systems where interactions are accurately approximated by quadratic Hamiltonians [conf. chapter 4], which is the case here in the weak-coupling limit. It is written as $|GS\rangle = U_{GS}|0\rangle$ where $|0\rangle$ is the photonic vacuum and [127]

$$U_{GS} = U_d U_S = \exp\big(i\boldsymbol{R}^T\boldsymbol{\sigma}\boldsymbol{\Delta}_R\big)\exp\bigg(-\frac{i}{2}\mathbf{R}^T\boldsymbol{\xi}\boldsymbol{R}\bigg), \tag{7.4}$$

with $\mathbf{R} = (x,p)^T$, $x = (a^\dagger + a)/\sqrt{2}$, and $p = i(a^\dagger - a)/\sqrt{2}$. This transformation comprises two unitary operators: the displacement operator U_d and the squeezing operator U_S, where $\boldsymbol{\Delta}_R = (\Delta_x, \Delta_p)^T$ denotes the photon displacement vector and $\boldsymbol{\xi}$ stands for the symmetric squeezing matrix. For simplicity, here we chose $\boldsymbol{\xi}$ to be a single parameter, anti-diagonal matrix, reflecting the symmetry of the spin-photon interaction. The vector $\mathbf{R}$ transforms as $U_{GS}^\dagger\mathbf{R}U_{GS} = \boldsymbol{S}\boldsymbol{R} + \boldsymbol{\Delta_R}$ with $\mathbf{S}$ being a symplectic matrix $\mathbf{S} = e^{\boldsymbol{\sigma}\boldsymbol{\xi}}$ and $\boldsymbol{S^T}\boldsymbol{\sigma}\boldsymbol{S} = \boldsymbol{\sigma}$.

As stated above, the Gaussian ansatz considers the spin and photonic degrees of freedom to be separable. Therefore, in strongly interacting systems, its effectiveness is naturally constrained since it fails to capture the complex correlations emerging from the interplay between bosonic and many-body degrees of freedom. For instance, explicit spin-photon couplings in hybrid quantum systems can generate entanglement that extends beyond the Gaussian regime. The NGS ansatz tackles this issue by merging Gaussian states with a dressing unitary transformation U_λ, which enables controlled entanglement between photonic and atomic elements, thereby offering a thorough characterization of hybrid quantum systems.

The NGS ansatz reads,

$$|\psi\rangle = U_\lambda\left(|GS\rangle \otimes |\phi\rangle\right), \tag{7.5}$$

with $|\phi\rangle$ being the spin state (for now unspecified) and where U_λ is given by

$$U_\lambda = \exp\left\{ i\frac{g'}{\omega}\sum_{i,j,\alpha} s_i^{(\alpha)}\lambda_{ij}^{(\alpha)}p_j \right\}. \tag{7.6}$$

This approach draws inspiration from the Lang-Firsov transformation [81], which is typically utilized in strong coupling perturbation theory to decouple interactions. U_λ extends this concept by incorporating adjustable parameters $\{\lambda\}$, allowing for a variational treatment of spin-photon coupling. This transformation offers partial decoupling of the spin-photon term. In the Dicke model, the kinetic part of the Hamiltonian is decoupled when $\lambda = 0$, while the potential part has no interaction when $\lambda = 1$ [see Eq. 7.7]. That way, λ is treated as a variational parameter in the range $[0, 1]$ on top of the previous set of GS parameters. Additionally, for a single-mode cavity with Dicke-like spin-photon couplings, $\lambda_{ij} = \delta_{ij}\hat{\mathbf{e}}_x\lambda$ is sufficient. The procedure to obtain the ground state is split in two steps, the minimization of the variational energy, given by $\mathcal{E}(\boldsymbol{\Delta}_R, \boldsymbol{\xi}, \lambda, |\phi\rangle) = \langle\psi| H |\psi\rangle$, and DMRG treatment of the effective spin Hamiltonian. That way, in the first step, we optimize $\{\boldsymbol{\Delta}_R, \boldsymbol{\xi}, \lambda\}$, where the spin averages and correlations are obtained from an initial random spin state $|\phi\rangle$. With this set of variational parameters we construct the effective spin Hamiltonian by tracing out the photonic degrees of freedom via $H_{\text{eff}} = \langle GS| U_\lambda^\dagger H U_\lambda |GS\rangle$. Explicitly, the effective spin Hamiltonian is given by

$$H_{\text{eff}} = H_{\text{eff}}^{\text{Dicke}} + H_{\text{eff}}^{\text{XYZ}}, \tag{7.7}$$

where

$$\begin{aligned} H_{\text{eff}}^{\text{Dicke}} &= \frac{\omega}{2}\cosh(2\xi) + \frac{\omega}{2}(\Delta_x^2 + \Delta_p^2) + (1-\lambda)g'\Delta_x s^x \\ &- (2-\lambda)\lambda\frac{g'^2}{2\omega}s^{x2} + \omega_0\left\{ s^z\cos\beta - s^y\sin\beta \right\}e^{-\alpha/2}. \end{aligned} \tag{7.8}$$

and

$$\begin{aligned} H_{\text{eff}}^{\text{XYZ}} = -\sum_i \Bigg\{ & J_x s_i^x s_{i+1}^x \\ & + s_i^y s_{i+1}^y e^{-\alpha}\left[J_y(\cosh\alpha\cos^2\beta + \sinh\alpha\sin^2\beta) + J_z(\cosh\alpha\sin^2\beta + \sinh\alpha\cos^2\beta) \right] \\ & + s_i^z s_{i+1}^z e^{-\alpha}\left[J_y(\cosh\alpha\sin^2\beta + \sinh\alpha\cos^2\beta) + J_z(\cosh\alpha\cos^2\beta + \sinh\alpha\sin^2\beta) \right] \\ & + (s_i^z s_{i+1}^y + s_i^y s_{i+1}^z)(J_y - J_z)e^{-2\alpha}\cos\beta\sin\beta \Bigg\}, \end{aligned} \tag{7.9}$$

with

$$\alpha = \frac{1}{2}\left(\frac{\lambda g'}{\omega}\right)^2 e^{-2\xi}, \tag{7.10}$$

$$\beta = \lambda g'\Delta_p/\omega. \tag{7.11}$$

This Hamiltonian can be minimized using a plethora of established numerical methods for spin systems since it does not contain the unbounded photonic Hilbert space anymore. Here, we proceed to obtain the ground state energy, and the necessary spin correlations from DMRG. The procedure is then repeated: we insert the $|\phi\rangle_i$ state back into the full Hamiltonian in order to optimize $\{\boldsymbol{\Delta}_R, \boldsymbol{\xi}, \lambda\}_{i+1}$ and continue the process until convergence. The workflow diagram of the hybrid method, which we call NGS-DMRG for short, is shown in Fig. 7.2.

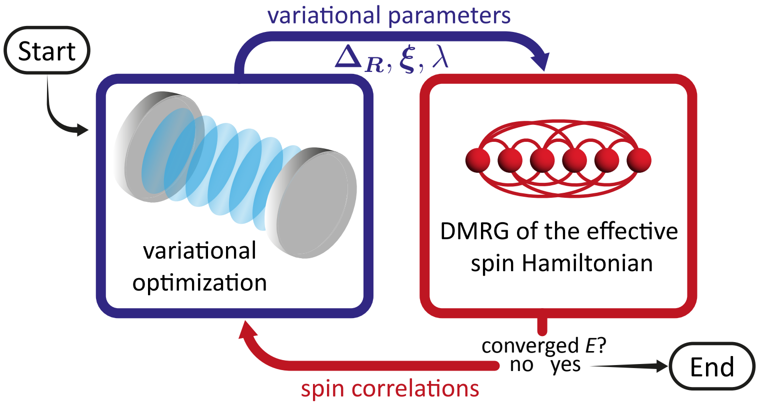

Figure 7.2: Flow diagram of the hybrid numerical method. Starting with a initial guess we minimize the variational energy, obtaining the optimal variational parameters. We then plug them into the effective spin Hamiltonian which is solved via DMRG giving the spin averages and correlations. The workflow is repeated until convergence of the energy, reaching a good approximation of the true ground state energy.

7.1.1 Benchmarking: The Dicke model

To illustrate the simplest case, consider when the interactions vanish, *i.e.*, $J_x = J_y = J_z = 0$. In this scenario, the system reduces to the Dicke model, as previously discussed. This model is renowned for its superradiant phase transition in the thermodynamic limit [see Fig. 7.3(a)].

We first consider the GS ansatz ($\lambda = 0$). In this case, the minimization can be performed analytically under the following assumptions. With no spin-spin interactions, all spins are equivalent under permutation and only the total spin couples to the photon mode. Therefore, we rewrite the many-body state vector as a coherent state represented by [8],

$$|\phi\rangle = e^{-i\phi \sum_j s_j^y} |\downarrow\downarrow \cdots\rangle \equiv e^{-i\phi s^y} |j, -j\rangle\,, \tag{7.12}$$

where ϕ is treated as another variational parameter describing the orientation of the total spin and $j = N/2$. We then minimize the expectation value of energy under the wavefunction ansatz. In this approach, we obtain $\boldsymbol{\Delta}_R = (-g'\langle s^x\rangle/\omega, 0)$ and $\xi = 0$, with $\phi = \cos^{-1}((g_c/g)^2)$ for $g > g_c$ and $\phi = 0$ for $g < g_c$, as a solution of the imaginary-time evolution equations, with $g_c = \sqrt{\omega\varepsilon}/2$. Thus, the cavity field is in the vacuum state and spins are ferromagnetic for $g < g_c$ until it goes to a coherent state of both photons and spins. Therefore, the average

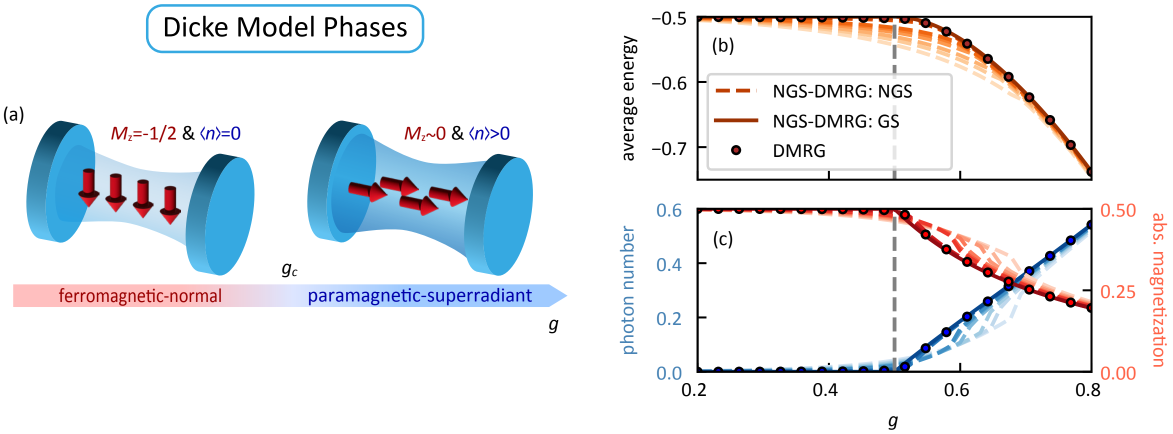

Figure 7.3: The Dicke model and its quantum phases. (a) The system consists of a spin chain coupled to a quantum light field within an optical cavity. The atom-cavity coupling parameter g controls the quantum phases of the composite system. For $g < g_c$, the spins form a ferromagnetic configuration, and the photonic field has a vanishing mean photon number. As g increases, the system undergoes a second-order phase transition to the superradiant phase at $g = g_c$. This phase is characterized by a significantly large mean photon number and a paramagnetic spin order that goes towards a full alignment in x. This result is depicted by (b) the ground state energy, (c) absolute magnetization in the z direction (red), and mean photon number (blue) as a function of g. Solid lines are the result for the NGS-DMRG method in the Gaussian ansatz (N-independent), dashed lines are the result for the NGS-DMRG method in the non-Gaussian ansatz for several $N = 4, 5, 6, 8, 10, 12, 40, 100$ (from light to dark colors), and dots are pure DMRG results for $N = 100$ and $n_{\max} = 120$.

energy obtained is

$$E_0 = \frac{1}{N}\left(\mathcal{E}_{\min} - \frac{\omega}{2}\right) = \begin{cases} -\varepsilon/2, & g \leq g_c, \\ -(g^4 + g_c^4)/\omega g^2, & g \geq g_c, \end{cases} \tag{7.13}$$

where g_c is the critical coupling indicating a second-order phase transition [see Fig. 7.3(b)]. The two phases separated by g_c can be characterized by the magnetization along the z axis, i.e., $M_z = \langle s^z \rangle / N$, and the average photon number, $\langle n \rangle / N$. As shown in Fig. 7.3(c), we find the magnetization plateau at $M_z = -1/2$, when $g < g_c$, indicating a ferromagnetic order with all spins pointing down. As g increases beyond g_c, the magnetization approaches zero, where the spins are aligned along x in a paramagnetic manner by the light field. On the other hand, the mean photon number is zero for $g < g_c$, indicating the normal phase, and increases significantly for $g > g_c$, as expected by the superradiant phase, where the photon number $\langle n \rangle \propto N$ when the spin-photon coupling decays with $1/\sqrt{N}$. At $g = g_c$, the system undergoes a well-known second-order phase transition from ferromagnetic-normal (FM-NP) to paramagnetic-superradiant (PM-SP) phase. Notably, while the variational ansatz allows both the coherent and squeezed states of photons, the ground-state solutions in both phases correspond to coherent states with $\xi = 0$. Additionally, it is interesting to note that the observables (per number of spins) are independent of the number of spins.

By including the dressing transformation U_λ, we further investigate the full NGS-DMRG method with the general ansatz for the Dicke model. In Fig. 7.3(b) we show the average energy for multiple N. The NGS energies consistently lie below those of the GS case (solid line). However, as N increases, the difference between the two approaches diminishes. This trend is also observed in other measurable quantities. The smoothed transitions for both M_z and $\langle n \rangle / N$ stem from the finite-size effects (in number of spins) well represented by our hybrid method in the NGS case.

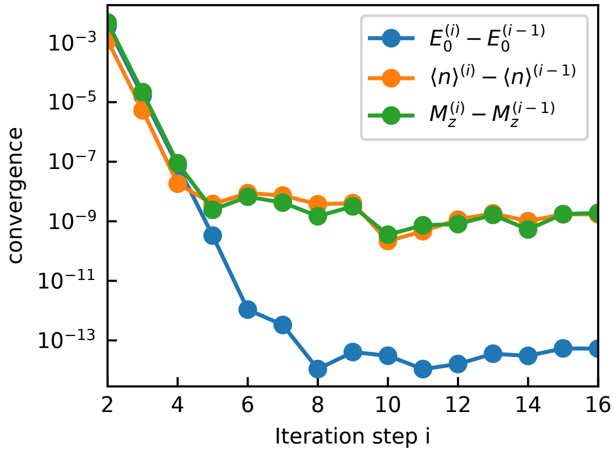

Figure 7.4: Convergence of the main observables in the Dicke model. We observe a quick convergence at $g = 0.25$ via $O[i+1] - O[i]$, stabilizing below 10^{-12} for energy and 10^{-8} for photon number and magnetization. The number of spins here is $N = 200$.

We find that the GS ansatz accurately describes the system in the thermodynamic limit, whereas the NGS ansatz effectively captures the finite-size behavior. This conclusion is supported by the observation that as N increases, the NGS curve approaches the GS one. Moreover, the ground state observables in the GS case remain N-independent, and our Gaussian results align with the well-established thermodynamic results of the Dicke superradiant quantum phase transition [75]. Therefore, a coherent state ansatz would appropriately represent the system's behavior in the limit of a large number of emitters.

As another layer of benchmarking, a pure DMRG approach for both spins and photons was taken for comparison. The DMRG results are very close to NGS-DMRG within the non-Gaussian ansatz for a fixed N. However, the necessary truncation $n_{\max}$ to achieve this match was large. For example, for $N = 100$, we observed convergent results (in $n_{\max}$) for a truncation $n_{\max} = 120$. Our method is both reliable and more efficient, since we do not need to play with photon Hilbert space truncation for distinct N.

Therefore, we have benchmarked the hybrid NGS-DMRG method for the simplest light-matter system, the Dicke model, accurately describing the well-established thermodynamic limit where the system is in a coherent separable state [75], and the finite-size behavior in the non-Gaussian ansatz is reproduced by full DMRG results.

7.2 Dicke-Ising model

Interactions between neighboring qubits are unavoidable in realistic quantum systems, irrespective of their realization. For instance, dipole-dipole interactions between molecules or Rydberg atoms lead to couplings that decay with distance as a power law; similar conclusions apply to circuit QED setups, where dipolar interactions are strongly modified by conducting plates forming the setup [29]. These interactions between spatially adjacent two-level quantum systems can be mapped to the nearest-neighbor exchange interactions between spins in the Dicke model. In this section, we consider the simplest form of these interactions by setting $J_x = J_y = 0$ and $J_z = 4J$, resulting in the Dicke-Ising model. A more general case of interactions will be discussed in Sec. 7.3.

In the pure Ising model, there are two two-fold degenerate phases separated by the critical interaction strength J_c. For $J > J_c$, the interaction tends to align the spins, resulting in ground states $|\downarrow\downarrow\downarrow \dots \downarrow\downarrow\rangle$ and $|\uparrow\uparrow\uparrow \dots \uparrow\uparrow\rangle$. For $J < J_c$, the spins prefer to anti-align, leading to $|\uparrow\downarrow\uparrow\downarrow \dots \uparrow\downarrow\rangle$ and $|\downarrow\uparrow\downarrow\uparrow \dots \downarrow\uparrow\rangle$. Thus, we refer to the $J > J_c$ as a *ferromagnetic* interaction and $J < J_c$ as an *antiferromagnetic* one. The term in Eq. 7.2 proportional to ε works as a classical longitudinal field. In a longitudinal field, the degeneracy of the ferromagnetic phase is lifted and $J_c = -\varepsilon/4$. In the classical transverse-field Ising model (TFIM), the phase transition at $J = J_c$ is destabilized by the external field, creating a paramagnetic phase between the two ordered phases. We found similar characteristics in its quantum counterpart, the Dicke-Ising model, but with unique superradiant-driven quantum effects.

Beyond the longitudinal magnetization M_z discussed in Sec. 7.1, which properly characterizes the uniform polarization of all spins, we further consider the staggered magnetization defined as $M_z^{(\mathrm{st})} = \sum_n (-1)^n \langle s_n^z \rangle / N$ to characterize the antiferromagnetic state with the presence of nearest spin interactions. Still, for a finite number of spins, both standard and staggered magnetizations can be misleading due to finite-size fluctuations. The spin correlations are a more convenient signature of the long-range order of the system. As we no longer expect perfect uniform polarization of all spins, we are also interested in the spatial distribution of spin configurations or correlations

$$C_{n,m}^{\alpha,\beta} = \langle s_n^\alpha s_m^\beta \rangle, \tag{7.14}$$

$$\bar{C}_{n,m}^{\alpha,\beta} = (-1)^{n-m} \langle s_n^\alpha s_m^\beta \rangle \,. \tag{7.15}$$

To avoid edge issues, we calculate the correlations in the bulk, i.e. for a fixed n far enough from the edges we focus on $m = n + r$ with $0 < r < N/2$. A ferromagnetic (antiferromagnetic) order will give $|C_{n,m}^{zz}| = 1/4$ ($|\bar{C}_{n,m}^{zz}| = 1/4$). The spin structure factor is an even more convenient observable, encapsulating all correlations between the spins. We define it as

$$S_{\alpha,\beta}(q) = \left(\frac{2}{N}\right)^2 \sum_{n,m} C_{n,m}^{\alpha,\beta} e^{iq(n-m)} \,. \tag{7.16}$$

The normalization is chosen such that the maximum value of $S_{\alpha\alpha}(q)$, which is reached at the nesting wavevector for a classical magnetic order, is one. A peak in $S_{zz}(q)$ at $q = 0$ ($q = \pi$) means that the spin configuration is ferromagnetic (antiferromagnetic). When the system is fully uncorrelated in a given direction α, we obtain $C_{n,m}^{\alpha\alpha} = 0$ for $n \neq m$ and $= 1$ for $n = m$.

This means that the spin structure factor $S_\alpha(q) = 1/N$. Therefore, we will be mainly focused on analyzing correlations and spin structure factors as a tool to define the spin ordering. For the photon degrees of freedom, we can distinguish the normal and superradiant phases by analyzing the mean photon number and its scaling with the number of spins.

7.2.1 Ferromagnetic coupling

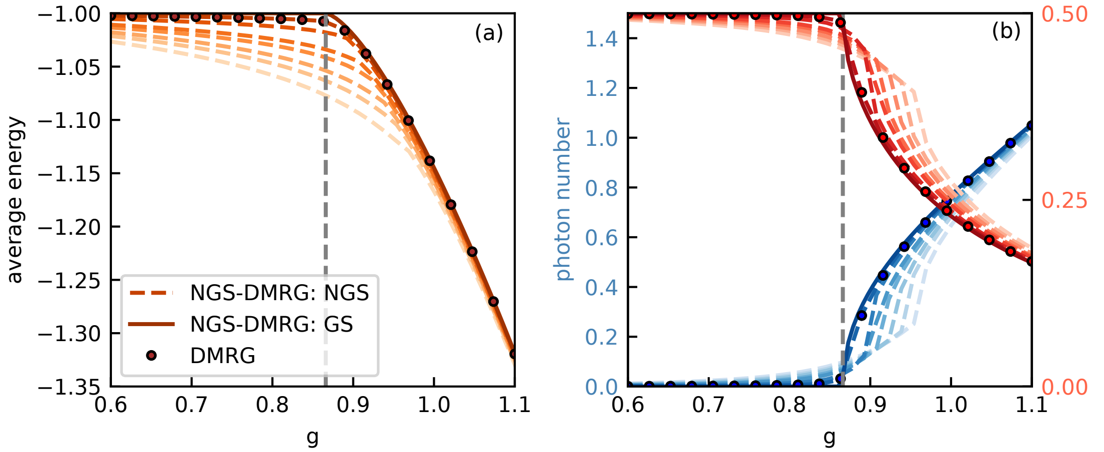

Figure 7.5: Observables of the ferromagnetic Dicke-Ising model ($J = 0.5 > J_c$). (a) The GS average energy (solid line) follows Eq. 7.18 until the second order phase transition at g_c where it starts decreasing; and the N-dependent NGS results are given by dashed lines. (b) The GS and NGS phonon number. The NGS curves (dashed) strongly deviate from the GS one (solid) around the critical point. The magnetization in z is enough to show the transition from FM to PM. Dashed lines $N = 4, 5, 6, 8, 10, 20, 50$ from light to dark colors, and dots are pure DMRG results for $N = 50$ and $n_{\max} = 80$.

We first consider the case of the ferromagnetic Ising interaction. Since the spins tend to align, the ground state of this Dicke-Ising model coincides with the FM-NP phase of the Dicke Hamiltonian. Within the GS case, using the spin ansatz as in Eq. 7.12, we can analytically obtain the modified critical coupling for the transition to the paramagnetic-superradiant phase as ($\varepsilon \neq 0$)

$$\tilde{g}_c(J) = g_c\sqrt{1 - \frac{J}{J_c}}, \tag{7.17}$$

where g_c is the critical coupling of the pure Dicke model ($J = 0$). Note that J_c is negative, so the critical coupling is increased by both J and ε. The normal phase ground state energy is merely shifted by the exchange interaction J as

$$E_0 = -\frac{\varepsilon}{2} - J. \tag{7.18}$$

This shows that the ferromagnetic Ising interaction further stabilizes the FM-NP phase showing the role of spin-spin and spin-photon competitions shifting the transition point to larger couplings (see Fig. 7.5). The spin state is not well represented by Eq. 7.12 outside the

FM-NP regime. Thus, the analysis is done with the full numerical method for both GS and NGS ansätze.

Now that we have obtained analytical intuition, we turn to the numerical results. In Fig. 7.5 we show the relevant observables of the system. They behave rather similarly to the $J = 0$ case. As we can see in the average energy [Fig. 7.5(a)], photon number, and magnetization [Fig. 7.5(b)], the critical coupling strength is shifted to a larger value due to the ferromagnetic Ising interaction. The modified critical spin-photon coupling and the normal phase average energy match the analytical prediction. When $g < g_c$ the system is in the normal phase, characterized by a vanishing photon number, while for an increasing g the system undergoes a second order phase transition to the superradiant phase where $\langle n \rangle > 0$, as shown in Fig.7.5(b). Since the zz (xx) correlations are maximized in the normal (superradiant) phase, this set of observables is enough to characterize this interaction regime. As in the Dicke model, we show the result from both GS (N-independent) and NGS in our numerical approach, and compare against DMRG. The non-Gaussian curves approach the Gaussian one for increasing N, showing the connection to the thermodynamic limit. The DMRG result for $N = 50$ and $n_{\max} = 80$ follows a similar behavior to the NGS case.

Interestingly, Kai et al. [120] predicted that in the thermodynamic limit the observables collapse to their analytical perturbative limiting results, given by $E_0 = -J$ for $g < g_c$ and $E_0 = -g^2/\omega$ for $g > g_c$ ($\varepsilon = 0$). This leads to the conclusion that the QPT here is of first order. However, these analytical energies are only valid away from the critical coupling $g_c(J)$, i.e. in the limits of large and small g. Moreover, the symmetry breaking nature of the system is not altered by the ferromagnetic Ising interaction, so we do not expect such a tremendous change with respect to the Dicke model. Indeed, our results show a second order phase transition from FM-NP to PM-SP phase, with the photon ground state corresponding to a coherent state.

7.2.2 Antiferromagnetic coupling

For $J < J_c$, the Ising interaction favors the anti-alignment of the spins, where now the staggered magnetization reaches $M_z^{(\mathrm{st})} = -1/2$ in the thermodynamic limit when g is sufficiently small. In addition, assuming periodic boundary conditions, the system can become geometrically frustrated for an odd number of spins. For instance, for the Gaussian ansatz, the minimized variational energies in the normal phase of the system are highly dependent of the number of particles for odd N, but do not change for even N. We focus the current analysis on the even N case.

The antiferromagnetic interaction creates a competition between the ferromagnetic configuration present in the Dicke normal phase and the antiferromagnetic configuration of the pure Ising model. Unlike the $J > J_c$ case, for $\lambda = 0$, here we observe that the ground state energy for small g equals J [see Fig. 7.6(a)], the mean photon number is zero, and the spin structure factor $S_{zz}(q = \pi)$ is maximized [cf. Fig. 7.6(c)]. This indicates that the antiferromagnetic configuration is the ground state in the normal phase. On the other hand, $S_{xx}(q) \approx 1/N$, as expected. Increasing g the system undergoes a quantum phase transition to a paramagnetic-superradiant phase where the quantum light field tends to align the spins along the x direction, so $S_{xx}(q = 0) \to 1$ and $S_{zz}(q) \to 1/N$ [see Fig. 7.6(d)]. The photon number in the PM-SP grows with g, as expected. In Figs. 7.6(a)-(b) we observe a discontinu-

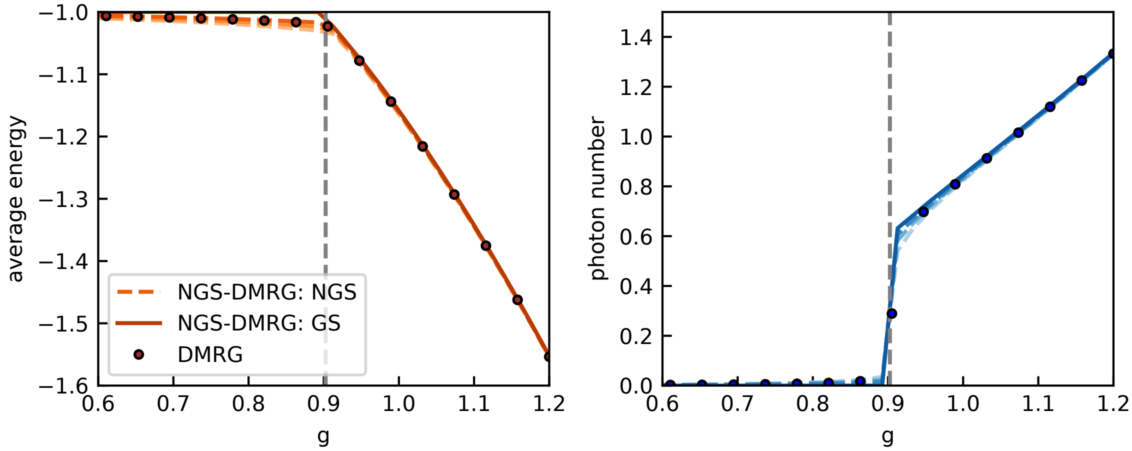

Figure 7.6: Observables of the antiferromagnetic Dicke-Ising model ($J = -1.0 < J_c$). We observe a distinct behavior where the QPT changes from second order ($J > J_c$) to a first order QPT. Order parameters show a discontinuity at the critical point and, therefore, a divergence in their first derivative. (a) Ground state energy starts from J in the AFM-NP until it reaches the critical value where it jumps and starts to decrease. (b) Photon number starts zero until it jumps to a certain value and then increases with g. Lines depict the hybrid method solutions in GS (solid) and NGS (dashed) ansatz, while dots correspond to DMRG with truncation at $n_{\max} = 50$. (c-d) The xx (dark red) and zz (red) spin structure factors for $g = 0.2$ (c) and $g = 1.4$ (d) in the NGS-DMRG. Here $N = 14$.

ity in the observables in the GS case. The discontinuity reveals the point where the system changes from one phase to another, indicating a possible first-order phase transition. The first-order phase transition in extended Dicke models has also been predicted in Ref. [20], appearing as a result of optical bi-stability. Note that first order QPT in multiqubit cavity QED systems has also been found in slightly different settings [84, 53, 52].

We note a related analysis of the AFM Dicke-Ising model performed by Zhang *et at.* [151] considering a separable mean field ansatz where the photons are in a coherent state while the spins are aligned in the xz plane with $|\phi_i\rangle = [\cos(\pi/4 - \phi_i/2), \sin(\pi/4 - \phi_i/2)]^T$. According to our more general ansatz, these assumptions turn out to be valid only in the limits of either small spin-photon coupling or zero spin exchange interaction, which makes sense due to the coherent nature of the Dicke model and the staggered alignment of the spins in the AFM Ising model in the thermodynamic limit. However, their limited treatment leads to a phase where both spin AFM order and photon superradiance coexist, while we were not able to observe such phenomenon. This shows that treating the spin part variationally can be tricky, demonstrating the need of a full treatment of the spin Hilbert space, as is the case in our method.

7.2.3 Phases summary

We have identified three distinct phases of the system: ferromagnetic-normal (FM-NP), antiferromagnetic-normal (AFM-NP), and paramagnetic-superradiant (PM-SP). We summarize these results in Fig. 7.7 by presenting the phase diagram in the J–g parameter space

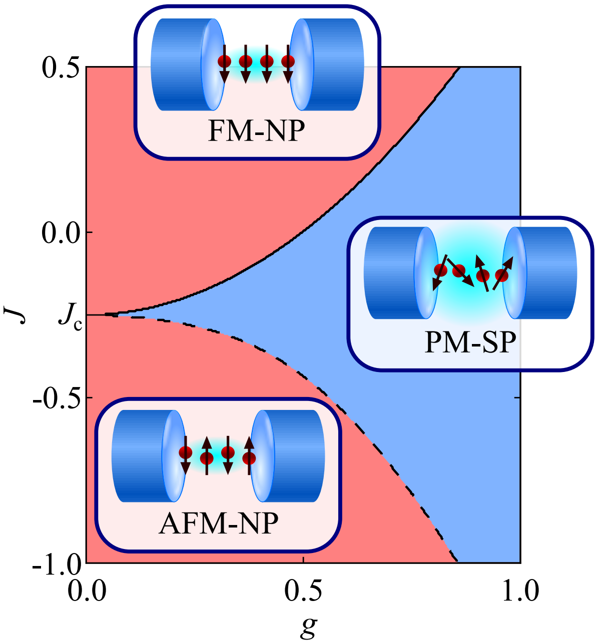

Figure 7.7: Phase diagram of the Dicke-Ising model. The three phases of the system are shown, where the lines separate the ordered-disordered(normal-superradiant) spin(photon) phases. Solid line depicts the second order quantum phase transition, while dashed line depicts the first order quantum phase transition. The FM-NP to PM-SP transition line matches the analytical result given by Eq. 7.17.

obtained by the our hybrid numerical method with $\lambda = 0$ (GS ansatz), for which the results are independent of the number of spins, corresponding to the thermodynamic limit. The phase boundaries where obtained by careful analysis of the photon and spin order parameters: the spin structure factors $S_{\alpha,\alpha}(q)$ and the mean photon number $\langle n \rangle / N$. Note that for $J > J_c$ we have a second order phase transition from FM-NP to PM-SP similarly to the Dicke model with the critical coupling g_c modified by J in a nonlinear fashion. In contrast, in the antiferromagnetic case $J < J_c$ there is a first order transition from AFM-NP to PM-SP. The longitudinal field ε influences the shape and position of the transition boundaries, the analytic form for the FM-NP to PM-SP transition is given by Eq. 7.17. Figs. 7.5 and 7.6 also show the case where the ground state can be a non-separable state of the NGS form for several values of N. In all cases the energy is below the GS one, showing that the NGS is a better solution in the context of the variational principle; the results converge to the GS one for increasing N.

To characterize the spin phases in this model, we focus on correlations in the z direction. In the normal phase, $S_{zz}(q)$ is maximal (minimal) at $q = 0$ and minimal (maximal) at $q = \pi$ due to perfect alignment (anti-alignment) of spins. Increasing the spin-photon coupling strength g, the system goes to the paramagnetic-superradiant regime. However, to properly characterize the photon phases it is necessary to study the scaling of the of the mean photon number with the number of emitters. As noticed by Hepp and Lieb [62], to obtain a meaningful thermodynamic limit in the Dicke model, the spin-photon coupling has to decay with the square root of the number of spins, as in our model, which leads to a

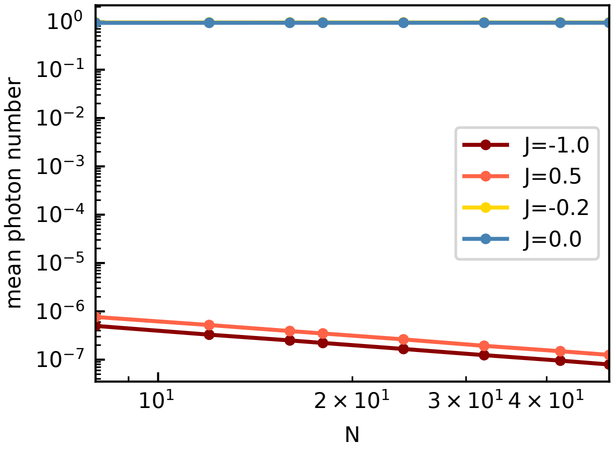

Figure 7.8: Mean photon number $\langle n\rangle/N$ scaling. For a small $g<\tilde{g}_c$ we observe $\langle n\rangle \propto c$ while for a large enough $g>\tilde{g}_c$ we observe a superradiant scaling $\langle n\rangle \propto N$.

change in the superradiant scaling to $\langle n\rangle \propto N$, while $\langle n\rangle$ should not grow with N in the normal phase. We show in Fig. 7.8, $\langle n\rangle/N$ vs N in the log-log scale. We observe that in both FM or AFM interacting regimes $\langle n\rangle/N$ decays polynomially with an exponent ≈ 1, $\langle n\rangle/N \approx 1/N$, meaning $\langle n\rangle$ does not grow with N. In the superradiant regime, we indeed observe a superradiant scaling where $\langle n\rangle \propto N$.

7.3 Dicke-XXZ model

Considering interactions between spins in all directions leads to the Dicke-XYZ model. When $J_x = J_y = J_z$, the spin exchange term becomes the well known XXX model, which is an exactly solvable model that respects SU(2) symmetry. However, anisotropies play a key role in spin-interacting systems. We keep $J_x = J_y$, but vary J_z as an anisotropy parameter. Without the light field, this corresponds to the celebrated XXZ model realizable via dipolar interactions of Rydberg atoms [124] which is integrable in 1D and can be studied via the coordinate Bethe ansatz [102]. It has three distinct quantum phases: the Ising-like ferromagnetic phase, the antiferromagnetic phase, and the XY phase lying in between them. With a vanishing longitudinal field case, $\varepsilon = 0$, the phases are separated by $|J_z| = 1$, where the phase transition at $J_z = -1$ is of infinite order, of the Berezinsky–Kosterlitz–Thouless (BKT) type. If $J_z = 0$, the system reduces to the free Fermion model. In general, however, the critical values depend on ε. For our chosen longitudinal field $\varepsilon = 1$ we expect the ferromagnet to occur at $J_z > 0$ and antiferromagnet at $J_z < J_c^{AFM} \approx -2.8$ [71]. However, the number of spins also affects the critical interaction strength for the XY to the antiferromagnetic phase transition, thus we can only reach the analytical J_c^{AFM} in the thermodynamic limit. In the J_z–ε phase diagram, the ferromagnetic and XY phases are delimited by the line $J_c^{FM} = 1 - \varepsilon$, while the antiferromagnetic and XY phase boundary is more involved [71]. From $J_z < J_c^{AFM}$ the ground state configuration is given by a combination of states with $N/2$ excited spins. The total magnetization $\langle s^z\rangle$ climbs unit by unit from zero to $-N/2$ as J_z grows, corresponding to the given number of excitations allowed. By adding spin-photon interactions, the effective long-range spin interaction mediated by photons has the potential to destabilize the QPTs seen in the pure XXZ model. In the next subsections, we show the most interesting features of the system for the three distinct interaction regimes.

7.3.1 Ferromagnetic phase

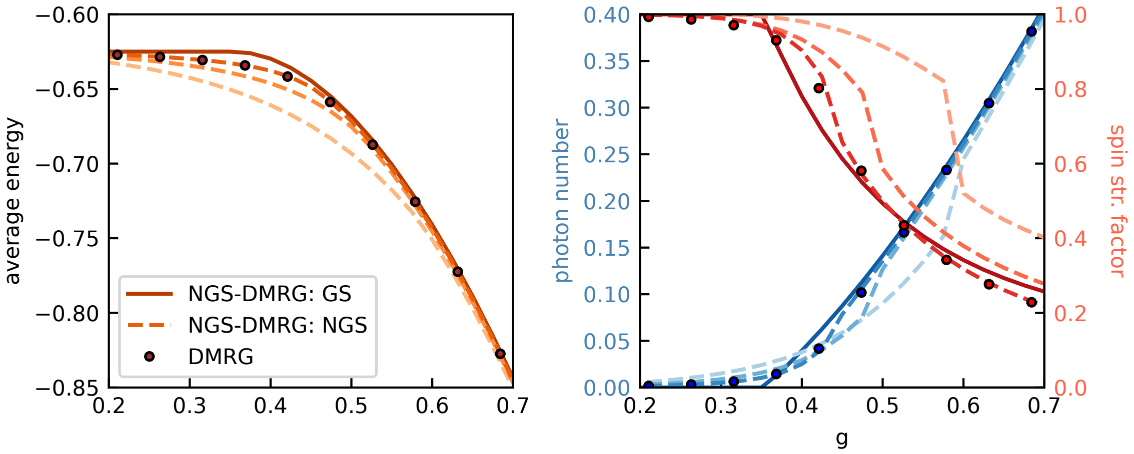

Figure 7.9: Dicke-XXZ model observables as a function of g in the ferromagnetic parameter region ($J_z = 0.5$). (top) The average energy, (bottom) photon number, and zz spin structure factor for fixed $q = 0$. In the GS case (solid lines), the observables as a function of g are in plateau until crossing the critical spin-photon coupling strength. NGS energy curves (dashed lines) lie below the Gaussian one. Parameters: $N = 4, 8, 16$ (NGS, dashed), and $N = 16$, $n_{\text{max}} = 40$ (DMRG, dots).

For $J_z > J_c^{FM}$, the effect of the spin-photon interaction on this phase looks similar to the ferromagnetic Dicke-Ising model. As shown in Fig. 7.9, the system undergoes a second order phase transition from ferromagnetic-normal to paramagnetic-superradiant for an increasing g. In the GS, the normal to superradiant QPT is observed as before. For instance, one can see the mean photon number being zero until it reaches a critical coupling and then increases with g. We also show in Fig. 7.9 the spin structure factor $S_{zz}(q = 0)$ as a function of g, attains maximum value in the normal phase, corresponding to the ferromagnetic configuration, and decreases reaching $1/N$, which we interpret as being fully uncorrelated in z. In the NGS case, the energy lies below the GS one, as it better captures the entanglement between the two subsystems for the finite chain. However, all observables converge in the limiting cases of large and small g.

7.3.2 Antiferromagnetic phase

In the parameter space regime where $J_z < J_c^{AFM}$ and g is small enough, the system is in the antiferromagnetic-normal phase. Let us restrict to the case of four spins, for which we can write the spin ground state as [103]

$$|\phi\rangle = \frac{1}{\mathcal{N}}[\beta(J_z)\,|AFM_2\rangle + |AFM\rangle], \tag{7.19}$$

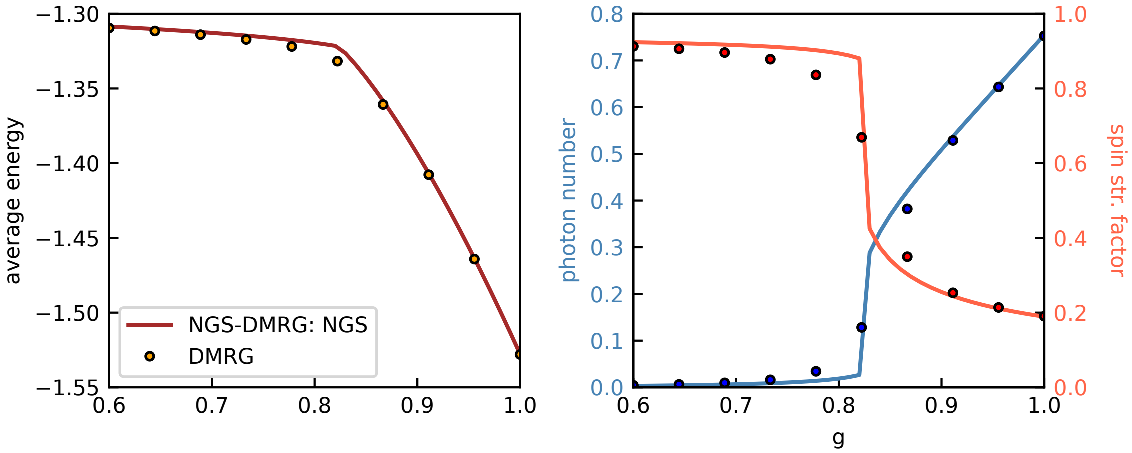

Figure 7.10: Main observables of the Dicke-XXZ model in the antiferromagnetic parameter region ($J_z = -5.0$). (a) average energy, (b) photon number, and spin structure factor in z for fixed $q = \pi$. Dashed lines depict NGS-DMRG results, while dots correspond to DMRG with truncation at $n_{\max} = 40$. (c-d) show the spin structure factors, in the NGS-DMRG, in xx (dark red) and zz (red), for $g = 0.6$ (c) and $g = 1.0$ (d), horizontal gray dashed line equals $1/N$. Here $N = 12$.

where $\mathcal{N}$ is a normalization factor, β is the weight, and

$$|AFM\rangle = \frac{1}{\sqrt{2}}(|0101\rangle + |1010\rangle), \tag{7.20a}$$

$$|AFM_2\rangle = \frac{1}{2}(|0011\rangle + |0110\rangle + |1001\rangle + |1100\rangle) \tag{7.20b}$$

are states with exactly two spin excitations. The factor $\beta(J_z)$ is inversely dependent of J_z, thus for a $J \to -\infty$, it is vanishing and we reach the Néel antiferromagnetic phase. This is also true for any N, where we have $|\phi\rangle \propto \left|AFM_{N/2}\right\rangle + |AFM\rangle$, with $\left|AFM_{N/2}\right\rangle$ a state vector containing all possible states with $N/2$ excited spins apart from the Néel state. As a result, strong finite-size effects arise in the Dicke-XXZ model, and are observed in all numerical methods utilized in this work. That way, since both GS and NGS are size-dependent, there is no advantage in the GS: the NGS ansatz is a better choice as the resulting smaller energy shows NGS to be a more accurate description. In the XY phase discussed next, the dependency with N is also strong. We thus restrict further calculations to the full method only.

As in the previous cases, the effective long-range spin-spin interaction given by the transverse photon field produces a paramagnetic phase of spins aligning to the field direction for a large enough spin-photon coupling strength. We show in Fig. 7.10 the aforementioned behavior, where in the normal phase the z spin structure factor is not maximum at $q = \pi$, unlike the Néel AFM in the Dicke-Ising, for a finite $J_z < J_c^{AFM}$ and N. The true Néel AFM phase is only achieved for $J_z \to -\infty$, and thus $S_{zz}(q = \pi)$ grows towards unit for an increasing $-J_z$. This supports our intuition given by the analytical solution of the pure XXZ model [Eq. 7.19], where we infer that the spin phase is qualitatively similar in the normal phase. DMRG solutions differ slightly only around the transition point, which is not well defined for a finite number of emitters.

DMRG treatment of the full Hamiltonian converged with a tolerance of 10^{-10} for a bond dimension m below 120, which is twice as large as the maximum bond dimension required when solving the effective spin Hamiltonian (in both GS and NGS), for $N = 12$ and $n_{\max} = 40$. In this parameter regime, even with a much smaller bond dimension, DMRG calculations of H_{eff} for $\lambda = 0$ (GS ansatz) displayed surprisingly slower convergence compared to both full NGS-DMRG method and DMRG of the full Hamiltonian.

7.3.3 XY phase

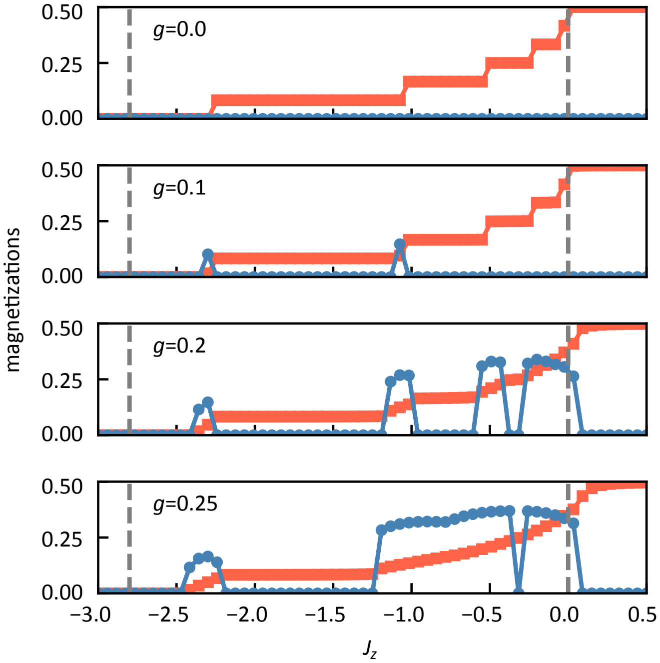

Figure 7.11: Absolute longitudinal (red, squares) and transverse (blue, circles) magnetizations as a function of J_z for multiple values of spin-photon coupling strength (from top to bottom) $g = 0, 0.1, 0.2, 0.25$. The spin-photon coupling strongly destabilizes the XY order, especially in the vicinity of the magnetization plateau transitions. Here we set $N = 12$.

In the XY phase of the XXZ model, with a longitudinal field ε, the spin correlations in z are suppressed while in-plane correlations dominate. As J_z goes from the FM to AFM regime, the number of spin excitations (with respect to the longitudinal field z) climbs from 0 (FM) to $N/2$ (AFM). As a result, we observe plateaus in the longitudinal magnetization for a finite N. Increasing the spin-photon coupling g, the effect of the transverse quantum field is manifested in the vicinity of the transition points between each plateau, unlike the classical transverse-field scenario. This destabilization resembles the Dicke-Ising model discussed above, where a paramagnetic phase appears between the FM/AFM-NP to PM-SP phase transition and broadens up for increasing g. Here, however, it happens not only at the critical quantum phase transition points, but also within the XY phase, as shown in Fig. 7.11. Intuitively, increasing the number of spins, the system becomes more susceptible to the spin-photon coupling: the more plateaus, the more transition points will be destabilized to a point where the XY phase is totally suppressed for any $g \neq 0$. However, it may also happen that an intermediate phase shows up. We indeed observe that when M_x peaks, $\langle n \rangle$ also does. Furthermore, the mean photon number remains of the same order in other regions, indicating a possible coexistence between XY spin order and superradiance.

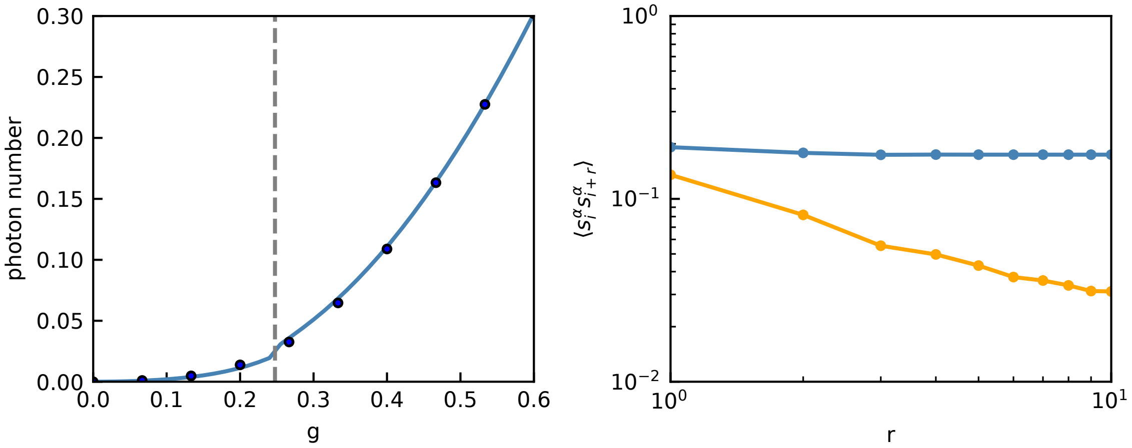

Figure 7.12: Photon number and spin correlations of the Dicke-XXZ model in the XY parameter region. (a) photon number as a function of g for $N = 12$. Both NGS-DMRG (solid line) and full DMRG (dots), with $n_{\max} = 40$, are shown, while the dashed line depicts the critical coupling strength. (b) spin-spin correlations in x; for small g, we observe a polynomial decay characteristic of the quasi-long-range order in the XY phase; for large g, the spins are polarized towards the same direction, generating a long-range order in the direction of the field. A larger N was chosen so that the decay laws are visible ($N = 24$ and $i = 5$). The anisotropy exchange was set to $J_z = -0.8$.

We show in Fig. 7.12 the mean photon number $\langle n \rangle / N$ and spin-spin correlations. The photon number is non-vanishing even for a small g. The result is also supported by DMRG for the full Hamiltonian. Dashed line depicts the critical spin-photon coupling, measured as the g value in which M_x abruptly jumps and starts increasing towards 1/2. Spin-spin correlations $C_{i,i+r}^{x,x}$ show a polynomial decay in r for a small g, due to the quasi-long-range order in the XY phase. While, after the critical coupling strength, we observe a true long-range order characterized by a saturation in the correlations. Indeed, below the critical coupling strength, we found a phase where spin order (XY) coexists with a finite $\langle n \rangle / N$.

As discussed above, the superradiant phase is characterized by the scaling of the mean photon number $\langle n \rangle \propto N$. We show in Fig. 7.13 its scaling in all parameter regimes. The superradiant scaling is observed for a large enough g for any J_z. For $J_z < J_c^{AFM}$, $J_z > J_c^{FM}$, and g small, the system is in the photon normal phase where $\langle n \rangle / N \propto 1/N$. This means that, even if $\langle n \rangle \neq 0$ for a given N, in the normal phase, it should not grow with N for an increasingly large N. We show the case where g is below its critical value for a given $J_c^{AFM} < J_z < J_c^{FM}$. Interestingly, the mean photon number grows with N, but not in a superradiant fashion. We observe a sublinear growth of the form $\langle n \rangle \propto N^{1-\alpha}$, with $0 < \alpha < 1$ instead. Incrementing g towards the critical strength, α continuously goes to zero, achieving the superradiant scaling. The spin-spin correlations in x also continuously move from a

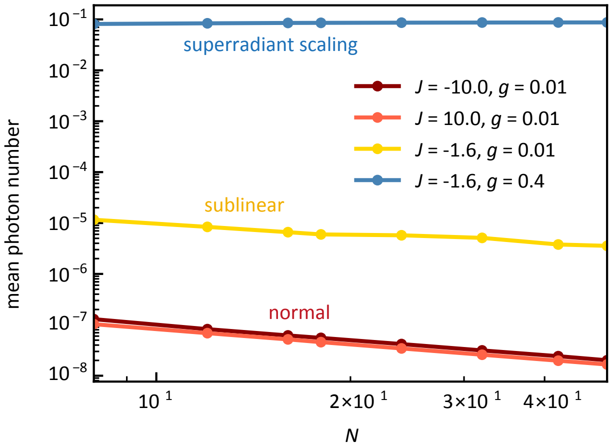

Figure 7.13: Scaling of $\langle n\rangle/N$ with $N \in [8, 50]$ in all regimes. The FM/AFM-normal phases exhibit a power-law decay with exponent ≈ 1 (dark and light red). The superradiant phase shows a nearly flat scaling, indicating $\langle n\rangle \propto N$ (blue). In the regime of moderate negative J_z, a sublinear scaling $\langle n\rangle \propto N^{1-\alpha}$ emerges (yellow).

polynomial decay to saturation, as shown in Fig. 7.14.

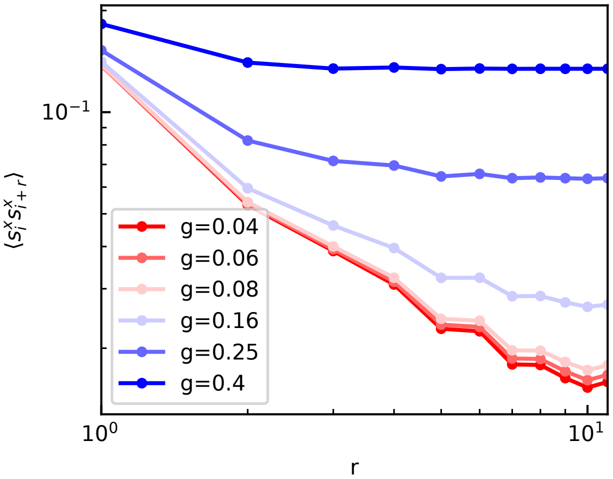

Figure 7.14: Spin-spin correlations in x continuously go towards saturation, starting from a polynomial decay in the XY phase regime. Parameters: $J_z = -1.6$ and $N = 24$.

8

Conclusions

In this thesis, we explored the field of strongly correlated hybrid quantum systems, with an emphasis on light-matter and electron-phonon systems. This study touches multiple research topics such as condensed matter physics, solid state physics, atomic, molecular, and optical (AMO) physics, materials science, and quantum optics. The interplay between competing interactions leads to a plethora of emergent phenomena, which we were deeply interested in.

We learned that a classical electromagnetic field trapped inside a microcavity can be decomposed into its Fourier modes, corresponding to a collection of simple harmonic oscillations. In second quantization formalism, the discrete energies of the quantum harmonic oscillators corresponds to a given number of photons. Quantum mechanically, we observed that even when the electromagnetic field is turned off, there are still vacuum fluctuations inside the cavity which is a pure quantum effect that has many physical consequences like the Casimir effect. When a particle is placed inside the cavity, its classical Hamiltonian is modified by the presence of a external field. Under the Coulomb gauge and the dipole approximation, we obtained the quantum Hamiltonian describing the interaction between photons and an ensemble of particles. This understanding lead us to the interest of the interplay between light-matter and matter-matter interactions. The so described light-matter interactions gives rise to emergent phenomena like superradiance, and the matter-matter interactions lead to intricate phases such as charge and spin density waves, (anti-)ferromagnetism, and Mott insulators. The question that have arisen is: how strong competing interactions affect the phases landscape? As a starting point, we focused on extending the Dicke model incorporating spin exchange interactions. This study culminated in two scientific papers: *The role of exchange interactions in the superradiance phenomena* (2024, submitted) and *A variational non-Gaussian approach to cavity QED with strongly interacting emitters* (In preparation). In summary, we systematically studied the impact of spin-spin interactions to the phases of the Dicke model in a one-dimensional chain. Using a hybrid many-body method which captures both the strong coupling and strong correlations, we found that the Ising-type interactions shift the superradiant phase boundary, exhibiting both first- and second-order transitions, and notably enhance the mean photon number in the PM-SP phase compared to the conventional Dicke model. When considering anisotropic interactions representing tunneling effects, our results revealed a complex interplay between anisotropy and photon coupling. A unique intermediate phase emerges from anisotropic interactions, where the XY

spin order and superradiant photon phase coexist. These results reveal that incorporating spin-spin interactions not only dramatically enhances the superradiant response, but also critically tunes the phase transitions, providing a framework for future experiments and applications in engineered light-matter quantum devices. In the development of the hybrid non-Gaussian numerical framework for spin-photon systems, we have benchmarked the results against known (mean-field) analytical solutions as well as brute-force DMRG treatment of the full Hamiltonian. In particular, we observe that the required bond dimension m of the effective Hamiltonian DMRG calculations was much smaller than when dealing with the full Hamiltonian, as expected. For small N, the bond dimension in the full DMRG calculations was more than twice as large compared to the NGS-DMRG method, and we expect that this difference would become even worse for increasing N. Indeed, the superradiant scaling of light makes the necessary Hilbert space truncation $n_{\max}$ increasingly large, making its size much larger than its effective spin counterpart. Surprisingly, even with a much smaller m, the convergence of the NGS-DMRG in the Gaussian ansatz is much slower than the other methods in some parameter regimes. However, the Gaussian states shown to be useful only when they represent the thermodynamic limit of the system. In such cases, the observables per spin are independent of number of emitters. Additionally, the effective spin Hamiltonian matrix for the Gaussian case is expected to be very sparse thus, the use of ED, instead of DMRG, for the Gaussian case is very beneficial and the hybrid method converges much faster. However, for more complex models involving anisotropic interactions the Gaussian ansatz produces inconclusive solutions. Non-Gaussian states, on the other hand, allow to obtain the ground state properties of the systems of interest with high precision and efficiency, agreeing well with DMRG. Our approach does not rely on specific system geometry or interaction range and can be easily applied to study more exotic models including e.g. long-ranged interactions, topological phenomena, and inhomogeneous couplings resulting from the light mode structure. Due to this flexibility, this study has branched into several other on-going projects, showing how beneficial it was for the research career of the author.

In the realm of electron-phonon systems, we considered a realistic material consisting of many ions and electrons. The ions, much heavier than the electrons, move at a much slower rate than the electrons, for which are seem as a background potential by the itinerant electrons. Under these assumptions, we learned how to second quantize the Hamiltonian to obtain, under a series of approximations, the paradigmatic Hubbard model, in which can be approximated, at half-filling, to the t-J and AFM Heisenberg models. However, the ionic motion cannot be completely disregarded in many realistic materials. Ions' motion, up to second order in the ion displacements, can be seem as a collection of harmonic oscillators. This collective motion is quantum mechanically represented by the bosonic quasi-particle called phonon. Moreover, we learned that in a polarizable medium the presence of an electron polarizes the atoms around it, which means that the electronic motion disturbs the system and creates phonons. We observed that this behavior is represented by the polaron quasiparticle, and its size depends on the characteristics of the electron-phonon interactions–which can be short or long ranged. We rigorously obtain the electron-phonon interaction Hamiltonian from second quantization of the electron-ion classical Coulomb interaction, up to first order in the ions' displacements, leading to the celebrated Holstein model that considers local electron-phonon interactions. When learning how to obtain the Holstein model, it became clear the possibility to explore extended versions of this model by taking a few steps back in the approximations. We also observed that some approximations taken into consideration to obtain the Hubbard model, connects to the ones in the Holstein model, showing that theses two models belong to similar energy scales and can be combined to study the interplay between strong electron-electron and electron-phonon interactions. However, due to the distinct nature of the bosonic and fermionic subsystems, both traditional approximate analytical and numerical methods fail to capture the emergent phenomena of this composite system. In order to circumvent this issue, we focused on two distinct approaches: hybrid quantum simulation and novel hybrid numerical techniques. The term "hybrid" here is coined from two different perspectives but both touches in the same idea of using two distinct approaches or systems to tackle the difficulties of strongly correlated *hybrid* quantum systems. These two ideas ended up in two distinct projects, in which one was published in the early PhD studies of the author: *Quantum simulation of extended electron-phonon-coupling models in a hybrid Rydberg atom setup* (Physical Review A 107 **3**, 032808) and *Applications of Novel Numerical Techniques to Extended Electron-Phonon Models* (on-going project). In the first, we have proposed a highly tunable experimental platform for simulation of compound quantum systems. It can be utilized for exploration of phase diagrams of extended Hubbard models in various geometric arrangements, possibly to study the onset of bipolaronic superconductivity. In the future, extensions to 2D and 3D structures and designing the system to exhibit flat bands and edge states seems particularly promising [126, 116, 123, 77, 32, 130], with exciting prospects for nonequlibrium dynamics and phonon driving related to recent breakthrough results on transient superconductivity [22, 7]. In the latter, the project goal is to return to the study of extended electron-phonon models, building on the quantum simulation frameworks introduced and the numerical techniques learned during the light-matter projects. We are applying these techniques to capture the intricacies of electron-phonon and electron-electron interactions with high precision. The project primarily represents a continuation of the original objectives, bringing forward the author's work in adapting and improving the numerical methods to handle complex, hybrid quantum systems.

In conclusion, this thesis encapsulates a comprehensive exploration of strongly correlated phases in hybrid, multicomponent systems, ranging from electron-phonon interactions to light-matter couplings. The research demonstrates the capability of advanced quantum simulation and numerical methods to uncover intricate behaviors in systems that defy classical simulation, ultimately contributing to the broader field of quantum technologies that mainly combines theoretical condensed matter physics, quantum optics, and AMO physics.

List of Figures

Bibliography

[1] Adams, C. S., Pritchard, J. D., and Shaffer, J. P. Rydberg atom quantum technologies. *Journal of Physics B: Atomic, Molecular and Optical Physics 53*, 1 (2019), 012002.

[2] Akahane, Y., Asano, T., Song, B.-S., and Noda, S. High-q photonic nanocavity in a two-dimensional photonic crystal. *nature 425*, 6961 (2003), 944–947.

[3] Alexandrov, A., and Ranninger, J. Bipolaronic superconductivity. *Physical Review B 24*, 3 (1981), 1164.

[4] Alexandrov, A. S., and Devreese, J. T. *Advances in polaron physics*, vol. 159. Springer, 2010.

[5] Altland, A. Advanced quantum mechanics, 2013.

[6] Altman, E., Brown, K. R., Carleo, G., Carr, L. D., Demler, E., Chin, C., DeMarco, B., Economou, S. E., Eriksson, M. A., Fu, K.-M. C., Greiner, M., Hazzard, K. R., Hulet, R. G., Kollár, A. J., Lev, B. L., Lukin, M. D., Ma, R., Mi, X., Misra, S., Monroe, C., Murch, K., Nazario, Z., Ni, K.-K., Potter, A. C., Roushan, P., Saffman, M., Schleier-Smith, M., Siddiqi, I., Simmonds, R., Singh, M., Spielman, I., Temme, K., Weiss, D. S., Vučković, J., Vuletić, V., Ye, J., and Zwierlein, M. Quantum simulators: Architectures and opportunities. *PRX Quantum 2* (Feb 2021), 017003.

[7] Babadi, M., Knap, M., Martin, I., Refael, G., and Demler, E. Theory of parametrically amplified electron-phonon superconductivity. *Phys. Rev. B 96* (Jul 2017), 014512.

[8] Bakemeier, L., Alvermann, A., and Fehske, H. Quantum phase transition in the dicke model with critical and noncritical entanglement. *Phys. Rev. A 85* (Apr 2012), 043821.

[9] Barredo, D., Lienhard, V., Scholl, P., de Léséleuc, S., Boulier, T., Browaeys, A., and Lahaye, T. Three-dimensional trapping of individual rydberg atoms in ponderomotive bottle beam traps. *Phys. Rev. Lett. 124* (Jan 2020), 023201.

[10] Baumann, K., Guerlin, C., Brennecke, F., and Esslinger, T. Dicke quantum phase transition with a superfluid gas in an optical cavity. *nature 464*, 7293 (2010), 1301–1306.

[11] Benedikter, N., Sok, J., and Solovej, J. P. The dirac-frenkel principle for reduced density matrices, and the bogoliubov-de-gennes equations. *arXiv preprint arXiv:1706.03082* (2017).

[12] Benedikter, N., Sok, J., and Solovej, J. P. The dirac–frenkel principle for reduced density matrices, and the bogoliubov–de gennes equations. In *Annales Henri Poincaré* (2018), vol. 19, Springer, pp. 1167–1214.

[13] Bernien, H., Schwartz, S., Keesling, A., Levine, H., Omran, A., Pichler, H., Choi, S., Zibrov, A. S., Endres, M., Greiner, M., Vuletić, V., and Lukin, M. D. Probing many-body dynamics on a 51-atom quantum simulator. *Nature 551*, 7682 (Nov 2017), 579–584.

[14] Bialynicki-Birula, I., and Rzążewski, K. No-go theorem concerning the superradiant phase transition in atomic systems. *Phys. Rev. A 19* (Jan 1979), 301–303.

[15] Bissbort, U., Cocks, D., Negretti, A., Idziaszek, Z., Calarco, T., Schmidt-Kaler, F., Hofstetter, W., and Gerritsma, R. Emulating solid-state physics with a hybrid system of ultracold ions and atoms. *Phys. Rev. Lett. 111* (2013), 080501.

[16] Bissbort, U., Hofstetter, W., and Poletti, D. Operator-based derivation of phonon modes and characterization of correlations for trapped ions at zero and finite temperature. *Phys. Rev. B 94* (Dec 2016), 214305.

[17] Bloch, I., Dalibard, J., and Nascimbene, S. Quantum simulations with ultracold quantum gases. *Nature Physics 8*, 4 (2012), 267–276.

[18] Bloch, J., Cavalleri, A., Galitski, V., Hafezi, M., and Rubio, A. Strongly correlated electron–photon systems. *Nature 606*, 7912 (2022), 41–48.

[19] Bloch, J., Cavalleri, A., Galitski, V., Hafezi, M., and Rubio, A. Strongly-correlated electron-photon systems. *arXiv preprint arXiv:2306.07313* (2023).

[20] Bowden, C. M., and Sung, C. C. First- and second-order phase transitions in the dicke model: Relation to optical bistability. *Phys. Rev. A 19* (Jun 1979), 2392–2401.

[21] Browaeys, A., and Lahaye, T. Many-body physics with individually controlled rydberg atoms. *Nature Physics 16*, 2 (2020), 132–142.

[22] Cavalleri, A. Photo-induced superconductivity. *Contemporary Physics 59*, 1 (2018), 31–46.

[23] Chin, C., Grimm, R., Julienne, P., and Tiesinga, E. Feshbach resonances in ultracold gases. *Rev. Mod. Phys. 82*, 2 (2010), 1225.

[24] Christianen, A., Cirac, J. I., and Schmidt, R. Bose polaron and the efimov effect: A gaussian-state approach. *Phys. Rev. A 105* (May 2022), 053302.

[25] Cirac, J. I., and Zoller, P. Goals and opportunities in quantum simulation. *Nature physics 8*, 4 (2012), 264–266.

[26] Clay, R. T., and Hardikar, R. P. Intermediate phase of the one dimensional half-filled hubbard-holstein model. *Phys. Rev. Lett. 95* (Aug 2005), 096401.

[27] Cong, I., Levine, H., Keesling, A., Bluvstein, D., Wang, S.-T., and Lukin, M. D. Hardware-efficient, fault-tolerant quantum computation with rydberg atoms. *Phys. Rev. X 12* (Jun 2022), 021049.

[28] Davis, E. J., Periwal, A., Cooper, E. S., Bentsen, G., Evered, S. J., Van Kirk, K., and Schleier-Smith, M. H. Protecting spin coherence in a tunable heisenberg model. *Phys. Rev. Lett. 125* (Aug 2020), 060402.

[29] De Bernardis, D., Jaako, T., and Rabl, P. Cavity quantum electrodynamics in the nonperturbative regime. *Phys. Rev. A 97* (Apr 2018), 043820.

[30] de Léséleuc, S., Lienhard, V., Scholl, P., Barredo, D., Weber, S., Lang, N., Büchler, H. P., Lahaye, T., and Browaeys, A. Observation of a symmetry-protected topological phase of interacting bosons with rydberg atoms. *Science 365*, 6455 (2019), 775–780.

[31] Denner, M. M., Miessen, A., Yan, H., Tavernelli, I., Neupert, T., Demler, E., and Wang, Y. A hybrid quantum-classical method for electron-phonon systems. *Communications Physics 6*, 1 (2023), 233.

[32] Di Liberto, M., Kruckenhauser, A., Zoller, P., and Baranov, M. A. Topological phonons in arrays of ultracold dipolar particles. *Quantum 6* (June 2022), 731.

[33] Dirac, P. A. Note on exchange phenomena in the thomas atom. In *Mathematical proceedings of the Cambridge philosophical society* (1930), vol. 26, Cambridge University Press, pp. 376–385.

[34] Disa, A. S., Fechner, M., Nova, T. F., Liu, B., Först, M., Prabhakaran, D., Radaelli, P. G., and Cavalleri, A. Polarizing an antiferromagnet by optical engineering of the crystal field. *Nature Physics 16*, 9 (2020), 937–941.

[35] Dou, F.-Q., Zhou, H., and Sun, J.-A. Cavity heisenberg-spin-chain quantum battery. *Phys. Rev. A 106* (Sep 2022), 032212.

[36] Dowling, J. P., and Milburn, G. J. Quantum technology: the second quantum revolution. *Philosophical Transactions of the Royal Society of London. Series A: Mathematical, Physical and Engineering Sciences 361*, 1809 (2003), 1655–1674.

[37] Eckle, H.-P. *Models of Quantum Matter: A First Course on Integrability and the Bethe Ansatz.* Oxford University Press, 2019.

[38] Emin, D. *Polarons.* Cambridge University Press, 2013.

[39] Evered, S. J., Bluvstein, D., Kalinowski, M., Ebadi, S., Manovitz, T., Zhou, H., Li, S. H., Geim, A. A., Wang, T. T., Maskara, N., et al. High-fidelity parallel entangling gates on a neutral-atom quantum computer. *Nature 622*, 7982 (2023), 268–272.

[40] Fehske, H., Hager, G., and Jeckelmann, E. Metallicity in the half-filled holstein-hubbard model. *Europhysics Letters 84*, 5 (2008), 57001.

[41] Fehske, H., Röder, H., Wellein, G., and Mistriotis, A. Hole-polaron formation in the two-dimensional holstein t-j model: A variational lanczos study. *Phys. Rev. B 51* (Jun 1995), 16582–16593.

[42] Ferraro, D., Campisi, M., Andolina, G. M., Pellegrini, V., and Polini, M. High-power collective charging of a solid-state quantum battery. *Phys. Rev. Lett. 120* (Mar 2018), 117702.

[43] Findik, G., Biliroglu, M., Seyitliyev, D., Mendes, J., Barrette, A., Ardekani, H., Lei, L., Dong, Q., So, F., and Gundogdu, K. High-temperature superfluorescence in methyl ammonium lead iodide. *Nature Photonics 15*, 9 (2021), 676–680.

[44] Franchini, C., Reticcioli, M., Setvin, M., and Diebold, U. Polarons in materials. *Nature Reviews Materials 6*, 7 (2021), 560–586.

[45] Fraxanet, J., Salamon, T., and Lewenstein, M. The coming decades of quantum simulation. *arXiv preprint arXiv:2204.08905* (2022).

[46] Frenkel, J. *Wave Mechanics: Elementary Theory.* No. v. 1 in International Series of Monographs on Physics; ed. by R.H. Fowler and P. Kapitza. Clarendon Press, 1932.

[47] Frenkel, J. Wave mechanics, clarendon, 1934.

[48] Fröhlich, H. Electrons in lattice fields. *Advances in Physics 3*, 11 (1954), 325–361.

[49] Fröhlich, H. On the theory of superconductivity: the one-dimensional case. *Proceedings of the Royal Society of London. Series A. Mathematical and Physical Sciences 223*, 1154 (1954), 296–305.

[50] Fröhlich, H., Pelzer, H., and Zienau, S. Xx. properties of slow electrons in polar materials. *The London, Edinburgh, and Dublin Philosophical Magazine and Journal of Science 41*, 314 (1950), 221–242.

[51] Gambetta, F. M., Li, W., Schmidt-Kaler, F., and Lesanovsky, I. Engineering nonbinary rydberg interactions via phonons in an optical lattice. *Phys. Rev. Lett. 124* (Jan 2020), 043402.

[52] Gammelmark, S., and Mølmer, K. Interacting spins in a cavity: Finite-size effects and symmetry-breaking dynamics. *Phys. Rev. A 85* (Apr 2012), 042114.

[53] Gammelmark, S., and Mølmer, K. Phase transitions and heisenberg limited metrology in an ising chain interacting with a single-mode cavity field. *New Journal of Physics 13*, 5 (may 2011), 053035.

[54] Ganczarek, W., Modugno, M., Pettini, G., and Zakrzewski, J. Wannier functions for one-dimensional $s-p$ optical superlattices. *Phys. Rev. A 90* (Sep 2014), 033621.

[55] Georgescu, I. M., Ashhab, S., and Nori, F. Quantum simulation. *Reviews of Modern Physics 86*, 1 (2014), 153.

[56] Giustino, F. Electron-phonon interactions from first principles. *Reviews of Modern Physics 89*, 1 (2017), 015003.

[57] Gould, T., and Bucko, T. C6 coefficients and dipole polarizabilities for all atoms and many ions in rows 1–6 of the periodic table. *J. Chem. Theory Comput. 12*, 8 (2016), 3603–3613.

[58] Guaita, T., Hackl, L., Shi, T., Hubig, C., Demler, E., and Cirac, J. I. Gaussian time-dependent variational principle for the bose-hubbard model. *Phys. Rev. B 100* (Sep 2019), 094529.

[59] Hague, J., and MacCormick, C. Quantum simulation of electron–phonon interactions in strongly deformable materials. *New Journal of Physics 14*, 3 (2012), 033019.

[60] Haroche, S. Nobel lecture: Controlling photons in a box and exploring the quantum to classical boundary. *Rev. Mod. Phys. 85* (Jul 2013), 1083–1102.

[61] Helmholtz, H. v. Über integrale der hydrodynamischen gleichungen, welche den wirbelbewegungen entsprechen. *Journal für die reine und angewandte Mathematik* (1858).

[62] Hepp, K., and Lieb, E. H. On the superradiant phase transition for molecules in a quantized radiation field: the dicke maser model. *Annals of Physics 76*, 2 (1973), 360–404.

[63] Hohenadler, M., and von der Linden, W. Lang-firsov approaches to polaron physics: From variational methods to unbiased quantum monte carlo simulations. In *Polarons in Advanced Materials*. Springer, 2007, pp. 463–502.

[64] Holstein, T. Studies of polaron motion: Part i. the molecular-crystal model. *Annals of physics 8*, 3 (1959), 325–342.

[65] Holstein, T. Studies of polaron motion: Part ii. the “small” polaron. *Annals of physics 8*, 3 (1959), 343–389.

[66] Hubbard, J. Electron correlations in narrow energy bands. *Proceedings of the Royal Society of London. Series A. Mathematical and Physical Sciences 276*, 1365 (1963), 238–257.

[67] Huber, J., Rey, A. M., and Rabl, P. Realistic simulations of spin squeezing and cooperative coupling effects in large ensembles of interacting two-level systems. *Phys. Rev. A 105* (Jan 2022), 013716.

[68] Jachymski, K., and Negretti, A. Quantum simulation of extended polaron models using compound atom-ion systems. *Phys. Rev. Research 2* (Aug 2020), 033326.

[69] Julià-Farré, S., Salamon, T., Riera, A., Bera, M. N., and Lewenstein, M. Bounds on the capacity and power of quantum batteries. *Physical Review Research 2*, 2 (2020), 023113.

[70] Julsgaard, B., Sherson, J., Cirac, J. I., Fiurášek, J., and Polzik, E. S. Experimental demonstration of quantum memory for light. *Nature 432*, 7016 (2004), 482–486.

[71] Justino, L., and de Oliveira, T. R. Bell inequalities and entanglement at quantum phase transitions in the *XXZ* model. *Phys. Rev. A 85* (May 2012), 052128.

[72] Karakuzu, S., Tocchio, L. F., Sorella, S., and Becca, F. Superconductivity, charge-density waves, antiferromagnetism, and phase separation in the hubbard-holstein model. *Phys. Rev. B 96* (Nov 2017), 205145.

[73] Kelly, S. P., Rey, A. M., and Marino, J. Effect of active photons on dynamical frustration in cavity qed. *Phys. Rev. Lett. 126* (Apr 2021), 133603.

[74] Kimble, H. J. The quantum internet. *Nature 453*, 7198 (Jun 2008), 1023–1030.

[75] Kirton, P., Roses, M. M., Keeling, J., and Dalla Torre, E. G. Introduction to the dicke model: From equilibrium to nonequilibrium, and vice versa. *Advanced Quantum Technologies 2*, 1-2 (2019), 1800043.

[76] Kline, M. *Mathematical thought from ancient to modern times*, vol. 1. Oxford university press, 1990.

[77] Knörzer, J., Shi, T., Demler, E., and Cirac, J. I. Spin-holstein models in trapped-ion systems. *Phys. Rev. Lett. 128* (Mar 2022), 120404.

[78] Kokail, C., Maier, C., van Bijnen, R., Brydges, T., Joshi, M. K., Jurcevic, P., Muschik, C. A., Silvi, P., Blatt, R., Roos, C. F., et al. Self-verifying variational quantum simulation of lattice models. *Nature 569*, 7756 (2019), 355–360.

[79] Kramer, P. A review of the time-dependent variational principle. In *Journal of Physics: Conference Series* (2008), vol. 99, IOP Publishing, p. 012009.

[80] Krishna, P. M., and Chatterjee, A. Existence of a metallic phase in a 1d holstein–hubbard model at half filling. *Physica C: Superconductivity 457*, 1-2 (2007), 55–59.

[81] Lang, I., and Firsov, Y. A. Kinetic theory of semiconductors with low mobility. *Sov. Phys. JETP 16*, 5 (1963), 1301.

[82] Lanzara, A., Bogdanov, P., Zhou, X., Kellar, S., Feng, D., Lu, E., Yoshida, T., Eisaki, H., Fujimori, A., Kishio, K., et al. Evidence for ubiquitous strong electron–phonon coupling in high-temperature superconductors. *Nature 412*, 6846 (2001), 510–514.

[83] Läuchli, A. M., Sudan, J., and Moessner, R. $s = \frac{1}{2}$ kagome heisenberg antiferromagnet revisited. *Phys. Rev. B 100* (Oct 2019), 155142.

[84] Lee, C. F., and Johnson, N. F. First-order superradiant phase transitions in a multiqubit cavity system. *Phys. Rev. Lett. 93* (Aug 2004), 083001.

[85] Li, X., Qiu, T., Zhang, J., Baldini, E., Lu, J., Rappe, A. M., and Nelson, K. A. Terahertz field–induced ferroelectricity in quantum paraelectric srtio3. *Science 364*, 6445 (2019), 1079–1082.

[86] Mahan, G. D. *Many-particle physics.* Springer Science & Business Media, 2013.

[87] Mandelstam, S. *Variational Principles in Dynamics and Quantum Theory.* Sir Isaac Pitman & Sons, 1960.

[88] Marquez Peraca, N., Li, X., Moya, J. M., Hayashida, K., Kim, D., Ma, X., Neubauer, K. J., Fallas Padilla, D., Huang, C.-L., Dai, P., et al. Quantum simulation of an extended dicke model with a magnetic solid. *Communications Materials 5*, 1 (2024), 42.

[89] Marzari, N., and Vanderbilt, D. Maximally localized generalized wannier functions for composite energy bands. *Phys. Rev. B 56* (Nov 1997), 12847–12865.

[90] Masson, S. J., Barrett, M. D., and Parkins, S. Cavity qed engineering of spin dynamics and squeezing in a spinor gas. *Phys. Rev. Lett. 119* (Nov 2017), 213601.

[91] Mattis, D. C. Ferromagnetism and spin waves in the band theory. *Phys. Rev. 132* (Dec 1963), 2521–2528.

[92] Mazzoncini, F., Cavina, V., Andolina, G. M., Erdman, P. A., and Giovannetti, V. Optimal control methods for quantum batteries. *arXiv preprint arXiv:2210.04028* (2022).

[93] McIver, J. W., Schulte, B., Stein, F.-U., Matsuyama, T., Jotzu, G., Meier, G., and Cavalleri, A. Light-induced anomalous hall effect in graphene. *Nature physics 16*, 1 (2020), 38–41.

[94] McLachlan, A. D. A variational solution of the time-dependent schrodinger equation. *Molecular Physics 8*, 1 (1964), 39–44.

[95] Mei, Y., Li, Y., Nguyen, H., Berman, P. R., and Kuzmich, A. Trapped alkali-metal rydberg qubit. *Phys. Rev. Lett. 128* (Mar 2022), 123601.

[96] Mendonça, J. P., and Jachymski, K. Quantum simulation of extended electron-phonon-coupling models in a hybrid rydberg atom setup. *Phys. Rev. A 107* (Mar 2023), 032808.

[97] Meth, M., Kuzmin, V., van Bijnen, R., Postler, L., Stricker, R., Blatt, R., Ringbauer, M., Monz, T., Silvi, P., and Schindler, P. Probing phases of quantum matter with an ion-trap tensor-network quantum eigensolver. *arXiv preprint arXiv:2203.13271* (2022).

[98] Mitrano, M., Cantaluppi, A., Nicoletti, D., Kaiser, S., Perucchi, A., Lupi, S., Di Pietro, P., Pontiroli, D., Riccò, M., Clark, S. R., et al. Possible light-induced superconductivity in k3c60 at high temperature. *Nature 530*, 7591 (2016), 461–464.

[99] Mueller, M., Said, R. S., Jelezko, F., Calarco, T., and Montangero, S. One decade of quantum optimal control in the chopped random basis. *Reports on Progress in Physics* (2022).

[100] Nataf, P., and Ciuti, C. No-go theorem for superradiant quantum phase transitions in cavity qed and counter-example in circuit qed. *Nature Communications 1*, 1 (Sep 2010), 72.

[101] Negretti, A., Gerritsma, R., Idziaszek, Z., Schmidt-Kaler, F., and Calarco, T. Generalized kronig-penney model for ultracold atomic quantum systems. *Phys. Rev. B 90* (Oct 2014), 155426.

[102] Nepomechie, R. I. Functional relations and bethe ansatz for the xxz chain. *Journal of statistical physics 111* (2003), 1363–1376.

[103] Niezgoda, A., Panfil, M., and Chwedeńczuk, J. Quantum correlations in spin chains. *Phys. Rev. A 102* (Oct 2020), 042206.

[104] Nomura, M., Anufriev, R., Zhang, Z., Maire, J., Guo, Y., Yanagisawa, R., and Volz, S. Review of thermal transport in phononic crystals. *Materials Today Physics 22* (2022), 100613.

[105] Nova, T., Disa, A., Fechner, M., and Cavalleri, A. Metastable ferroelectricity in optically strained srtio3. *Science 364*, 6445 (2019), 1075–1079.

[106] Ohgoe, T., and Imada, M. Competition among superconducting, antiferromagnetic, and charge orders with intervention by phase separation in the 2d holstein-hubbard model. *Phys. Rev. Lett. 119* (Nov 2017), 197001.

[107] Orso, G., Zakrzewski, J., and Deuar, P. Self-organized cavity bosons beyond the adiabatic elimination approximation. *arXiv preprint arXiv:2312.10502* (2023).

[108] Ortner, M., Micheli, A., Pupillo, G., and Zoller, P. Quantum simulations of extended hubbard models with dipolar crystals. *New Journal of Physics 11*, 5 (2009), 055045.

[109] Pekar, S. Local quantum states of electrons in an ideal ion crystal. *Zhurnal Eksperimentalnoi I Teoreticheskoi Fiziki 16*, 4 (1946), 341–348.

[110] Periwal, A., Cooper, E. S., Kunkel, P., Wienand, J. F., Davis, E. J., and Schleier-Smith, M. Programmable interactions and emergent geometry in an array of atom clouds. *Nature 600*, 7890 (2021), 630–635.

[111] Płodzień, M., Wasak, T., Witkowska, E., Lewenstein, M., and Chwedeńczuk, J. Generation of scalable many-body bell correlations in spin chains with short-range two-body interactions. *arXiv preprint arXiv:2306.06173* (2023).

[112] Primakoff, H., and Holstein, T. Many-body interactions in atomic and nuclear systems. *Physical Review 55*, 12 (1939), 1218.

[113] Pupillo, G., Griessner, A., Micheli, A., Ortner, M., Wang, D.-W., and Zoller, P. Cold atoms and molecules in self-assembled dipolar lattices. *Phys. Rev. Lett. 100* (2008), 050402.

[114] Quach, J. Q., McGhee, K. E., Ganzer, L., Rouse, D. M., Lovett, B. W., Gauger, E. M., Keeling, J., Cerullo, G., Lidzey, D. G., and Virgili, T. Superabsorption in an organic microcavity: Toward a quantum battery. *Science advances 8*, 2 (2022), eabk3160.

[115] Raab, A. On the dirac–frenkel/mclachlan variational principle. *Chemical physics letters 319*, 5-6 (2000), 674–678.

[116] Reshodko, I., Benseny, A., Romhányi, J., and Busch, T. Topological states in the kronig–penney model with arbitrary scattering potentials. *New Journal of Physics 21*, 1 (2019), 013010.

[117] Ribeiro, R. F., Martínez-Martínez, L. A., Du, M., Campos-Gonzalez-Angulo, J., and Yuen-Zhou, J. Polariton chemistry: controlling molecular dynamics with optical cavities. *Chemical science 9*, 30 (2018), 6325–6339.

[118] Ridley, B. Ii.1 - electron–phonon interactions in 2d systems. In *Hot Carriers in Semiconductor Nanostructures*, J. Shah, Ed. Academic Press, San Diego, 1992, pp. 17–51.

[119] Ritsch, H., Domokos, P., Brennecke, F., and Esslinger, T. Cold atoms in cavity-generated dynamical optical potentials. *Rev. Mod. Phys. 85* (Apr 2013), 553–601.

[120] Rohn, J., Hörmann, M., Genes, C., and Schmidt, K. P. Ising model in a light-induced quantized transverse field. *Phys. Rev. Res. 2* (May 2020), 023131.

[121] Rzażewski, K., Wódkiewicz, K., and Żakowicz, W. Phase transitions, two-level atoms, and the A^2 term. *Phys. Rev. Lett. 35* (Aug 1975), 432–434.

[122] Safavi-Naini, A., Lewis-Swan, R. J., Bohnet, J. G., Gärttner, M., Gilmore, K. A., Jordan, J. E., Cohn, J., Freericks, J. K., Rey, A. M., and Bollinger, J. J. Verification of a many-ion simulator of the dicke model through slow quenches across a phase transition. *Phys. Rev. Lett. 121* (Jul 2018), 040503.

[123] Salamon, T., Celi, A., Chhajlany, R. W., Frérot, I., Lewenstein, M., Tarruell, L., and Rakshit, D. Simulating twistronics without a twist. *Phys. Rev. Lett. 125* (Jul 2020), 030504.

[124] Scholl, P., Williams, H. J., Bornet, G., Wallner, F., Barredo, D., Henriet, L., Signoles, A., Hainaut, C., Franz, T., Geier, S., Tebben, A., Salzinger, A., Zürn, G., Lahaye, T., Weidemüller, M., and Browaeys, A. Microwave engineering of programmable xxz hamiltonians in arrays of rydberg atoms. *PRX Quantum 3* (Apr 2022), 020303.

[125] Schollwöck, U. The density-matrix renormalization group. *Rev. Mod. Phys. 77* (Apr 2005), 259–315.

[126] Shi, T., and Cirac, J. I. Topological phenomena in trapped-ion systems. *Phys. Rev. A 87* (Jan 2013), 013606.

[127] Shi, T., Demler, E., and Cirac, J. I. Variational study of fermionic and bosonic systems with non-gaussian states: Theory and applications. *Annals of Physics 390* (2018), 245–302.

[128] Shin, D., Hübener, H., De Giovannini, U., Jin, H., Rubio, A., and Park, N. Phonon-driven spin-floquet magneto-valleytronics in mos2. *Nature communications 9*, 1 (2018), 638.

[129] Shore, B. W., and Knight, P. L. The jaynes-cummings model. *Journal of Modern Optics 40*, 7 (1993), 1195–1238.

[130] Sompet, P., Hirthe, S., Bourgund, D., Chalopin, T., Bibo, J., Koepsell, J., Bojović, P., Verresen, R., Pollmann, F., Salomon, G., et al. Realizing the symmetry-protected haldane phase in fermi–hubbard ladders. *Nature* (2022), 1–5.

[131] Strack, P., and Sachdev, S. Dicke quantum spin glass of atoms and photons. *Phys. Rev. Lett. 107* (Dec 2011), 277202.

[132] Takada, Y., and Chatterjee, A. Possibility of a metallic phase in the charge-density-wave–spin-density-wave crossover region in the one-dimensional hubbard-holstein model at half filling. *Phys. Rev. B 67* (Feb 2003), 081102.

[133] Tam, K.-M., Tsai, S.-W., and Campbell, D. K. Dominant superconducting fluctuations in the one-dimensional extended holstein–extended hubbard model. *Phys. Rev. B 89* (Jan 2014), 014513.

[134] Vidal, J., and Dusuel, S. Finite-size scaling exponents in the dicke model. *Europhysics Letters 74*, 5 (2006), 817.

[135] Vukics, A., and Domokos, P. Adequacy of the dicke model in cavity qed: A counter-no-go statement. *Phys. Rev. A 86* (Nov 2012), 053807.

[136] Vukics, A., Griesser, T., and Domokos, P. Elimination of the a-square problem from cavity qed. *Phys. Rev. Lett. 112* (Feb 2014), 073601.

[137] Wang, Y., Chen, Z., Shi, T., Moritz, B., Shen, Z.-X., and Devereaux, T. P. Phonon-mediated long-range attractive interaction in one-dimensional cuprates. *Physical Review Letters 127*, 19 (2021), 197003.

[138] Wang, Y., Esterlis, I., Shi, T., Cirac, J. I., and Demler, E. Zero-temperature phases of the two-dimensional hubbard-holstein model: A non-gaussian exact diagonalization study. *Phys. Rev. Research 2* (Nov 2020), 043258.

[139] Wang, Y., Shi, T., and Chen, C.-C. Fluctuating nature of light-enhanced d-wave superconductivity: a time-dependent variational non-gaussian exact diagonalization study. *Physical Review X 11*, 4 (2021), 041028.

[140] Wang, Y., Steinberg, H., Jarillo-Herrero, P., and Gedik, N. Observation of floquet-bloch states on the surface of a topological insulator. *Science 342*, 6157 (2013), 453–457.

[141] Weber, S., Tresp, C., Menke, H., Urvoy, A., Firstenberg, O., Büchler, H. P., and Hofferberth, S. Calculation of rydberg interaction potentials. *Journal of Physics B: Atomic, Molecular and Optical Physics 50*, 13 (2017), 133001.

[142] Wellein, G., Röder, H., and Fehske, H. Polarons and bipolarons in strongly interacting electron-phonon systems. *Phys. Rev. B 53* (Apr 1996), 9666–9675.

[143] White, S. R. Density matrix formulation for quantum renormalization groups. *Phys. Rev. Lett. 69* (Nov 1992), 2863–2866.

[144] White, S. R. Density-matrix algorithms for quantum renormalization groups. *Phys. Rev. B 48* (Oct 1993), 10345–10356.

[145] Whitlock, S., Glaetzle, A. W., and Hannaford, P. Simulating quantum spin models using rydberg-excited atomic ensembles in magnetic microtrap arrays. *Journal of Physics B: Atomic, Molecular and Optical Physics 50*, 7 (2017), 074001.

[146] Wietek, A., and Läuchli, A. M. Sublattice coding algorithm and distributed memory parallelization for large-scale exact diagonalizations of quantum many-body systems. *Phys. Rev. E 98* (Sep 2018), 033309.

[147] Williamson, J. On the algebraic problem concerning the normal forms of linear dynamical systems. *American journal of mathematics 58*, 1 (1936), 141–163.

[148] Wilson, J. T., Saskin, S., Meng, Y., Ma, S., Dilip, R., Burgers, A. P., and Thompson, J. D. Trapping alkaline earth rydberg atoms optical tweezer arrays. *Phys. Rev. Lett. 128* (Jan 2022), 033201.

[149] Wineland, D. J. Nobel lecture: Superposition, entanglement, and raising schrödinger's cat. *Rev. Mod. Phys. 85* (Jul 2013), 1103–1114.

[150] Yin, T., Cocks, D., and Hofstetter, W. Polaronic effects in one- and two-band quantum systems. *Phys. Rev. A 92* (Dec 2015), 063635.

[151] Zhang, Y., Yu, L., Liang, J.-Q., Chen, G., Jia, S., and Nori, F. Quantum phases in circuit qed with a superconducting qubit array. *Scientific Reports 4*, 1 (Feb 2014), 4083.

[152] Zou, L. J., Marcos, D., Diehl, S., Putz, S., Schmiedmayer, J., Majer, J., and Rabl, P. Implementation of the dicke lattice model in hybrid quantum system arrays. *Phys. Rev. Lett. 113* (Jul 2014), 023603.